University of Naples Federico II
Polytechnic and Basic Sciences School

Department of Chemical Sciences

Ph.D. in Chemical Sciences

Artificial metalloenzymes active in oxidation chemistry

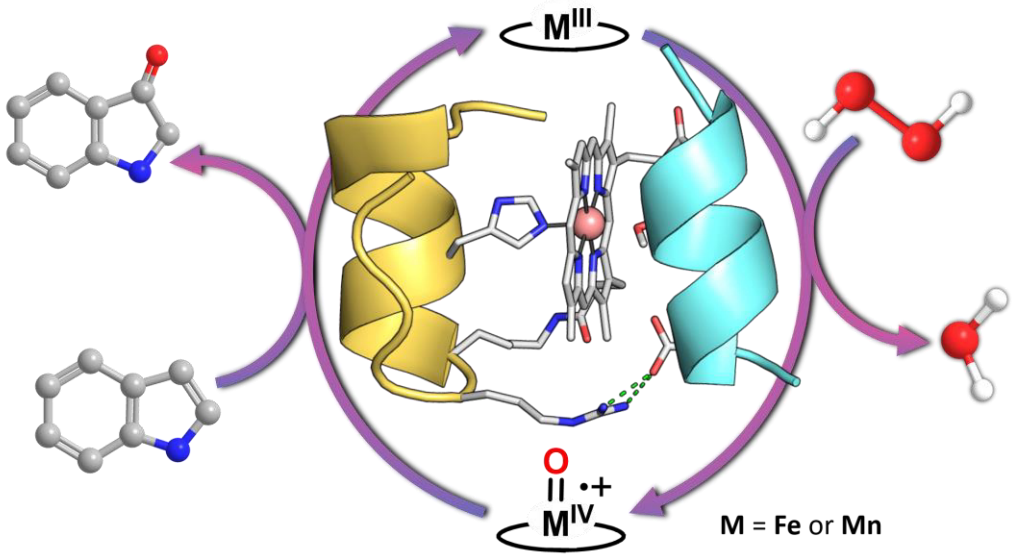

Linda Leone

Advisor:
prof. Angela Lombardi

Examiner:
prof. Alessandra Napolitano

XXXII Cycle 2017 – 2020
Coordinator: prof. Angela Lombardi

UNIVERSITY OF NAPLES FEDERICO II

Polytechnic and Basic Sciences School

Ph.D. School in Chemical Sciences

ARTIFICIAL METALLOENZYMES ACTIVE IN OXIDATION CHEMISTRY

Linda Leone

Advisor:

prof. Angela Lombardi

Examiner:

prof. Alessandra Napolitano

XXXII Cycle 2017/2020

Coordinator: prof. Angela Lombardi

This page was intentionally left blank.

"There is nothing more wonderful than being a scientist.
Nowhere I would rather be than in my lab,
staining up my clothes and getting paid to play."

Marie Curie

This page was intentionally left blank.

TABLE OF CONTENTS

This page was intentionally left blank.

SUMMARY

Bioinorganic chemists tackled the challenge to unravel the mechanisms that allow the protein matrix to modulate the catalytic activity of metal-containing cofactors through the development of artificial systems. In this perspective, heme-proteins represent a significant source of inspiration: researchers have attempted for decades to develop efficient and selective metalloporphyrin-based catalysts. Significant advance has been achieved in the design and engineering of protein scaffolds to host metalloporphyrins and to modulate their reactivity. Peptide-based architectures of different sizes have been exploited for the construction of catalytic systems. Among them, synthetic porphyrin-peptide conjugates known as "Mimochromes" represent an important class of artificial heme enzymes. Their structure consists of two α-helical peptides covalently linked to a metalloporphyrin core, resulting into a helix-heme-helix sandwich. Their simple scaffold has been optimized to reproduce the functional properties of peroxidases. Mimochrome VI*a (MC6*a), in its Fe^{III} complex, recently emerged as the best artificial peroxidase known so far, overcoming the catalytic efficiency of horseradish peroxidase (HRP) in ABTS oxidation. Moreover, the cobalt derivative (Co-MC6*a) behaves as a very promising catalyst in hydrogen evolution reactions. These recent achievements prompted us to further evaluate the versatility of the MC6*a scaffold towards metal replacement, by swapping iron to manganese.

The primary aim of this PhD project was to expand the scope of transformations accessible by MC6*a complexes in oxidation chemistry. Taking into account the catalytic promiscuity of iron and manganese porphyrins towards diverse oxidative transformations, the analysis of the spectroscopic, redox and catalytic properties of Fe- and Mn-MC6*a has been performed.

Compared to other peptide-porphyrin conjugates with a fully solvent-exposed distal site, both Fe- and Mn-MC6*a display an increased ability to promote the deprotonation of metal-bound water and hydrogen peroxide. This property allows MC6*a complexes to reach their highest activity towards H_2O_2 at lower pH values, approaching those of the natural counterparts.

Both Fe- and Mn-MC6*a demonstrated to be efficient and robust catalysts in the H_2O_2-mediated sulfoxidation of thioethers, being among the most active artificial heme enzymes studied for this reaction. The two catalysts displayed divergent behaviours towards the oxidation of indole. Notably, Mn-MC6*a displays higher chemo-selectivity compared to Fe-MC6*a, but also surpasses most of heme-enzymes examined to the same end. Mn-MC6*a represents one of the most proficient catalysts for indole oxidation, mainly due to the possibility of controlling the formation of different oxidation products with high selectivity. Among them, the formation and isolation of the highly reactive 3-oxindolenine is very important, because it could represent a useful synthon in organic synthesis.

Overall, the results of this PhD thesis pave the way for the application of mimochromes to synthetic chemistry. These catalysts fill the middle ground between small-molecule and biological catalysts, since they own a minimal structure that enables substrate promiscuity and a designed peptide scaffold that modulates the reactivity of the metal ion.

SECTION 1:
Introduction

This page was intentionally left blank.

1. HEME ENZYMES IN OXIDATION CHEMISTRY

Nature has evolved enzymes to catalyse a wide range of complex oxidative transformations using bioavailable O_2 as the oxidant.[1] The use of the dioxygen molecule as the electron acceptor in a redox process is far from simple, due to the high chemical stability of the O–O bond.[2] Most O_2-dependent enzymes employ redox-active transition metal ions as cofactors, which can push their electron density into a bound dioxygen molecule, overcoming the kinetic barrier of O–O bond cleavage.[3–5]

Heme-enzymes can be viewed as the paradigm of the mechanisms adopted by Nature to control the reactivity of a metal ion.[6] The heme cofactor employs a porphyrin framework acting as a redox non-innocent ligand to an iron ion. The highly conjugated structure of the porphyrin macrocycle allows for spin delocalization and serves as an electron density reservoir in the stabilization of high-valent metal states.[7] The most studied heme-enzymes are peroxidases,[8] cytochrome P450 oxygenases (P450s)[9] and heme dioxygenases.[10] The last two classes of enzymes use O_2-dependent pathways, whereas peroxidases employ H_2O_2 (Scheme 1.1). Once dioxygen is reduced to the peroxide form, the catalytic mechanisms of both O_2- and H_2O_2-dependent enzymes involve the O–O bond cleavage, leading to common reaction intermediates.[11–13] The first intermediate is called Compound I and consists of a ferryl heme with a porphyrin or protein radical. One-electron reduction of Compound I generates Compound II, which is still a ferryl heme but has no organic radical. Their subsequent reactivity depends on a complex interplay between the cofactor and the surrounding protein matrix, which enables a wide array of enzymes to promote a variety of different oxidations using the same intermediates.[14–17] Heme dioxygenases have the peculiarity to not utilize Compound I as the active oxidizing species,[13] which differentiates them from all the other O–O bond activating heme enzymes.

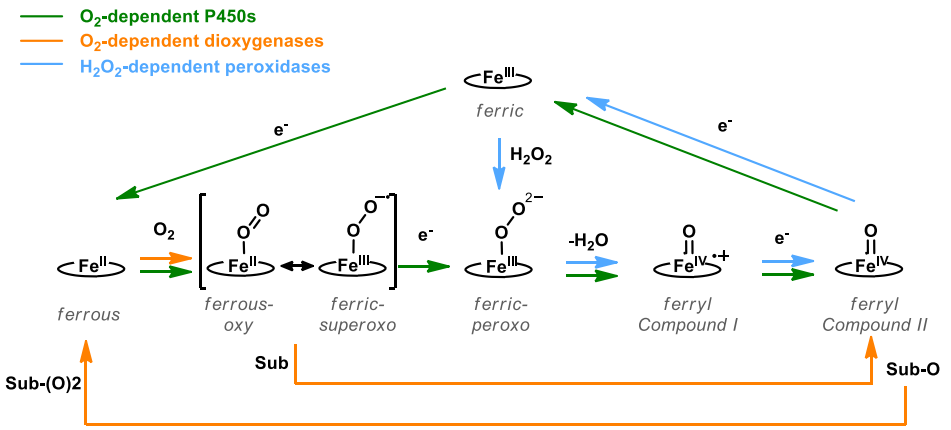

Scheme 1.1. Reaction scheme for heme-catalysed oxygen activation. The heme macrocycle is represented as a black circle. Protons and the protein-derived iron axial ligand are not shown for sake of simplicity. *Sub*, *Sub-O* and *Sub-(O)2* denote the substrate, the mono-oxygenated and the doubly-oxygenated product, respectively.

Heme ferryl-oxo intermediates act as powerful and versatile biological engines in oxidation chemistry. Understanding their nature and reactivity has been matter of extensive studies and is the key for the design of new tailor-made catalysts.[18]

1.1. Cytochrome P450 oxygenases

P450s are among the most versatile enzymes in terms of the variety of substrates and transformations that are able to promote.[19,20] Their biological functions range from the catabolism of xenobiotics to the biosynthesis of steroid hormones and typically involve the highly specific oxygenation of organic molecules.[21] All P450s share a five-coordinate heme iron with the thiolate group of a cysteine acting as the axial ligand.[9]

The catalytic mechanism of P450s is a complex cascade of individual steps (Scheme 1.2) also involving the interaction with redox partners that provide reducing equivalents in the form of NAD(P)H.[11,20]

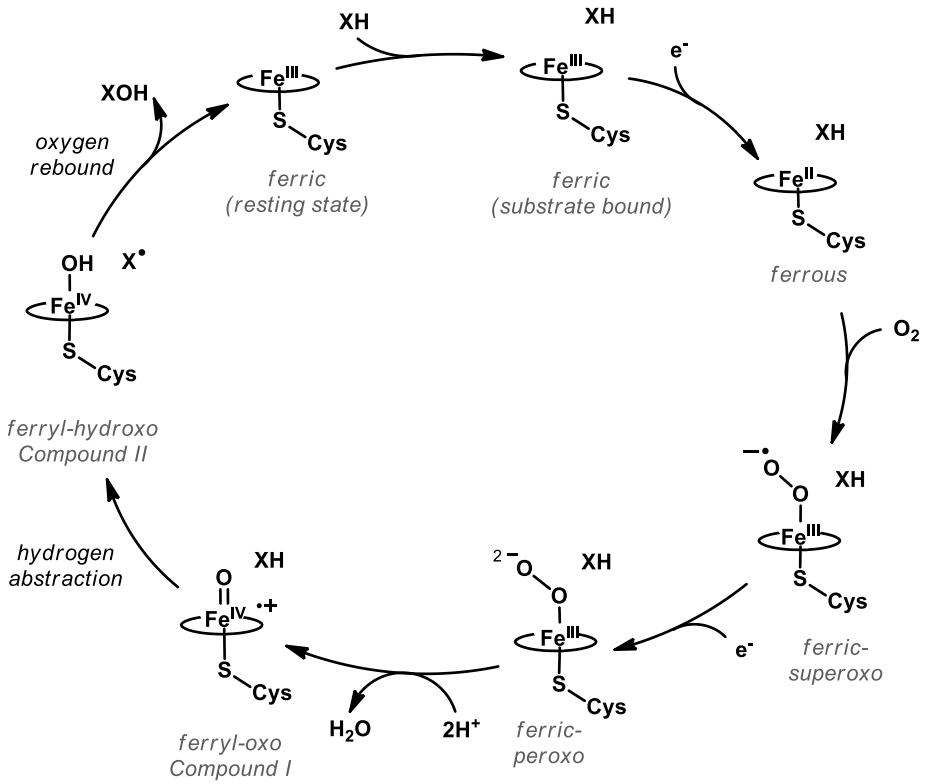

Scheme 1.2 General reaction mechanism for P450-catalysed substrate hydroxylations. XH and XOH represent a substrate and a hydroxylated product, respectively.

In the resting state, P450s appear in the ferric form because of a relatively low reduction potential of the Fe^{III}/Fe^{II} couple, typically in the range between - 400 and

- 170 mV.[22] Substrate recognition triggers the catalytic cycle by inducing a shift in the reduction potential up to 100 mV more positive. This represents a specific regulatory mechanism, since the reduction of ferric-heme and the reaction with dioxygen can occur only in the presence of a substrate. Upon the delivery of the first electron from a reductase, dioxygen binds to the ferrous heme, forming a species that is best described as a ferric-superoxo complex. Further reduction of this species leads to a ferric-peroxo intermediate. Double protonation at the distal

oxygen induces the O–O bond cleavage, yielding Compound I. The mechanism of proton delivery to has been subject of an extensive debate in the literature. Important clues have come from the comparison of the crystal structures of ferric and oxy-ferrous P450cam.[23,24] It was observed that the hydrogen bond between Thr252 side chain and Gly248 is disrupted upon O_2 binding. This induces the widening of the active site, which allows for water molecules to enter. Further, mutagenesis studies identified Asp251 as a key residue in O_2 activation. Inspection of the structure of ferrous P450cam in complex with its redox partner putidaredoxin showed the disruption of the ionic pairs that involve Asp251 in the ferric form (Figure 1.1). The conformational change allows this residue to act as a proton carrier.[25]

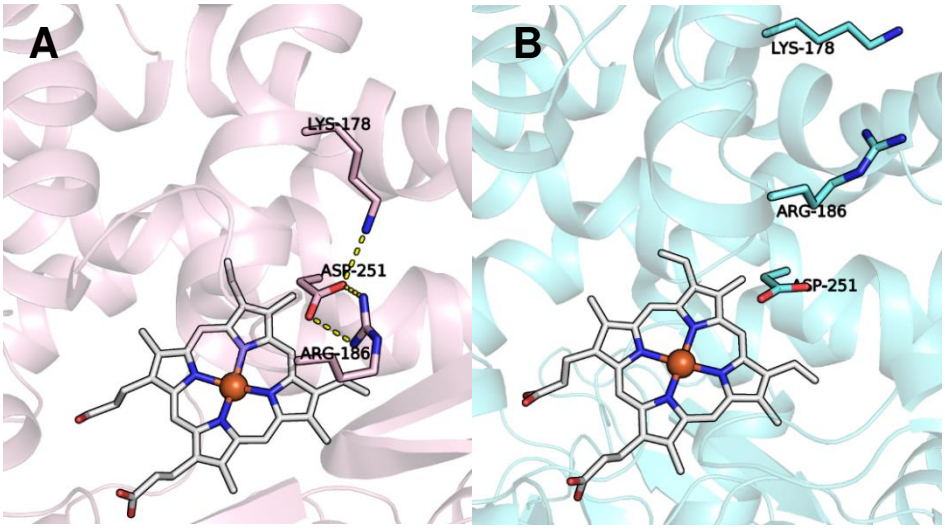

Figure 1.1. Comparison between the X-ray structures of (A) ferric P450cam (PDB ID: 2CPP) and (B) ferrous P450cam in complex with putidaredoxin (PDB ID: 4JWU), with a focus on the ionic interactions involving Asp251.

Compound I is responsible for the majority of P450 oxidative reactions. Recent studies have provided the spectroscopic capture and characterization of this transient intermediate.[26]

The mechanism of P450-catalysed hydroxylation has become known as "oxygen rebound mechanism" since it was postulated by Groves in 1970s.[27,28] It consists of a stepwise process involving H· radical abstraction from the substrate, forming a ferryl-hydroxo complex (Compound II) that rapidly recombines with the substrate radical to yield the hydroxylated product. Kinetic isotope effects and experiments with radical clock substrates provided support to this mechanism for hydrocarbon hydroxylation.[29,30]

P450s Compound I possess the unique ability among heme enzymes to oxygenate unactivated C-H bonds with remarkable rate constants (up to 1×10^7 M^{-1} s^{-1} for the hydroxylation of unsaturated fatty acids).[26]

It has been demonstrated that the axial cysteine assumes a fundamental role in C-H bond activation by P450s.[31,32] The electron-donating thiolate ligand acts as an electron pump to the metal-oxo species, increasing the pK_a of compound II. A more basic Compound II translates into a stronger $Fe^{IV}O$–H bond, which in turn determines a favourable free energy balance between the C–H bond breaking and the O–H bond making events. Most of histidine-ligated heme-proteins appear to have non-basic ferryl-oxo species, consistent with their ineffective reactivity towards H· abstraction. However, recent spectroscopic and structural studies provided evidences for protonated ferryl-oxo (Compound II) species in histidine[33] and tyrosine[34] ligated heme-proteins. These studies highlight that a complete description of the structural determinants for the exceptional reactivity of P450s is still to be found.

1.2. Peroxidases

Peroxidases are ubiquitous oxidative enzymes. They are found in most organisms, including bacteria, fungi, plants and mammals.[35] The nature of their reducing substrates depends on the precise physiological role of the peroxidase, ranging from Mn^{2+} ions for manganese peroxidase to cytochrome *c* for cytochrome *c*

peroxidase (C*c*P). Plant enzymes such as horseradish peroxidase (HRP) usually oxidize aromatic amines or phenols and are typically able to accept a variety of reducing substrates.[36,37] Despite their low sequence homology, the structure of the catalytic site is highly conserved among peroxidases from different organisms.[8] It consists of a five-coordinate heme with an axially ligated proximal histidine, which forms a hydrogen bond with the carboxylate group of a highly conserved aspartate residue through the non-coordinated N^{δ} (Figure 1.2). This interaction imparts a higher imidazolate character to the histidine, which is responsible for the lower reduction potential of peroxidases[38,39] compared to globins,[40,41] whose N^{δ} forms a weaker hydrogen bond with the backbone oxygen of a leucine residue.

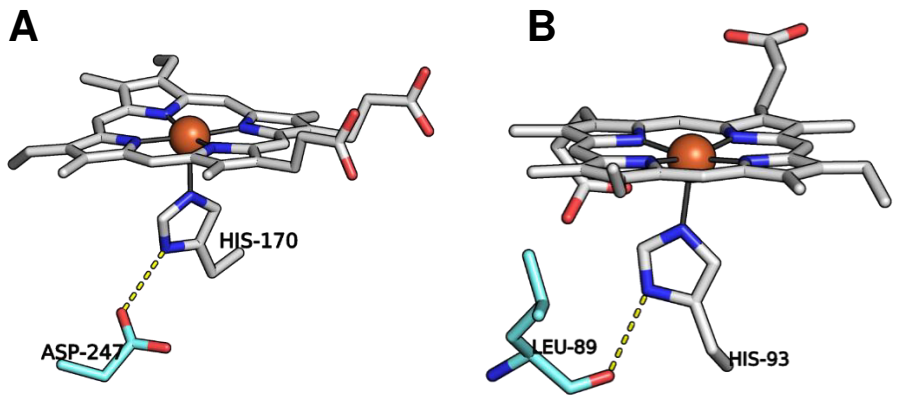

Figure 1.2. Comparison between the heme proximal sites of (A) HRP (PDB ID: 1ATJ) and (B) Myoglobin (PDB ID: 1MBN).

Catalytic cycle of peroxidases starts with the reaction of the resting, ferric state of the enzyme with hydrogen peroxide that leads to Compound I formation (Scheme 1.3).[42]

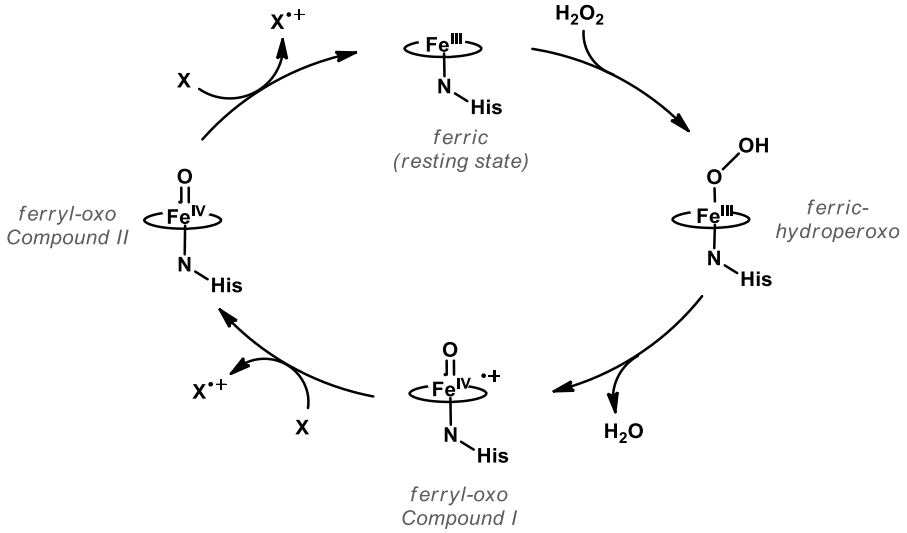

Scheme 1.3. General catalytic mechanism of peroxidase catalysed substrate oxidation. X and $X^{\cdot+}$ represent the substrate and its one-electron oxidation product.

Mutagenesis studies, mostly with C*c*P, evidenced that a histidine and an arginine residue in the distal site play fundamental roles in Compound I formation.[43,44] It was initially proposed that the distal His directly mediates the proton transfer between the proximal (O1) and the distal (O2) oxygen atoms of peroxide, acting as an acid-base catalyst (Scheme 1.4A).[45] The distal Arg was thought to stabilize the increasing negative charge on the leaving O2 atom, thus favouring the heterolytic O–O bond cleavage. One problem with the original mechanism is that the distal His is too far from the O1 atom to make a strong hydrogen bond. It was then proposed that the distal His is assisted by a water molecule in acid-base catalysis (Scheme 1.4B).

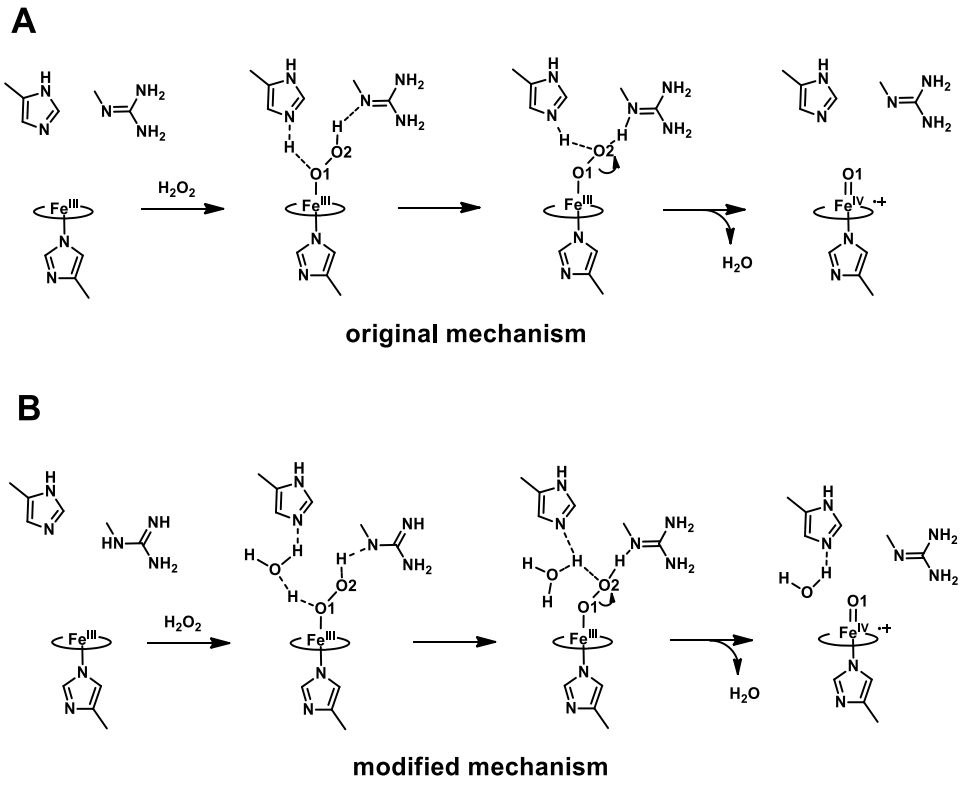

Scheme 1.4. Mechanism of peroxidase Compound I formation. In the original mechanism (A) the distal His shuttles the proton from the O1 to the O2 of peroxide, while in the modified mechanism (B), the distal His is assisted by a water molecule in acid-base catalysis.

Peroxidases Compound I are characterised by an increased stability compared to those of P450s, allowing for their isolation and structural characterization. Crystal structures of Compound I of HRP[46] and C*c*P[47] provided fundamental insights on the mechanism of O–O bond cleavage. Indeed, in both the structures of HRP and C*c*P Compound I, there is a well-ordered water molecule close to the ferryl oxygen, correctly positioned to serve this function (Figure 1.3). Mutation of the distal Arg resulted in a decreased rate of Compound I formation, in agreement with the proposed original mechanism. However, distal Arg mutants also displayed altered stability and reactivity of Compound I, suggesting the

involvement of this residue in a direct interaction with the O1 rather than with the O2. This was confirmed by the crystal structures, where the distal Arg acts as a hydrogen bond donor to the ferryl oxygen (O1), which accounts for the modulation of Compound I reactivity.

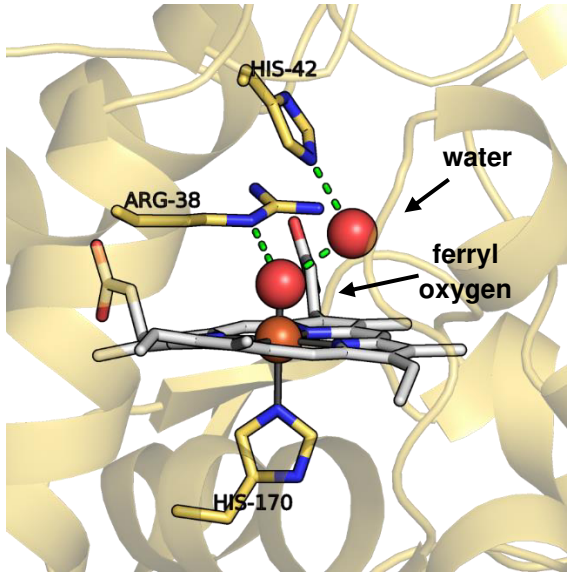

Figure 1.3. X-ray crystal structure of HRP Compound I (PDB ID: 1HCH). Hydrogen bonds involving Arg38 and His42 side-chains are highlighted in green.

Substrate oxidation by peroxidases usually occurs through two separate one-electron steps from Compound I. Peroxidases have been also reported to show peroxygenase activity towards alkene epoxidation[48] and thioether sulfoxidation.[49,50] This reactivity involves the incorporation of one oxygen atom into the product, as in most of the P450-catalysed reactions. One difference with oxygenase activity is that the oxygen atom is derived from peroxide instead of dioxygen. The presence of peroxygenative pathways together with the inactivity towards C–H hydroxylations indicates that H· abstraction cannot be performed by

peroxidases Compound I, and remains a prerogative of Cys-ligated heme enzymes.[51]

1.3. Heme dioxygenases

Heme dioxygenases catalyse the O_2-dependent biological oxidation of tryptophan to *N*-formylkynurenine and comprise tryptophan 2,3-dioxygenases (TDO) and indoleamine 2,3-dioxygenases (IDO).[52]

Differently from P450s, dioxygenases promote the insertion of two oxygen atoms into the substrate and none of the oxygenations is mediated by Compound I.[13] The insertion of the first oxygen atom occurs from the iron-dioxygen adduct and generates Compound II, which is then responsible for the second oxygenation step (Scheme 1.1).

The catalytic mechanism of heme dioxygenases is one of the most long-standing arguments in bioinorganic chemistry. Early mechanistic proposals suggested a base-catalysed mechanism involving deprotonation of the indole nitrogen and no change in the metal oxidation state.[53] This hypothesis was confuted since 1-methyl-Trp analogue was also found to be reactive, which is not consistent with a base-catalysed abstraction mechanism.[54] Since then, many efforts have been done through experimental[55,56] and computational[57,58] approaches. To date, the detailed mechanism is still not established, and two hypotheses have emerged. One possibility involves the electrophilic addition from a ferrous-oxy species to the (most nucleophilic) C3 atom of tryptophan indole ring while the other is a radical addition from a ferric-superoxo species, both leading to Compound II and an epoxide intermediate (Scheme 1.5). Elucidating the nature of the dioxygen adduct is therefore crucial to discriminate between the two pathways.

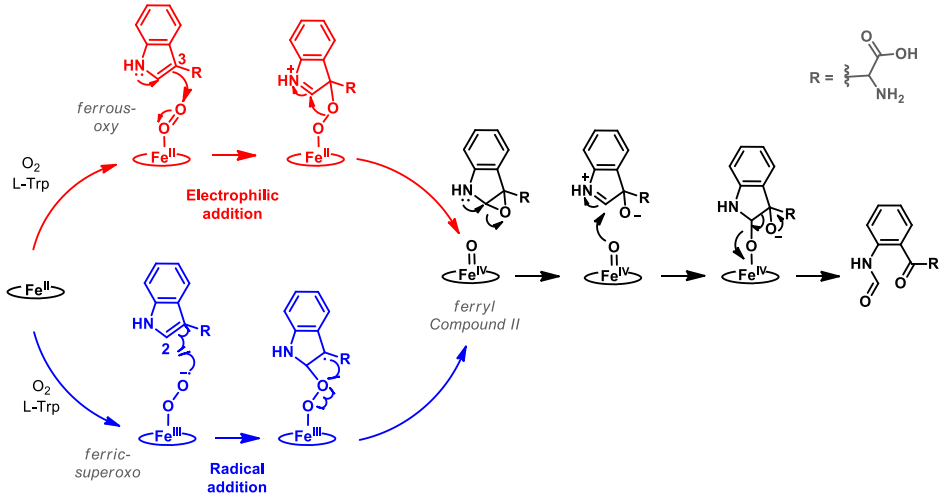

Scheme 1.5 Proposed mechanism of L-Trp oxidation by heme dioxygenases. Electrophilic and radical addition hypotheses for the O–O bond cleavage are highlighted in red and in blue, respectively.

Evidence of a ferric-superoxo species of TDO came from Raman studies,[59] and was recently supported by the crystal structure of TDO with bound O_2 and tryptophan.[60] Structural data from the ternary complex also indicate that oxygen is prone to attack the C2 atom of tryptophan indole ring, which is unlikely to occur in the electrophilic addition pathway. On the other hand, heme modification studies of TDO support the latter mechanism, because more electron-deficient hemes resulted in an increased rate of tryptophan oxidation.[61] Another focal point concerns the different reactivities of TDO and IDO, the latter characterised by a broader substrate specificity. It has been assumed that IDO and TDO react through the same mechanism, although there is no strong evidence that they actually do. Raman studies allowed the identification of IDO Compound II,[62] while it was never isolated during turnovers for TDO. A comparative kinetic study of the two enzymes provided as an explanation that they experience different rate-limiting steps, since the steady-state accumulation of either the ferrous-oxy species or Compound II was observed for TDO and IDO, respectively.[63] The reason for

Compound II accumulation in IDO under multiple turnover conditions has been attributed to an inhibition effect of the substrate. Indeed, differently from TDO, IDO has an additional substrate binding site on the heme proximal side, which can be exploited to tune its enzymatic activity.[64] Despite the recent advances, the molecular mechanism of substrate inhibition remains unclear as well as the detailed dioxygenase mechanism.

The lessons learned so far from the study of natural heme-enzymes are very useful for the design of metallo-porphyrin based catalysts.[18,65] However, there are still some unclear aspects, and the bottom-up approach of model design has demonstrated its proficiency in deepening our understanding of oxygen activation.

2. TOWARDS THE DEVELOPMENT OF ARTIFICIAL HEME-ENZYMES

Bioinorganic chemists attempted to unravel the intricate mechanisms that allow the protein matrix to modulate the catalytic activity of the heme cofactor through the development of synthetic systems.[66] In addition to provide great insight into the effects of that modulate the formation, stability and reactivity of the ferryl heme intermediates, model complexes also represent valuable tools in catalysis.[18,65,66]

Inspired by heme-containing enzymes, numerous research groups have developed metalloporphyrins containing various metals for catalytic oxidation reactions in conjunction with terminal oxidants such as hydrogen peroxide, oxone, hypochlorite, and iodosyl benzene.[67]

Physico-chemical properties of metalloporphyrins, including solubility in aqueous medium, steric and electronic properties can be modulated by chemical modification of the macrocycle. Following this idea, several generations of catalysts have been obtained. The first level of synthetic design involves the introduction of substituents at the periphery of the porphyrin ring (at the *meso* and β-pyrrolic positions). Bulky aromatic groups have been introduced with the aim of improving catalyst stability during oxidation catalysis. In particular, halogenated aryl moieties resulted effective in preventing porphyrin decomposition and the formation of inactive μ-oxo dimers.[68]

Anionic or cationic substituents have been also exploited with the dual purpose of modifying the electronic structure of the porphyrin through electron-withdrawing or electron-donating effects while increasing its solubility in water. Iron and manganese have been mostly employed for the development of these catalytic systems. Cationic iron porphyrins functionalized with *N*-substituted pyridyl moieties have been reported by Groves and co-workers as models of P450 Compound I.[69] These complexes were capable to promote C–H hydroxylations

with high efficiency (k_{cat} = 3.6 × 10^6 M^{-1} s^{-1} for xanthene hydroxylation) following the oxygen rebound mechanism. A number of iron porphyrin derivatives have been studied in the effort to elucidate the chemistry of biological ferryl-oxo species.[70]

Heme synthetic models with axial ligands covalently tethered to the porphyrin have been developed to investigate the effects of axial ligation on reactivity.[71] Efforts have been made to synthesize thiolate-ligated heme models with the goal of mimicking P450 reactivity (Figure 2.1).[72] However, the syntheses of these tethered systems are usually difficult and low-yielding, thus the addition of exogenous ligands has been mainly preferred for this kind of studies.[68,73]

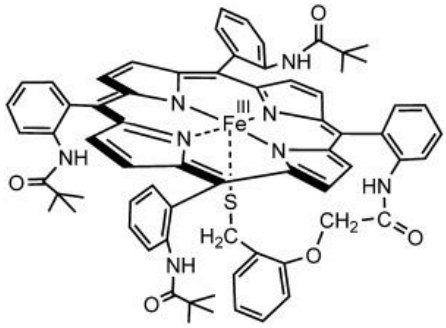

Figure 2.1. An example of a thiolate-bound heme model complex. Adapted with permission from reference [72].

Manganese porphyrins have also been recognized as very efficient catalysts for oxygen-atom transfer reactions.[74] These reactions are promoted by high-valent Mn-oxo species, that are formed through similar mechanisms as described for ferryl-heme intermediates. Mn-porphyrins have been shown to access both the Mn^{V}-oxo and the Mn^{IV}-oxo state.[74–76] The former has been proposed as the active oxidant in the oxygenation of a number of unactivated substrates, similarly to ferryl-oxo Compound I.[77,78] Mn^{IV}-oxo species have attracted less interest in catalysis due to their lower reactivity. A recent study has demonstrated that the reactivity of Mn^{IV}-oxo species is highly sensitive to the nature of the porphyrin substituents and it is enhanced by electron-donating groups. Along these lines,

Nam and co-workers reported the first Mn^{IV}-oxo porphyrin capable of activating C–H bond, promoting oxygenation or halogenation reactions.[79]

A subsequent level of metalloporphyrin design focuses on modulating the environment surrounding the metal centre. Elaborated ligands have been manufactured to create asymmetric environments and/or to assist the activation of oxygen as well as other small-molecule substrates (H_2 or CO_2). Chiral, water soluble manganese porphyrins have been reported to promote the asymmetric epoxidation of aryl alkenes (e.e. up to 68%) and the hydroxylation of aryl alkanes (e.e. up to 57%) with moderate enantioselectivity.[80] Notable examples are the Pacman assemblies, that consist of two porphyrins in a face-to-face arrangement, linked through aromatic bridges of different lengths and flexibility.[81] These systems exploit the cooperativity between two metal centres to carry out multiple electron transfer processes, limiting undesired side-reactions that derive from single-electron transfer events.[82]

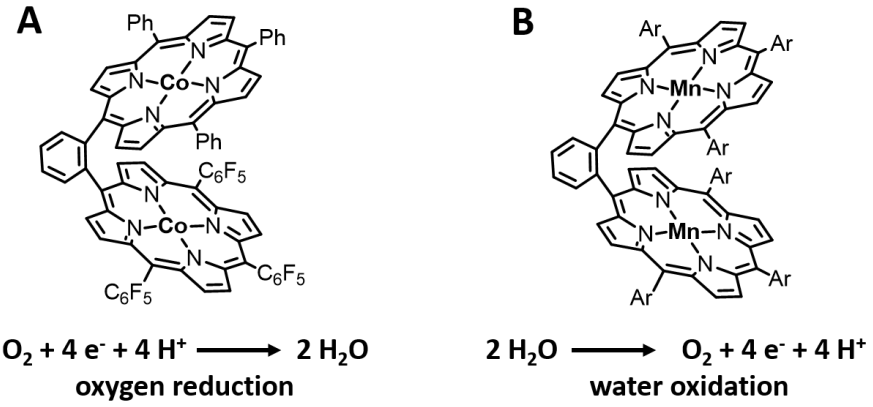

Figure 2.2. (A) Cobalt and (B) Manganese based bis-porphyrin systems for oxygen reduction or water oxidation catalysis. Adapted with permission from references [83] and [84].

Co-derivatives of these bis-porphyrin systems are among the few molecular catalysts capable of mediating the selective four-electron, four-proton reduction of O_2 to water (Figure 2.2A).[83] Mn-containing bis-porphyrin complexes were

demonstrated to efficiently promote O_2 evolution reaction through O-O bond formation from a bis-Mn^V-oxo species (Figure 2.2B).[84]

One of the latest frontiers of metallo-porphyrin design involves the construction of "Hangman" architectures, in which an acid-base hanging group is positioned over the porphyrin to facilitate proton transfer.[85–87] The hanging functionality is meant to mimic the role of distal site residues that assist O–O bond activation in heme enzymes. (Scheme 2.1).[88–90] Nocera and co-workers demonstrated that positioning of the acid/base residue in Hangman complexes allows for the functional modelling of enzymatic "push-pull effects." The hanging acid group directs O−O bond cleavage towards the heterolysis that generates a Compound I-like species, whereas the homolytic cleavage is favoured when the proton transfer is inhibited.[91]

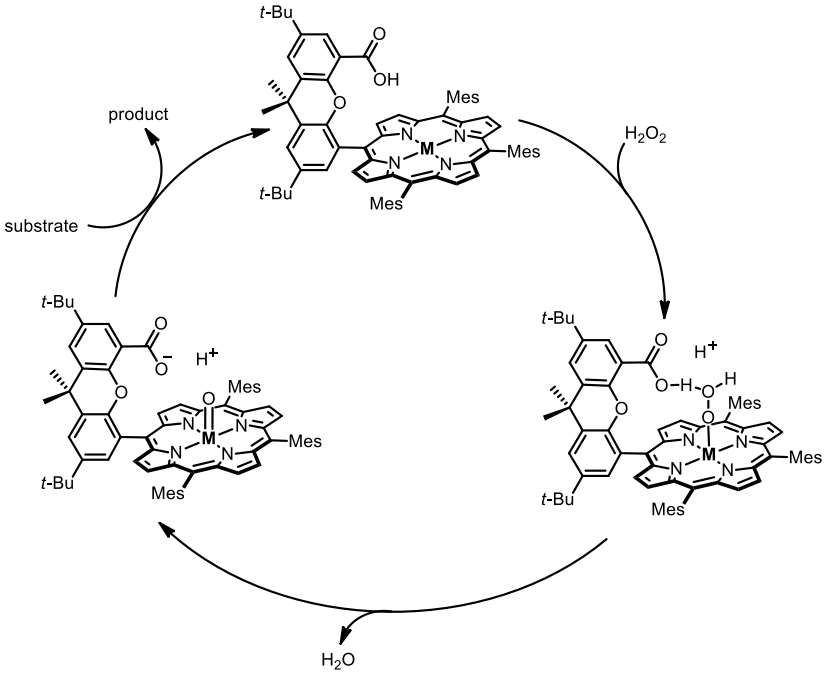

Scheme 2.1 Proposed mechanism for proton-assisted metal-oxo species formation and substrate oxidation by Hangman porphyrins. Reproduced with permission from reference [89].

Despite great progress has been made in developing functional metalloporphyrin complexes, it is still challenging to design a small catalyst with high catalytic efficiency for practical applications.[18] An additional level of complexity around the macrocycle is needed to control substrate recognition, regio- and stereo-selectivity by means of specific second-shell and long-range interactions.[92]

In the last decades, significant advance has been achieved in the design and engineering of protein scaffolds able to accommodate metalloporphyrins and to modulate their reactivity. Peptide-based architectures of different sizes have been used so far for the construction of conjugates with catalytic activity. A variety of strategies have been developed to this end, including noncovalent or covalent anchoring of metallo-porphyrins into natural or designed protein scaffolds.

3. NON-COVALENT PROTEIN/PEPTIDE-PORPHYRIN ASSEMBLIES

The construction of non-covalent protein-porphyrin systems has been successfully approached through the use of protein scaffolds, properly selected to interact with the cofactor. To modulate activity and selectivity, the structure should have a suitable cavity for hosting heme and should be able to tolerate mutations in the metal microenvironment. Different strategies have been developed to this end, involving the use of natural or artificial protein scaffolds.[93–96]

3.1. Incorporation of metallo-porphyrins into non-metal-containing natural proteins

Numerous researchers focused on the insertion of metallo-porphyrins into native proteins that do not contain catalytic metal cofactors. One possible approach to enhance supramolecular association between the metallo-porphyrin and the macromolecular host is to raise antibodies against metallo-porphyrins. Along these lines, Mahy and co-workers developed "hemoabzymes," obtained raising monoclonal antibodies against differently substituted Fe^{III}-*meso*-tetra-phenyl porphyrins and MP8.[97,98] Structural characterization of these systems allowed to carve out several aspects on the interaction between antibodies and metallo-porphyrins and their implications in catalysis. The improved catalytic properties of hemoabzymes compared to the isolated metallo-porphyrins could be ascribed to the protective role of the protein, which prevents catalyst oxidative self-degradation. The conjugate based on MP8 appeared as the best catalyst among hemoabzymes, with a k_{cat}/K_m value only two orders of magnitude lower than HRP. This complex also showed enantioselectivity in thioether sulfoxidation (up to 45% e.e.).[99] The lower reactivity shown by the synthetic metallo-porphyrin conjugates was attributed to the lack of an axial ligand promoting the "push-effect" in H_2O_2 activation. These results clearly highlight the advantages of using antibodies to incorporate synthetic iron-porphyrins for improving the stability and the reactivity of the catalytic site in peroxidase-like reactions. However, they strongly support

that the lack of a distal site environment, properly assisting catalysis, causes poor efficiency.

A different approach to insert a synthetic porphyrin into a protein environment is the so-called "Trojan Horse" strategy.[100] It involves the supramolecular association of a metallo-porphyrin, properly functionalized with a ligand, with a protein able to bind that ligand with high affinity. This strategy has been extensively applied also with catalytic metal complexes different from metallo-porphyrins.[96,101,102]

Highly significant in this field is the work of the Ward group, which exploited the exceedingly high affinity of streptavidin towards biotin for the construction of artificial metallo-enzymes.[103–105] Following this approach, a variety of biotinylated metal complexes have been incorporated into native or mutated streptavidin, leading to artificial enzymes able to perform oxidative or even abiological catalysis.[106–108]

In the context of heme enzymes, the Trojan Horse strategy has been adopted by Mahy and co-workers for the development of "Hemozymes".[97] Taking advantage of the remarkable affinity of a monoclonal antibody for its estradiol antigen, water-soluble Fe^{III}- and Mn^{III}-porphyrins were chemically modified with estradiol and inserted into the anti-estradiol antibody 7A3 (Figure 3.1).[100] Both cationic (TMPyP) and anionic (T*p*SPP) Fe^{III}-porphyrins were able to catalyse the H_2O_2-mediated chemoselective sulfoxidation of thioanisole, even though displaying a small enantiomeric excess (10%).

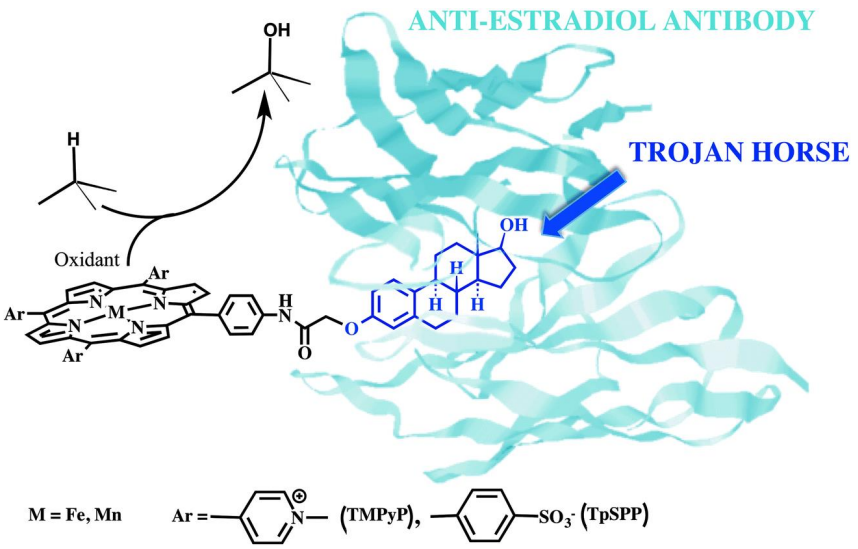

Figure 3.1. Application of the "Trojan Horse" strategy through the insertion of metallo-porphyrin–estradiol conjugates into the anti-estradiol antibody 7A3. Adapted from reference [97] with permission from The Royal Society of Chemistry.

Other proteins were also selected as targets for the development of catalytic hemozymes. The same authors chose neocarzinostatin (NCS) and, in particular, they used the a variant (NCS-3.24) which was previously engineered to shape a binding site for testosterone.[109] Fe^{III}-T*p*SPP covalently conjugated to testosterone was found to bind protein with higher affinity than testosterone alone.[110] The resulting hemozyme catalysed the chemoselective sulfoxidation of thioanisole by H_2O_2, still displaying low enantioselectivity (13% e.e.). Docking analyses revealed that the porphyrin was strongly stabilized by hydrophobic interactions into the protein, displacing testosterone from its binding site. The low enantioselectivity was attributed to partial solvent exposure of the metal centre. These results point out that it is hard to predict the precise arrangement of the porphyrin within the protein host and the role played by the ligand in driving the binding. This possibly represents the main limitation of the Trojan Horse strategy.

More successful for the development of hybrid catalysts active in enantioselective oxidation was the application of the host-guest approach.[92,97] Xylanase A (XlnA)

was selected for the incorporation of anionic Fe^{III}-porphyrins, since the presence of a catalytic site, rich in positive charge, could provide stabilization to the complex through charge-charge interactions.[111,112] The artificial enzyme Fe^{III}-T*p*CPP-XlnA exhibited peroxidase activity towards the oxidation of guaiacol and *o*-dianisidine.[111] Noteworthy, the protein environment induced a moderate enantiomeric excess in the sulfoxidation of thioanisole (40% e.e. (*S*)-sulfoxide).[113] Replacement of iron with manganese also allowed for the epoxidation of aromatic alkenes.[112] Mn^{III}-T*p*CPP-XlnA catalysed the epoxidation of unactivated or poorly activated styrenes (4-chlorostyrene, 4-nitrostyrene, 4-methylstyrene) displaying low enantio-selectivities in favour of the (*S*)-isomer. Interestingly, the epoxidation of 4-methoxystyrene gave a higher and reversal enantioselectivity towards the formation of styrene oxide (80% e.e. (*R*)-isomer).

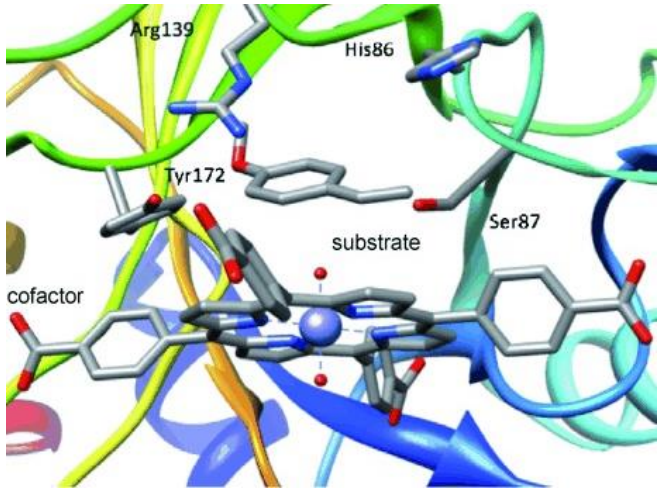

Figure 3.2. Lowest-energy solution of the docking of *p*-methoxystyrene in the artificial Mn(T*p*CPP)-XlnA enzyme. Orientation consistent with the (*R*)-epoxide production. Adapted with permission from reference [112].

Docking simulations confirmed that the formation of the (*S*)-epoxide was slightly energetically favoured during the reaction of styrene and its derivatives into the XlnA active site. For 4-methoxystyrene, a H-bond interaction between a tyrosine residue (Tyr172) and the 4-methoxy group of the substrate could favour the

formation of the (*R*)-epoxide (Figure 3.2), thus highlighting the role of second shell interactions in driving oxidation selectivity.[112]

A similar host-guest approach was adopted by Wang and co-workers, that achieved the construction of an efficient artificial peroxidase by non-covalent anchoring of hemin into the bacterial chapernonine GroEL.[114] GroEL represents an ideal protein cage to host the heme cofactor since it holds a hydrophobic central cavity that could mimic the hydrophobic heme-binding pocket of peroxidases and P450s. The hemin−GroEL complex behaves as an efficient peroxidase mimetic, promoting the decolorization of dyes with H_2O_2 as the oxidant. In this system, GroEL acts as a nano-reaction chamber, since it accommodates multiple guest cofactors (up to 70 in a single protein) in unspecific binding modes and orientations.

3.2. Modification of natural heme-proteins: the case of myoglobin

Parallel to the incorporation of metallo-porphyrins into non-heme containing proteins, the reconstitution of heme-proteins with different cofactors has been approached by several groups.[115,116,95] Indeed, in the absence of a covalent linkage, native heme can be removed from its binding site upon protein denaturation, and the resulting *apo*-protein can be refolded in the presence of a modified cofactor (Figure 3.3). This strategy aims to alter the catalytic properties of the native protein or to implant a novel activity into a catalytically inactive protein. In this context, myoglobin (Mb) has been widely used as a white canvas for "painting" new activities.[95,117,118]

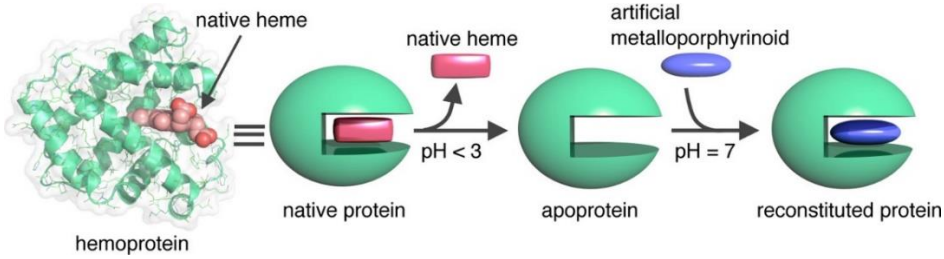

Figure 3.3. Schematic representation of heme-protein reconstitution strategy. Reproduced with permission from reference [95] (*Acc. Chem. Res.* 2019, 52, 4, 945-954). Copyright 2019 American Chemical Society.

Significant in this field is the work of Hayashi's group, which successfully endowed Mb with peroxidase and peroxygenase activity by substitution of native heme with artificial metallo-porphyirinoids. The incorporation of iron porphycene (Fe^{III}-Pc), a constitutional isomer of hemin, turned Mb into an efficient catalyst for the oxidation of guaiacol (peroxidase catalysis), styrene and thioanisole (peroxygenase catalysis).[119] Based on spectroscopic studies, the authors suggested that a stronger coordination of His93, the proximal histidine to the iron ion, and a lower Fe^{3+}/Fe^{2+} reduction potential (- 190 and + 52 mV vs. NHE for Fe^{III}-Pc-Mb and WT-Mb, respectively) accounted for the observed catalytic activity of Fe^{III}-Pc-Mb. Further, swapping iron to manganese led to Mn^{III}-Pc-Mb, which was able

to catalyse the H_2O_2-dependent alkane hydroxylation, converting ethylbenzene in 1-phenylethanol as a single product.[120,121]

Among reconstitution strategies involving metal ion replacement, it is noteworthy to recall the outstanding results by Hartwig and co-workers,[118] who exploited the reconstitution of Mb with metals other than iron, with the aim of expanding the catalytic properties of heme-proteins towards abiological chemistry.[122] An array of myoglobins containing mutations at His93 were obtained and reconstituted with Co-, Cu-, Mn-, Rh-, Ir-, Ru-, or Ag-containing porphyrins. In some cases, these cofactors contained organic co-ligands (a CO or a methyl group) bound to the metal ion. The resulting artificial enzymes were investigated as catalysts for the intra-molecular cyclization of diazo-compounds *via* carbene chemistry and the Ir(Me)-reconstituted proteins displayed the highest reactivity. However, the products of the Ir(Me)-Mb catalysed reactions were nearly racemic and moderate turnover numbers (60-100 TON) were observed. Modification of the protein scaffold by both site-directed mutagenesis and directed evolution led to significant improvements of reactivity and selectivity, achieving an artificial enzyme able to perform over 7000 TON in carbene C–H insertion with high enantioselectivity (84% e.e.).[122]

Rational engineering of the myoglobin scaffold was successfully exploited by Lu and co-workers for the construction of additional metal binding sites.[94] The incorporation of a nonheme iron centre, through the introduction of three histidines and one glutamate in the distal pocket of myoglobin, afforded a mimic of nitric oxide reductases (NORs).[123–125] The engineered enzyme, Fe_B-Mb (Figure 3.4A), not only represents a structural model of the heme–nonheme diiron centre of NORs, but also reproduces the function of the natural counterparts, by selectively reducing nitric oxide to nitrous oxide.[123–125] The same group also engineered myoglobin to host a non-heme copper binding site, leading to a heme-

copper oxidase (HCO) model. Differently from heme oxygenases, HCOs do not couple the reduction of O_2 to the oxidation of exogenous substrates, while generate a transmembrane proton gradient which is essential for the biosynthesis of adenosine triphosphate (ATP) [126]. Notably, the engineered Cu_B-Mb (Figure 3.4B) was able to perform over one thousand turnovers without releasing ROS during catalysis.[127]

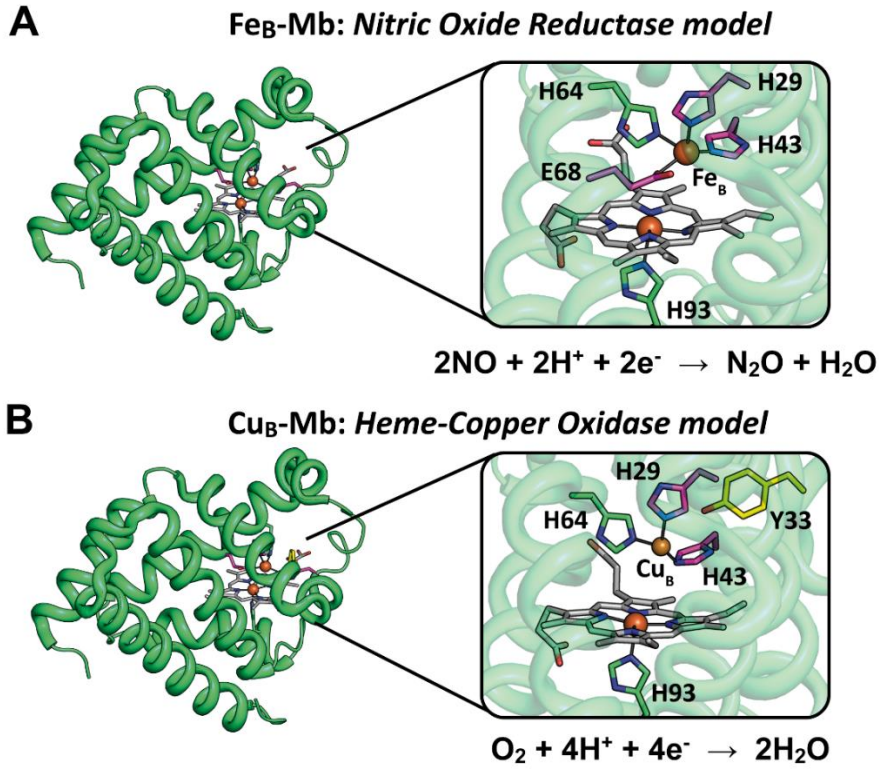

Figure 3.4. X-ray structures of: (A) the Mb-based NOR model (Fe_B-Mb; PDB-code: 3K9Z) and (B) the Mb-based HCO model (Cu_BMb; PDB code: 4FWY) with a focus on the active sites. Side-chains of the mutated residues are highlighted in magenta. Reactions catalysed by each enzyme are also reported. Adapted with permission from reference [93].

The active sites of NORs and HCOs are highly homologous, since they simply differ for the nature of the nonheme metal ion. The reasons why copper was selected for O_2 reduction in HCOs and iron was selected for NO reduction in

NORs could not be clearly established. Indeed, the study of structure-to-function relationships in native HCOs, as well as in native NORs, is hampered by their large size and membranous nature. Metal-substitution studies with Mb-based artificial enzymes allowed to achieve a deep insight into the catalytic mechanism of their natural counterparts, evidencing a correlation between the electronic configurations of the metal ions and their effectiveness in facilitating the O–O bond cleavage.[128] Diverse site-directed mutants were also obtained by introducing secondary sphere perturbations or heme modifications, aimed at evaluating the effect of altering the heme reduction potential[129,130] and the role of proton transfer residues[131] on enzymatic activity. Through these studies, Lu and co-workers deciphered the factors responsible for fine modulation of the NOR/HCO activity in the natural enzymes, which would be useful for the development of artificial catalytic systems.

3.3. *De novo* protein scaffolds

Artificial protein platforms have also been exploited for the construction of functional heme-enzymes. Most of the work in this area has been focused on introducing heme-binding sites into *de novo* designed α-helical bundles.[132] The α-helical bundle is a widespread structural motif among heme and nonheme metalloproteins.[133] A great degree of confidence in the design and engineering of helical bundles has been reached over the years.[134] Therefore, these structural motifs have been extensively adopted for the incorporation of metal binding sites other than heme, including iron-sulphur clusters,[135,136] zinc,[137,138] copper[139,140] and diiron centres.[141,142]

In the first pioneering work, DeGrado and co-workers designed a four-helix bundle capable of incorporating a heme group into the protein interior.[143] Afterwards, Dutton and co-workers reached impressive results in the development of four-helix bundles, named *maquettes*, which can host diverse redox-active

cofactors and reproduce the function of electron transfer proteins.[144–150] Remarkably, engineering of the *maquette* scaffold also led to the construction of an artificial oxygen-binding heme-protein that displays higher affinity towards O_2 than CO.[151] Oxidation catalysis by non-covalent heme-binding *maquettes* has not been reported so far, while it will be described for covalently bound systems.

Efforts to develop artificial heme-proteins by *de novo* design has experienced significant progress in the last decades. Despite the majority of designed metallo-enzymes are based on α-helical scaffolds, *de novo* design of multi-stranded, heme-binding, β-sheet peptides, was recently reported.[152,153] Even though the peroxidase activity of the designed catalysts was far from those of natural enzymes, this work represents a milestone towards the design of synthetic proteins functioning in membranes.

Moving from small-sized protein models towards supramolecular structures, Fry and co-workers recently reported the incorporation of heme b into self-assembling *de novo* designed peptide scaffolds.[154] The supramolecular peptide structure could adopt different morphologies that are stabilized in different pH conditions (Figure 3.5), with the micelles favoured in neutral-acidic conditions and the nano-fibers favoured in alkaline conditions. Remarkably, changes in the supramolecular structure could be used to modulate heme coordination properties and reactivity.

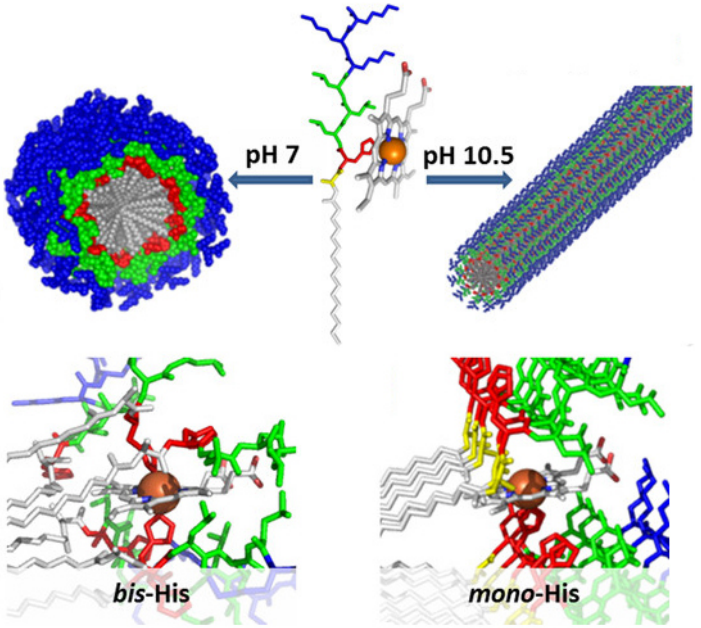

Figure 3.5. Representation of pH-driven stabilization of different morphologies in self-assembling peptides. Micelle formation at pH 7 leads to a bis-His heme, while nano-fibers at pH 10.5 leads to a five-coordinate, mono-His heme. Adapted from reference [154].

4. COVALENT PROTEIN/PEPTIDE-PORPHYRIN CONJUGATES

Covalent ligation between the porphyrin and the peptide scaffold has the advantage of preventing cofactor or axial ligand dissociation and scrambling. Following this idea, several goals in the construction of this kind of catalysts have been achieved.[65]

Functionalization of Mn-porphyrins with biomolecules has been widely exploited in the construction of functional anti-oxidants. Owing to the ability of simple Mn-porphyrin systems to act as superoxide dismutase (SOD) mimics, Asayama and coworkers developed Mn-porphyrin-peptide conjugates intended to protect cells under oxidative stress conditions (Figure 4.1).[155] In this case, the functionalization was simply aimed at improving the efficiency of the complex delivery to specific cellular targets, and it did not greatly affect the reactivity of the porphyrin alone.

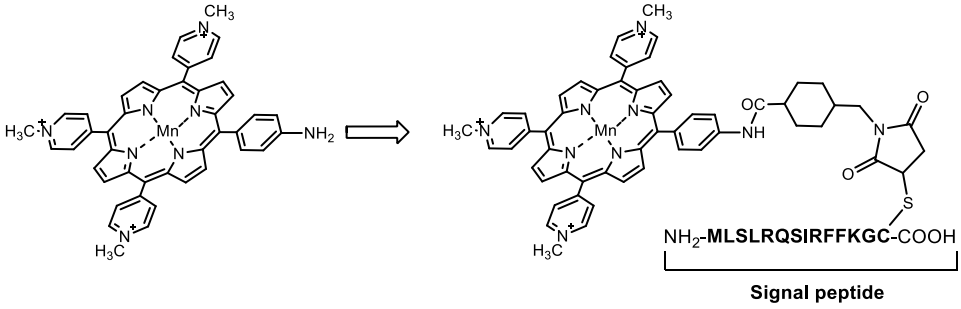

Figure 4.1. Mn-porphyrin-oligopeptide conjugate with SOD activity. Adapted with permission from reference [155].

Umezawa and coworkers reported the functionalization of a Mn-porphyrin at *meso* positions with small peptide fragments to provide artificial catalases.[156] Several analogues were synthesized by varying the peptide sequence, using a combinatorial rather than a rational approach. Even though only slight improvements were observed with respect to the unbound porphyrin, functional selectivity towards catalase or peroxidase activity could be achieved by introducing positively or negatively charged residues.

For catalytic purposes, it is crucial to rule on the parameters that affect both the reactivity and the selectivity of the metal centre. Therefore, diverse peptide-based architectures have been constructed in the effort of recreating, into smaller systems, the first and second-shell interactions that allow for the modulation of the heme reactivity in metallo-enzymes.

Possibly the most well-known examples of covalent peptide-porphyrin conjugates are Microperoxidases (MPs).[157] MPs result from the proteolytic cleavage of cytochromes c, thus they cannot be strictly classified as artificial systems. They consist of a short peptide chain containing a Cys-Xxx-Xxx-Cys motif that provides two cysteine residues involved in the chemical ligation with the heme moiety. Among MPs, the most studied are MP8 and MP11, in which the peptide fragment consists of eight and eleven amino acid residues, respectively. Both these complexes retain a histidine residue which acts as proximal ligand to the heme iron. Differently from the parent cytochromes, in MPs the sixth coordination position is not occupied by peptide-derived ligands, giving rise to a five-coordinate metal site. These features provide them with the minimal structural requirements for peroxidase activity.

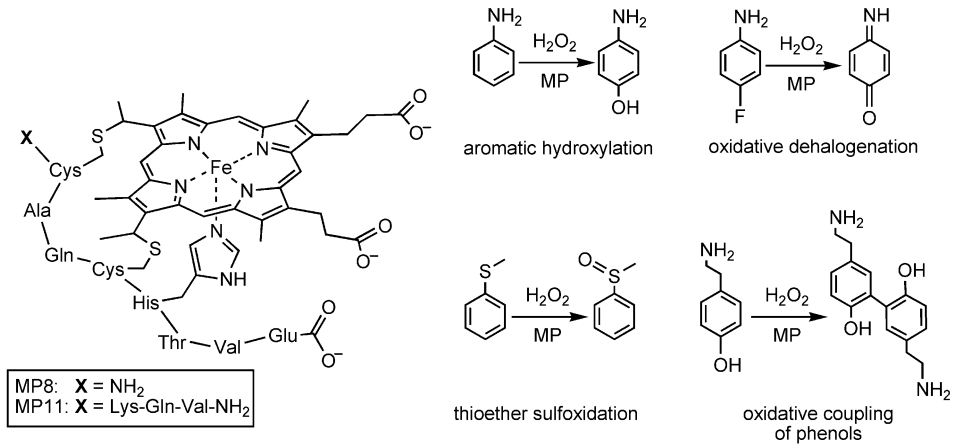

Figure 4.2. Molecular structure of microperoxidases and some examples of reactions that they catalyse.

MP8, MP11 and their derivatives have been extensively studied to promote oxidation and oxygenation reactions by activation of hydrogen peroxide, including aromatic hydroxylation,[158] oxidative dehalogenation,[159] tioether sulfoxidation[160,161] and the oxidative coupling of phenolic substrates[162,163] (Figure 4.2).

Solvent exposure of the heme distal site accounts for the ability of MPs to easily bind and oxidize substrates, but also represents a major limitation to their practical use as catalysts. Indeed, degradation pathways usually occur during oxidation catalysis, leading to rapid bleaching of the porphyrin. One strategy that has been adopted to prevent catalyst self-inactivation is the replacement of iron with manganese, owing to the increased stability of the manganyl-oxo species compared to the corresponding iron analogues.[164,165] Metal substitution in MP8 led to a substantial decrease in peroxidase and peroxygenase activity. Therefore, Mn-MPs are even less attractive for catalytic purposes. An additional limitation in the catalytic application of MPs is their tendency to aggregate even at micromolar concentrations in water.[166,167] Some research groups reasoned to take advantage of the high accessibility of the heme in MPs for the immobilization onto surfaces. Accordingly, MP8 and MP11 have been exploited in the construction of biosensors for the detection of peroxides and aromatic compounds.[168] More recently, Sicard, Ricoux and co-workers reported the encapsulation of MP8 into a metal organic framework (MOF) as an efficient strategy to enhance catalyst robustness in the oxidation of organic dyes.[169] The MOF matrix not only exerts a protective role against catalyst deterioration, but can also be exploited to selectively enhance the degradation of positively or negatively charged substrates depending on the pH. These achievements point out the importance of a supramolecular host in tuning the reactivity of the metal centre through specific interactions.

The design and construction of fully synthetic peptide-porphyrin conjugates has been devoted to the development of complexes with improved catalytic properties. In this respect, the use of four-helix bundles as protein scaffold to host metallo-porphyrins has been widely reported.[145,170,171] Among them, Mini-Peroxidase 3 (MP3) was designed using the heme-binding motif of bacterioferritin (BFR) as a template. The original sequence was modified to build an asymmetric sandwiched structure in which two helix-loop-helix units are covalently bound to the porphyrin (Figure 4.3).[172] Like microperoxidases, MP3 was characterised by a five-coordinate heme, able to accommodate exogeneous substrates. Moreover, an Arg residue was introduced into the distal site, since it is known to assist hydrogen peroxide activation in HRP.[44] Fe^{III}-MP3 behaved as an efficient catalyst towards peroxidase reactions (k_{cat}/K_m = 1.57 ×10^6 $M^{-1}s^{-1}$ for the oxidation of ABTS), even though it did not approach the activity of the natural counterpart.

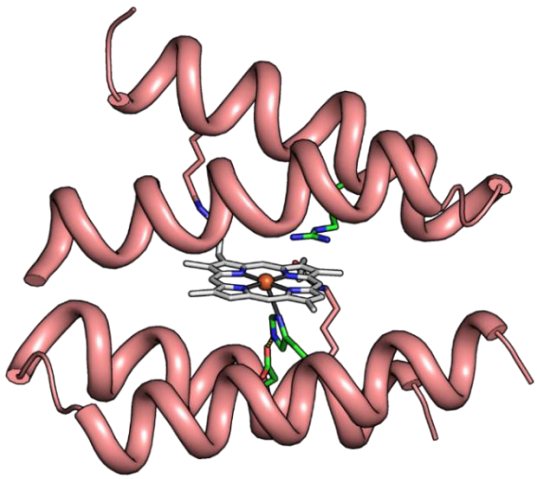

Figure 4.3. Molecular model of Fe^{III}-MP3 with key residues of the first and second coordination spheres depicted in green.

Impressive results were reported by Anderson and co-workers in the context of designed peroxidase models. In a recent paper, the authors describe the construction of an artificial heme-binding *maquette* able to efficiently catalyse

oxidation reactions using H_2O_2.[173] Anderson's group demonstrated that *maquettes* can be recognized and modified by the post-translational cytochrome c maturation system of *E. Coli* for covalent heme incorporation *in vivo*, giving rise to the "*c*-type cytochrome maquettes" (CTMs).[174] Starting from a six-coordinated, non-catalytic CTM, a mono-histidine peroxidase-like heme active site was introduced through a few-steps design process (Figure 4.4). The resulting enzyme, named C45, displays one of the highest catalytic efficiencies (k_{cat}/K_m= 3.20 ×10^6 $M^{-1}s^{-1}$ in the ABTS oxidation) among the artificial peroxidases developed so far, also retaining its activity at high temperatures.

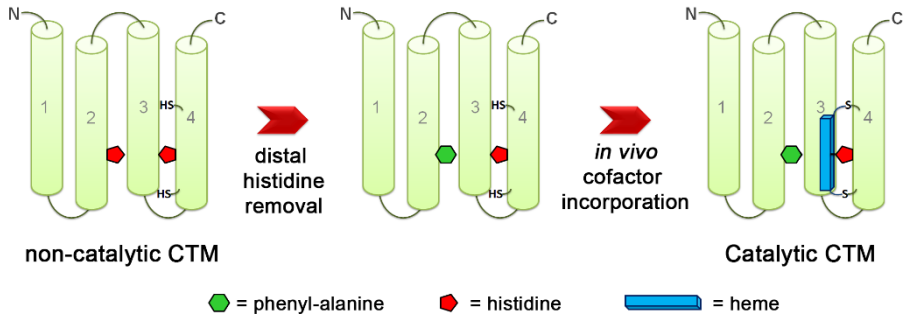

Figure 4.4. Design process for the construction of *c*-type cytochrome maquettes (CTMs). Reproduced from reference [130].

The lack of a rationally designed binding site for substrate recognition gives to C45 the ability to promote the oxidation of a wide array of substrates, including guaiacol, luminol, *o*-phenylenediamine and 2,4,6-trihalophenols. Lately, C45 has been also reported to provide abiological carbene-trasferase activity, affording a variety of diverse substrate functionalizations with notable efficiency and stereo-selectivity.[175] In particular it appears as the first biocatalyst, among natural and artificial enzymes, capable to promote ring expansion of heterocycles by carbene-transfer.

4.1. Miniaturized heme-enzymes: Mimochromes

Mimochromes represent notable examples of covalent peptide-porphyrin conjugates with catalytic activity. Differently from the *de novo* proteins described above, Mimochromes have been designed following a miniaturization approach. The concept of this strategy is the selection of the smallest peptide sequence from a target enzyme that allows for an accurate reconstruction of the active-site structure and function.

The prototype molecule, Mimochrome I (MC1), was designed taking inspiration from the hemoglobin active site. Two identical nonapeptides are covalently linked to the propionic groups of a deuteroporphyrin though the ε-amino groups of lysine residues, giving rise to a helix-heme-helix sandwiched structure. The F helix of hemoglobin β-chain was employed as a template for the peptide sequence.[176]

Each peptide bears a histidine that acts as axial ligand to the heme iron, leading to a *bis*-His coordination complex.[177] Starting from MC1, a careful re-design process has been carried out to improve structural and functional properties, and numerous analogues have been obtained. In particular, two design strategies were adopted to increase the water-solubility of the complex. The first approach focused on the elongation of the peptide chains from 9 to 14 amino-acids residues in the C-terminal regions and led to MC2.[178] The other strategy focused in the modification of the MC1 sequence to introduce stabilizing interactions and led to MC4.[179] The introduction of arginine and glutamate residues at the N- and the C-termini of the peptides allowed for the formation of ionic pairs between the charged residues in MC4. The latter displayed a solubility in the range of 10^{-3} M in aqueous solution and a very stable structure. It also represents the first miniaturized protein for which both NMR[179] and X-ray crystal structure[180] (in the Co^{III}-complex) have been solved, displaying inter-helical interactions in solution and intra-helical interactions in the solid state (Figure 4.5).

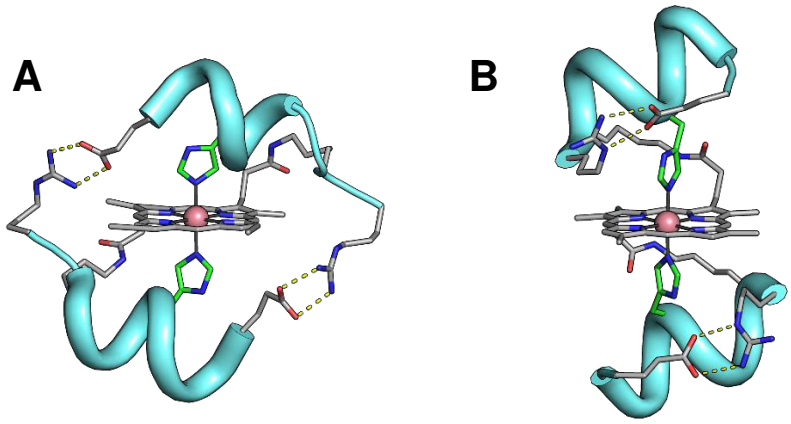

Figure 4.5. (A) Solution NMR (PDB ID: 1VL3) and (B) X-ray crystal (PDB ID: 1PYZ) structures of Co^{III}-MC4.

Taking account from the symmetrical six-coordinated complexes, subsequent design has been focused on creating a five-coordinated heme site, apt to perform oxidative catalysis. To this aim, the sequences of MC2 and MC4 were combined. In particular, a tetradeca-peptide (*TD*) chain, derived from MC2 and bearing a His coordinating residue was employed to construct the heme proximal site. A decapeptide (*D*) lacking metal-coordinating residues was obtained from MC4 upon substitution of the histidine with a serine residue. This allowed to create a substrate binding pocket on the distal side of the heme. The ionic pairs between Arg and Glu were conserved from MC4 in the new analogue, called MC6. MC6 was the first analogue to show peroxidase-like activity in its Fe^{III}-complex.[181,182] Unlike its precursors, MC6 mimics the asymmetry of natural proteins in both primary and secondary coordination spheres (Figure 4.6A). Fe^{III}-MC6 behaves as an efficient artificial peroxidase, since it catalyses the oxidation of ABTS with a catalytic efficiency ($k_{cat}/K_m = 4.42 \times 10^6\ M^{-1}\ s^{-1}$) comparable to that of HRP ($k_{cat}/K_m = 5.8 \times 10^6\ M^{-1}\ s^{-1}$) in the conditions of maximal activity for each catalyst. Fe^{III}-MC6 also converts phenol to 2- and 4-nitrophenol in presence of H_2O_2 and NO_2^-, with high reaction yields. In order to elucidate the role of the distal helix on the

functional properties of Fe^{III}-MC6, the reactivity of the derivative lacking the *D* chain was also evaluated. The *TD*-porphyrin conjugate showed a decreased apparent affinity (K_m) towards both the substrate (ABTS) and co-substrate (H_2O_2), indicating that the decapeptide may assist their binding. Moreover, in spite of an increased k_{cat}, the mono-peptide conjugate was more susceptible to oxidative degradation, as it performed a lower turnover number.

In order to further enhance the catalytic performances of Fe^{III}-MC6, the effect of specific amino-acid mutations was investigated. Particular attention was devoted to the charged residues in the N- and C-terminal regions of the peptide chains (Glu^2 and Arg^{10}), which were intended to stabilize the tertiary structure through inter-chain electrostatic interactions. Disruption of one ionic pair was thought to increase the flexibility of the structure, thus providing higher substrate accessibility to the catalytic site. The Glu^2Leu mutation in the *TD* chain also left unpaired the Arg^{10} on the distal side of the heme, mimicking Arg^{38} of HRP. This new analogue, named Fe^{III}-MC6* (Figure 4.6B) displayed a 4-fold enhancement of the catalytic efficiency in the ABTS oxidation ($k_{cat}/K_m = 1.6 \times 10^7\ M^{-1}\ s^{-1}$), overcoming that of HRP.[183]

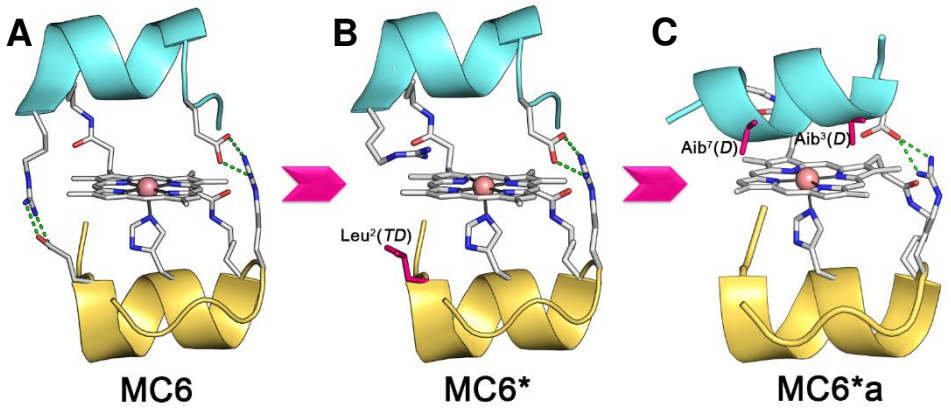

Figure 4.6. Designed models of MC6 catalysts: (A) MC6; (B) MC6*; (C) MC6*a. The residues that have been mutated in each round of redesign are highlighted in magenta.

More recently, the robustness of MC6 scaffold was further increased by modification of the distal peptide chain. Taking advantage of the use of noncoded α-amino acids as conformational constraints, the simplest Cα,Cα-disubstituted amino acid, 2-aminoisobutyric acid (Aib, U), was selected to reduce backbone flexibility and to favour helical folding.[184–186] Positions 3 and 7 of the *D* chain were selected for the insertion of two Aib residues, since they do not include residues involved in structural stabilization or catalysis. Further, according to the designed model, these positions place the two amino acid side-chains facing towards the deuteroheme, thus stabilizing the global sandwich topology.[187] The resulting compound, named Fe^{III}-MC6*a (Figure 4.6C), behaves as the best artificial peroxidase catalyst known so far, displaying a 20-fold higher catalytic efficiency ($6.4 \times 10^7\ M^{-1}\ s^{-1}$) with respect to HRP in the ABTS oxidation and a double turnover number compared to its precursor. Moreover, the cobalt derivative (Co-MC6*a) behaves as a very promising catalyst in hydrogen evolution reactions, as it is able to electrocatalytically reduce protons to hydrogen (H_2) in water at neutral pH under aerobic conditions, performing more than 230,000 turnovers.[188]

5. AIM OF THE PROJECT

This PhD project is aimed at obtaining artificial heme-enzymes, based on designed protein scaffolds, able to promote oxidation reactions with high efficiency and selectivity.

The recent achievements obtained with Fe-MC6*a towards peroxidase catalysis and Co-MC6*a in promoting the hydrogen evolution reaction, prompted us to further evaluate the versatility of the MC6*a scaffold towards metal replacement, by swapping iron to manganese. Accordingly, the preparation, spectroscopic and redox characterization of Mn-MC6*a has been performed.

Iron- and manganese-porphyrins have rich redox chemistry and they generate common metal-oxo species upon activation of oxygen or hydrogen peroxide. As outlined in the previous sections, both Fe- and Mn-porphyrins have been found to promote a variety of synthetically relevant transformation. Their conjugation to peptide or protein-based scaffold represents a valuable tool for the modulation of their catalytic properties.

Taking advantage of the catalytic promiscuity of metallo-porphyrin systems, the research activity has been focused on expanding the repertoire of transformations accessible by MC6*a complexes in oxidation chemistry. To this end, the ability of Mn- and Fe-MC6*a in promoting the oxy-functionalization of organic substrates has been evaluated. First, phenyl thioethers were chosen as model substrates for oxygen transfer reactions. Further, indole oxidation was studied with the dual purpose of investigating the catalyst site-selectivity and to produce added value products.

6. REFERENCES

1. Hess, C. R., Welford, R. W. D. & Klinman, J. P. Oxygen-Activating Enzymes, Chemistry of. in *Wiley Encyclopedia of Chemical Biology* 1–12 (American Cancer Society, 2008).
2. Klinman, J. P. How do enzymes activate oxygen without inactivating themselves? *Acc. Chem. Res.* **40,** 325–333 (2007).
3. Jasniewski, A. J. & Que, L. Dioxygen Activation by Nonheme Diiron Enzymes: Diverse Dioxygen Adducts, High-Valent Intermediates, and Related Model Complexes. *Chem. Rev.* **118,** 2554–2592 (2018).
4. Itoh, S. & Fukuzumi, S. Monooxygenase Activity of Type 3 Copper Proteins. *Acc. Chem. Res.* **40,** 592–600 (2007).
5. Decker, A. & Solomon, E. I. Dioxygen activation by copper, heme and non-heme iron enzymes: comparison of electronic structures and reactivities. *Curr. Opin. Chem. Biol.* **9,** 152–163 (2005).
6. Poulos, T. L. Heme Enzyme Structure and Function. *Chem. Rev.* **114,** 3919–3962 (2014).
7. Huang, X. & Groves, J. T. Oxygen Activation and Radical Transformations in Heme-proteins and Metalloporphyrins. *Chem. Rev.* **118,** 2491–2553 (2018).
8. Raven, E. & Dunford, B. *Heme Peroxidases*. (The Royal Society of Chemistry, 2016).
9. Ortiz de Montellano, P. R. *Cytochrome P450: Structure, Mechanism, and Biochemistry*. **1,** (Springer International Publishing, 2015).
10. Raven, E. L. A short history of heme dioxygenases: rise, fall and rise again. *J Biol Inorg Chem* **22,** 175–183 (2017).
11. Krest, C. M., Onderko, E. L., Yosca, T. H., Calixto, J. C., Karp, R. F., Livada, J., Rittle, J. & Green, M. T. Reactive Intermediates in Cytochrome P450 Catalysis. *J. Biol. Chem.* **288,** 17074–17081 (2013).
12. Moody, P. C. E. & Raven, E. L. The Nature and Reactivity of Ferryl Heme in Compounds I and II. *Acc. Chem. Res.* **51,** 427–435 (2018).
13. Efimov, I., Basran, J., Thackray, S. J., Handa, S., Mowat, C. G. & Raven, E. L. Structure and Reaction Mechanism in the Heme Dioxygenases. *Biochemistry* **50,** 2717–2724 (2011).
14. Hersleth, H.-P., Ryde, U., Rydberg, P., Görbitz, C. H. & Andersson, K. K. Structures of the high-valent metal-ion haem-oxygen intermediates in peroxidases, oxygenases and catalases. *J. Inorg. Biochem.* **100,** 460–476 (2006).
15. Blomberg, M. R. A. & Ädelroth, P. The mechanism for oxygen reduction in cytochrome c dependent nitric oxide reductase (cNOR) as obtained from a combination of theoretical and experimental results. *Biochim. Biophys. Acta Bioenerg.* **1858,** 884–894 (2017).

16. Alfonso-Prieto, M., Biarnés, X., Vidossich, P. & Rovira, C. The molecular mechanism of the catalase reaction. *J. Am. Chem. Soc.* **131,** 11751–11761 (2009).
17. Wikström, M., Krab, K. & Sharma, V. Oxygen Activation and Energy Conservation by Cytochrome c Oxidase. *Chem. Rev.* **118,** 2469–2490 (2018).
18. Baglia, R. A., Zaragoza, J. P. T. & Goldberg, D. P. Biomimetic Reactivity of Oxygen-Derived Manganese and Iron Porphyrinoid Complexes. *Chem. Rev.* **117,** 13320–13352 (2017).
19. Bernhardt, R. Cytochromes P450 as versatile biocatalysts. *J. Biotechnol.* **124,** 128–145 (2006).
20. Guengerich, F. P. Mechanisms of Cytochrome P450-Catalyzed Oxidations. *ACS Catal.* **8,** 10964–10976 (2018).
21. Munro, A. W., Girvan, H. M., Mason, A. E., Dunford, A. J. & McLean, K. J. What makes a P450 tick? *Trends Biochem. Sci.* **38,** 140–150 (2013).
22. Daff, S. N., Chapman, S. K., Holt, R. A., Govindaraj, S., Poulos, T. L. & Munro, A. W. Redox Control of the Catalytic Cycle of Flavocytochrome P-450 BM3. *Biochemistry* **36,** 13816–13823 (1997).
23. Schlichting, I., Berendzen, J., Chu, K., Stock, A. M., Maves, S. A., Benson, D. E., Sweet, R. M., Ringe, D., Petsko, G. A. & Sligar, S. G. The catalytic pathway of cytochrome p450cam at atomic resolution. *Science* **287,** 1615–1622 (2000).
24. Nagano, S. & Poulos, T. L. Crystallographic Study on the Dioxygen Complex of Wild-type and Mutant Cytochrome P450cam: implications for the dioxygen activation mechanism. *J. Biol. Chem.* **280,** 31659–31663 (2005).
25. Tripathi, S., Li, H. & Poulos, T. L. Structural basis for effector control and redox partner recognition in cytochrome P450. *Science* **340,** 1227–1230 (2013).
26. Rittle, J. & Green, M. T. Cytochrome P450 compound I: capture, characterization, and C-H bond activation kinetics. *Science* **330,** 933–937 (2010).
27. Groves, J. T. & Van der Puy, M. Stereospecific aliphatic hydroxylation by iron-hydrogen peroxide. Evidence for a stepwise process. *J. Am. Chem. Soc.* **98,** 5290–5297 (1976).
28. Huang, X. & Groves, J. T. Beyond ferryl-mediated hydroxylation: 40 years of the rebound mechanism and C-H activation. *J. Biol. Inorg. Chem.* **22,** 185–207 (2017).
29. Cryle, M. J., Ortiz de Montellano, P. R. & De Voss, J. J. Cyclopropyl Containing Fatty Acids as Mechanistic Probes for Cytochromes P450. *J. Org. Chem.* **70,** 2455–2469 (2005).
30. Ortiz de Montellano, P. R. Hydrocarbon Hydroxylation by Cytochrome P450 Enzymes. *Chem. Rev.* **110,** 932–948 (2010).

31. Yosca, T. H., Rittle, J., Krest, C. M., Onderko, E. L., Silakov, A., Calixto, J. C., Behan, R. K. & Green, M. T. Iron(IV)hydroxide pKa and the Role of Thiolate Ligation in C–H Bond Activation by Cytochrome P450. *Science* **342,** 825–829 (2013).
32. Groves, J. T. Enzymatic C-H bond activation: Using push to get pull. *Nat. Chem.* **6,** 89–91 (2014).
33. Kwon, H., Basran, J., Casadei, C. M., Fielding, A. J., Schrader, T. E., Ostermann, A., Devos, J. M., Aller, P., Blakeley, M. P., Moody, P. C. E. & Raven, E. L. Direct visualization of a Fe(IV)–OH intermediate in a heme enzyme. *Nat. Commun.* **7,** 1–6 (2016).
34. Yosca, T. H., Langston, M. C., Krest, C. M., Onderko, E. L., Grove, T. L., Livada, J. & Green, M. T. Spectroscopic Investigations of Catalase Compound II: Characterization of an Iron(IV) Hydroxide Intermediate in a Non-thiolate-Ligated Heme Enzyme. *J. Am. Chem. Soc.* **138,** 16016–16023 (2016).
35. Dunford, H. B. *Peroxidases and Catalases: Biochemistry, Biophysics, Biotechnology and Physiology*. (John Wiley & Sons, 2010).
36. Chmièlnicka, J., Ohlsson, P.-I., Paul, K.-G. & Stigbrand, T. Substrate specificity of plant peroxidases. *FEBS Lett.* **17,** 181–184 (1971).
37. Gajhede, M. Plant peroxidases: substrate complexes with mechanistic implications. *Biochem. Soc. Trans.* **29,** 91–99 (2001).
38. Harbury, H. A. Oxidation-Reduction Potentials of Horseradish Peroxidase. *J. Biol. Chem.* **225,** 1009–1024 (1957).
39. Battistuzzi, G., Bellei, M., Zederbauer, M., Furtmüller, P. G., Sola, M. & Obinger, C. Redox Thermodynamics of the Fe(III)/Fe(II) Couple of Human Myeloperoxidase in Its High-Spin and Low-Spin Forms. *Biochemistry* **45,** 12750–12755 (2006).
40. Taylor, J. F. & Morgan, V. E. Oxidation-Reduction Potentials of the Metmyoglobin-Myoglobin System. *J. Biol. Chem.* **144,** 15–20 (1942).
41. Efimov, I., Parkin, G., Millett, E. S., Glenday, J., Chan, C. K., Weedon, H., Randhawa, H., Basran, J. & Raven, E. L. A simple method for the determination of reduction potentials in heme-proteins. *FEBS Lett.* **588,** 701–704 (2014).
42. Rodríguez-López, J. N., Lowe, D. J., Hernández-Ruiz, J., Hiner, A. N. P., García-Cánovas, F. & Thorneley, R. N. F. Mechanism of Reaction of Hydrogen Peroxide with Horseradish Peroxidase: Identification of Intermediates in the Catalytic Cycle. *J. Am. Chem. Soc.* **123,** 11838–11847 (2001).
43. Erman, J. E., Vitello, L. B., Miller, M. A., Shaw, A., Brown, K. A. & Kraut, J. Histidine 52 is a critical residue for rapid formation of cytochrome c peroxidase compound I. *Biochemistry* **32,** 9798–9806 (1993).

44. Rodriguez-Lopez, J. N., Smith, A. T. & Thorneley, R. N. F. Role of Arginine 38 in Horseradish Peroxidase: a critical residue for substrate binding and catalysis. *J. Biol. Chem.* **271,** 4023–4030 (1996).
45. Poulos, T. L. & Kraut, J. The stereochemistry of peroxidase catalysis. *J. Biol. Chem.* **255,** 8199–8205 (1980).
46. Berglund, G. I., Carlsson, G. H., Smith, A. T., Szöke, H., Henriksen, A. & Hajdu, J. The catalytic pathway of horseradish peroxidase at high resolution. *Nature* **417,** 463–468 (2002).
47. Meharenna, Y. T., Doukov, T., Li, H., Soltis, S. M. & Poulos, T. L. Crystallographic and single-crystal spectral analysis of the peroxidase ferryl intermediate. *Biochemistry* **49,** 2984–2986 (2010).
48. Tuynman, A., Spelberg, J. L., Kooter, I. M., Schoemaker, H. E. & Wever, R. Enantioselective epoxidation and carbon-carbon bond cleavage catalyzed by Coprinus cinereus peroxidase and myeloperoxidase. *J. Biol. Chem.* **275,** 3025–3030 (2000).
49. Galzigna, L., Rizzoli, V., Schiappelli, M. P., Rigobello, M. P., Scarpa, M. & Rigo, A. Horseradish peroxidase-catalyzed sulfoxidation of promethazine and properties of promethazine sulfoxide. *Free Radic. Biol. Med.* **20,** 807–811 (1996).
50. Ozaki, S. & Ortiz de Montellano, P. R. Molecular Engineering of Horseradish Peroxidase: Thioether Sulfoxidation and Styrene Epoxidation by Phe-41 Leucine and Threonine Mutants. *J. Am. Chem. Soc.* **117,** 7056–7064 (1995).
51. Kumar, D., de Visser, S. P., Sharma, P. K., Derat, E. & Shaik, S. The intrinsic axial ligand effect on propene oxidation by horseradish peroxidase versus cytochrome P450 enzymes. *J. Biol. Inorg. Chem.* **10,** 181–189 (2005).
52. Millett, E. S., Efimov, I., Basran, J., Handa, S., Mowat, C. G. & Raven, E. L. Heme-containing dioxygenases involved in tryptophan oxidation. *Curr. Opin. Chem. Biol.* **16,** 60–66 (2012).
53. Hamilton, G. A. Mechanisms of Two- and Four-Electron Oxidations Catalyzed by Some Metalloenzymes. in *Advances in Enzymology and Related Areas of Molecular Biology* 55–96 (John Wiley & Sons Ltd, 2006).
54. Chauhan, N., Thackray, S. J., Rafice, S. A., Eaton, G., Lee, M., Efimov, I., Basran, J., Jenkins, P. R., Mowat, C. G., Chapman, S. K. & Raven, E. L. Reassessment of the Reaction Mechanism in the Heme Dioxygenases. *J. Am. Chem. Soc.* **131,** 4186–4187 (2009).
55. Nienhaus, K. & Nienhaus, G. U. Different Mechanisms of Catalytic Complex Formation in Two L-Tryptophan Processing Dioxygenases. *Front. Mol. Biosci.* **4,** 94 (2017).
56. Shin, I., Ambler, B. R., Wherritt, D., Griffith, W. P., Maldonado, A. C., Altman, R. A. & Liu, A. Stepwise O-Atom Transfer in Heme-Based Tryptophan Dioxygenase: Role of Substrate Ammonium in Epoxide Ring Opening. *J. Am. Chem. Soc.* **140,** 4372–4379 (2018).

57. Capece, L., Lewis-Ballester, A., Yeh, S.-R., Estrin, D. A. & Marti, M. A. Complete reaction mechanism of indoleamine 2,3-dioxygenase as revealed by QM/MM simulations. *J. Phys. Chem. B* **116,** 1401–1413 (2012).
58. Chung, L. W., Li, X., Sugimoto, H., Shiro, Y. & Morokuma, K. Density Functional Theory Study on a Missing Piece in Understanding of Heme Chemistry: The Reaction Mechanism for Indoleamine 2,3-Dioxygenase and Tryptophan 2,3-Dioxygenase. *J. Am. Chem. Soc.* **130,** 12299–12309 (2008).
59. Lewis-Ballester, A., Batabyal, D., Egawa, T., Lu, C., Lin, Y., Marti, M. A., Capece, L., Estrin, D. A. & Yeh, S.-R. Evidence for a ferryl intermediate in a heme-based dioxygenase. *Proc. Natl. Acad. Sci. U.S.A.* **106,** 17371–17376 (2009).
60. Lewis-Ballester, A., Forouhar, F., Kim, S.-M., Lew, S., Wang, Y., Karkashon, S., Seetharaman, J., Batabyal, D., Chiang, B.-Y., Hussain, M., Correia, M. A., Yeh, S.-R. & Tong, L. Molecular basis for catalysis and substrate-mediated cellular stabilization of human tryptophan 2,3-dioxygenase. *Sci. Rep.* **6,** 35169 (2016).
61. Makino, R., Obayashi, E., Hori, H., Iizuka, T., Mashima, K., Shiro, Y. & Ishimura, Y. Initial O_2 Insertion Step of the Tryptophan Dioxygenase Reaction Proposed by a Heme-Modification Study. *Biochemistry* **54,** 3604–3616 (2015).
62. Yanagisawa, S., Horitani, M., Sugimoto, H., Shiro, Y., Okada, N. & Ogura, T. Resonance Raman study on the oxygenated and the ferryl-oxo species of indoleamine 2,3-dioxygenase during catalytic turnover. *Faraday Discuss.* **148,** 239–247 (2010).
63. Basran, J., Booth, E. S., Lee, M., Handa, S. & Raven, E. L. Analysis of Reaction Intermediates in Tryptophan 2,3-Dioxygenase: A Comparison with Indoleamine 2,3-Dioxygenase. *Biochemistry* **55,** 6743–6750 (2016).
64. Lewis-Ballester, A., Karkashon, S., Batabyal, D., Poulos, T. L. & Yeh, S.-R. Inhibition Mechanisms of Human Indoleamine 2,3 Dioxygenase 1. *J. Am. Chem. Soc.* **140,** 8518–8525 (2018).
65. Chino, M., Leone, L., Zambrano, G., Pirro, F., D'Alonzo, D., Firpo, V., Aref, D., Lista, L., Maglio, O., Nastri, F. & Lombardi, A. Oxidation catalysis by iron and manganese porphyrins within enzyme-like cages. *Biopolymers* **109,** e23107 (2018).
66. Guo, M., Corona, T., Ray, K. & Nam, W. Heme and Nonheme High-Valent Iron and Manganese Oxo Cores in Biological and Abiological Oxidation Reactions. *ACS Cent. Sci.* **5,** 13–28 (2019).
67. Pereira, M. M., Dias, L. D. & Calvete, M. J. F. Metalloporphyrins: Bioinspired Oxidation Catalysts. *ACS Catal.* **8,** 10784–10808 (2018).
68. Dolphin, D., Traylor, T. G. & Xie, L. Y. Polyhaloporphyrins: Unusual Ligands for Metals and Metal-Catalyzed Oxidations. *Acc. Chem. Res.* **30,** 251–259 (1997).

69. Bell, S. R. & Groves, J. T. A Highly Reactive P450 Model Compound I. *J. Am. Chem. Soc.* **131,** 9640–9641 (2009).
70. Ehudin, M. A., Gee, L. B., Sabuncu, S., Braun, A., Moënne-Loccoz, P., Hedman, B., Hodgson, K. O., Solomon, E. I. & Karlin, K. D. Tuning the Geometric and Electronic Structure of Synthetic High-Valent Heme Iron(IV)-Oxo Models in the Presence of a Lewis Acid and Various Axial Ligands. *J. Am. Chem. Soc.* **141,** 5942–5960 (2019).
71. Hessenauer-Ilicheva, N., Franke, A., Meyer, D., Woggon, W.-D. & van Eldik, R. Low-Temperature Rapid-Scan Detection of Reactive Intermediates in Epoxidation Reactions Catalyzed by a New Enzyme Mimic of Cytochrome P450. *J. Am. Chem. Soc.* **129,** 12473–12479 (2007).
72. Hessenauer-Ilicheva, N., Franke, A., Wolak, M., Higuchi, T. & van Eldik, R. Spectroscopic and Mechanistic Studies on Oxidation Reactions Catalyzed by the Functional Model SR Complex for Cytochrome P450: Influence of Oxidant, Substrate, and Solvent. *Chem. Eur. J.* **15,** 12447–12459 (2009).
73. Nastri, F., Lombardi, A., D'Andrea, L. D., Sanseverino, M., Maglio, O. & Pavone, V. Miniaturized hemoproteins. *Biopolymers* **47,** 5–22 (1998).
74. Jin, N. & Groves, J. T. Unusual Kinetic Stability of a Ground-State Singlet Oxomanganese(V) Porphyrin. Evidence for a Spin State Crossing Effect. *J. Am. Chem. Soc.* **121,** 2923–2924 (1999).
75. Song, W. J., Seo, M. S., DeBeer George, S., Ohta, T., Song, R., Kang, M.-J., Tosha, T., Kitagawa, T., Solomon, E. I. & Nam, W. Synthesis, Characterization, and Reactivities of Manganese(V)−Oxo Porphyrin Complexes. *J. Am. Chem. Soc.* **129,** 1268–1277 (2007).
76. Guo, M., Dong, H., Li, J., Cheng, B., Huang, Y., Feng, Y. & Lei, A. Spectroscopic observation of iodosylarene metalloporphyrin adducts and manganese(V)-oxo porphyrin species in a cytochrome P450 analogue. *Nat. Commun.* **3,** 1–9 (2012).
77. Arunkumar, C., Lee, Y.-M., Lee, J. Y., Fukuzumi, S. & Nam, W. Hydrogen-atom abstraction reactions by manganese(V)- and manganese(IV)-oxo porphyrin complexes in aqueous solution. *Chem. Eur. J.* **15,** 11482–11489 (2009).
78. Neu, H. M., Yang, T., Baglia, R. A., Yosca, T. H., Green, M. T., Quesne, M. G., de Visser, S. P. & Goldberg, D. P. Oxygen-Atom Transfer Reactivity of Axially Ligated Mn(V)–Oxo Complexes: Evidence for Enhanced Electrophilic and Nucleophilic Pathways. *J. Am. Chem. Soc.* **136,** 13845–13852 (2014).
79. Guo, M., Seo, M. S., Lee, Y.-M., Fukuzumi, S. & Nam, W. Highly Reactive Manganese(IV)-Oxo Porphyrins Showing Temperature-Dependent Reversed Electronic Effect in C–H Bond Activation Reactions. *J. Am. Chem. Soc.* **141,** 12187–12191 (2019).

80. Srour, H., Maux, P. L. & Simonneaux, G. Enantioselective Manganese-Porphyrin-Catalyzed Epoxidation and C–H Hydroxylation with Hydrogen Peroxide in Water/Methanol Solutions. *Inorg. Chem.* **51,** 5850–5856 (2012).
81. Rosenthal, J. & Nocera, D. G. Oxygen Activation Chemistry of Pacman and Hangman Porphyrin Architectures Based on Xanthene and Dibenzofuran Spacers. in *Progress in Inorganic Chemistry* 483–544 (John Wiley & Sons Ltd, 2008).
82. Chang, C. J., Loh, Z.-H., Deng, Y. & Nocera, D. G. The Pacman Effect: A Supramolecular Strategy for Controlling the Excited-State Dynamics of Pillared Cofacial Bisporphyrins. *Inorg. Chem.* **42,** 8262–8269 (2003).
83. Liu, Y., Zhou, G., Zhang, Z., Lei, H., Yao, Z., Li, J., Lin, J. & Cao, R. Significantly improved electrocatalytic oxygen reduction by an asymmetrical Pacman dinuclear cobalt(II) porphyrin–porphyrin dyad. *Chem. Sci.* **11,** 87–96 (2019).
84. Naruta, Y., Sasayama, M. & Sasaki, T. Oxygen Evolution by Oxidation of Water with Manganese Porphyrin Dimers. *Angew. Chem. Int. Ed. Engl.* **33,** 1839–1841 (1994).
85. Jr, R. M., Dogutan, D. K., Teets, T. S., Suntivich, J., Shao-Horn, Y. & Nocera, D. G. Oxygen reduction reactivity of cobalt(II) hangman porphyrins. *Chem. Sci.* **1,** 411–414 (2010).
86. Margarit, C. G., Schnedermann, C., Asimow, N. G. & Nocera, D. G. Carbon Dioxide Reduction by Iron Hangman Porphyrins. *Organometallics* **38,** 1219–1223 (2019).
87. Kielb, P., Horch, M., Wrzolek, P., Goetz, R., H. Ly, K., Kozuch, J., Schwalbe, M. & M. Weidinger, I. Hydrogen evolution by cobalt hangman porphyrins under operating conditions studied by vibrational spectro-electrochemistry. *Catal. Sci. Technol.* **8,** 1849–1857 (2018).
88. Rosenthal, J., Chng, L. L., Fried, S. D. & Nocera, D. G. Stereochemical control of H2O2 dismutation by Hangman porphyrins. *Chem. Commun.* 2642–2644 (2007).
89. Chang, C. J., Chng, L. L. & Nocera, D. G. Proton-Coupled O−O Activation on a Redox Platform Bearing a Hydrogen-Bonding Scaffold. *J. Am. Chem. Soc.* **125,** 1866–1876 (2003).
90. Graham, D. J., Dogutan, D. K., Schwalbe, M. & Nocera, D. G. Hangman effect on hydrogen peroxide dismutation by Fe(III) corroles. *Chem. Commun.* **48,** 4175–4177 (2012).
91. Soper, J. D., Kryatov, S. V., Rybak-Akimova, E. V. & Nocera, D. G. Proton-Directed Redox Control of O−O Bond Activation by Heme Hydroperoxidase Models. *J. Am. Chem. Soc.* **129,** 5069–5075 (2007).
92. Marchi-Delapierre, C., Rondot, L., Cavazza, C. & Ménage, S. Oxidation Catalysis by Rationally Designed Artificial Metalloenzymes. *Isr. J. Chem.* **55,** 61–75 (2015).

93. Nastri, F., D'Alonzo, D., Leone, L., Zambrano, G., Pavone, V. & Lombardi, A. Engineering Metalloprotein Functions in Designed and Native Scaffolds. *Trends Biochem. Sci.* **44,** 1022–1040 (2019).
94. Mirts, E. N., Bhagi-Damodaran, A. & Lu, Y. Understanding and Modulating Metalloenzymes with Unnatural Amino Acids, Non-Native Metal Ions, and Non-Native Metallocofactors. *Acc. Chem. Res.* **52,** 935–944 (2019).
95. Oohora, K., Onoda, A. & Hayashi, T. Hemoproteins Reconstituted with Artificial Metal Complexes as Biohybrid Catalysts. *Acc. Chem. Res.* **52,** 945–954 (2019).
96. Schwizer, F., Okamoto, Y., Heinisch, T., Gu, Y., Pellizzoni, M. M., Lebrun, V., Reuter, R., Köhler, V., Lewis, J. C. & Ward, T. R. Artificial Metalloenzymes: Reaction Scope and Optimization Strategies. *Chem. Rev.* **118,** 142–231 (2018).
97. Mahy, J.-P., Maréchal, J.-D. & Ricoux, R. From "hemoabzymes" to "hemozymes": towards new biocatalysts for selective oxidations. *Chem. Commun.* **51,** 2476–2494 (2015).
98. Ricoux, R., Sauriat-Dorizon, H., Girgenti, E., Blanchard, D. & Mahy, J.-P. Hemoabzymes: towards new biocatalysts for selective oxidations. *J. Immunol. Methods* **269,** 39–57 (2002).
99. Ricoux, R., Lukowska, E., Pezzotti, F. & Mahy, J.-P. New activities of a catalytic antibody with a peroxidase activity: formation of Fe(II)-RNO complexes and stereoselective oxidation of sulfides. *Eur. J. Biochem.* **271,** 1277–1283 (2004).
100. Sansiaume-Dagousset, E., Ricoux, R., Gori, D. & Mahy, J.-P. Oxidation of organic molecules in homogeneous aqueous solution catalyzed by hybrid biocatalysts (based on the Trojan Horse strategy). *Tetrahedron: Asymmetry* **21,** 1593–1600 (2010).
101. Lewis, J. C. Beyond the Second Coordination Sphere: Engineering Dirhodium Artificial Metalloenzymes To Enable Protein Control of Transition Metal Catalysis. *Acc. Chem. Res.* **52,** 576–584 (2019).
102. Zhang, C., Srivastava, P., Ellis-Guardiola, K. & Lewis, J. C. Manganese terpyridine artificial metalloenzymes for benzylic oxygenation and olefin epoxidation. *Tetrahedron* **70,** 4245–4249 (2014).
103. Ward, T. R. Artificial metalloenzymes based on the biotin-avidin technology: enantioselective catalysis and beyond. *Acc. Chem. Res.* **44,** 47–57 (2011).
104. Heinisch, T. & Ward, T. R. Artificial Metalloenzymes Based on the Biotin-Streptavidin Technology: Challenges and Opportunities. *Acc. Chem. Res.* **49,** 1711–1721 (2016).
105. Liang, A. D., Serrano-Plana, J., Peterson, R. L. & Ward, T. R. Artificial Metalloenzymes Based on the Biotin-Streptavidin Technology: Enzymatic Cascades and Directed Evolution. *Acc. Chem. Res.* **52,** 585–595 (2019).

106. Zhao, J., Bachmann, D. G., Lenz, M., Gillingham, D. G. & Ward, T. R. An artificial metalloenzyme for carbene transfer based on a biotinylated dirhodium anchored within streptavidin. *Catal. Sci. Technol.* **8,** 2294–2298 (2018).
107. Dürrenberger, M., Heinisch, T., Wilson, Y. M., Rossel, T., Nogueira, E., Knörr, L., Mutschler, A., Kersten, K., Zimbron, M. J., Pierron, J., Schirmer, T. & Ward, T. R. Artificial Transfer Hydrogenases for the Enantioselective Reduction of Cyclic Imines. *Angewandte Chemie International Edition* **50,** 3026–3029 (2011).
108. Wu, S., Zhou, Y., Rebelein, J. G., Kuhn, M., Mallin, H., Zhao, J., Igareta, N. V. & Ward, T. R. Breaking Symmetry: Engineering Single-Chain Dimeric Streptavidin as Host for Artificial Metalloenzymes. *J. Am. Chem. Soc.* **141,** 15869–15878 (2019).
109. Drevelle, A., Graille, M., Heyd, B., Sorel, I., Ulryck, N., Pecorari, F., Desmadril, M., van Tilbeurgh, H. & Minard, P. Structures of in vitro evolved binding sites on neocarzinostatin scaffold reveal unanticipated evolutionary pathways. *J. Mol. Biol.* **358,** 455–471 (2006).
110. Sansiaume-Dagousset, E., Urvoas, A., Chelly, K., Ghattas, W., Maréchal, J.-D., Mahy, J.-P. & Ricoux, R. Neocarzinostatin-based hybrid biocatalysts for oxidation reactions. *Dalton Trans.* **43,** 8344–8354 (2014).
111. Ricoux, R., Dubuc, R., Dupont, C., Marechal, J.-D., Martin, A., Sellier, M. & Mahy, J.-P. Hemozymes Peroxidase Activity Of Artificial Hemoproteins Constructed From the Streptomyces lividans Xylanase A and Iron(III)-Carboxy-Substituted Porphyrins. *Bioconjugate Chem.* **19,** 899–910 (2008).
112. Allard, M., Dupont, C., Robles, V. M., Doucet, N., Lledós, A., Maréchal, J.-D., Urvoas, A., Mahy, J.-P. & Ricoux, R. Incorporation of Manganese Complexes into Xylanase: New Artificial Metalloenzymes for Enantioselective Epoxidation. *ChemBioChem* **13,** 240–251 (2012).
113. Ricoux, R., Allard, M., Dubuc, R., Dupont, C., Maréchal, J.-D. & Mahy, J.-P. Selective oxidation of aromatic sulfide catalyzed by an artificial metalloenzyme: new activity of hemozymes. *Org. Biomol. Chem.* **7,** 3208–3211 (2009).
114. Wang, X., Wang, C., Pan, M., Wei, J., Jiang, F., Lu, R., Liu, X., Huang, Y. & Huang, F. Chaperonin-Nanocaged Hemin as an Artificial Metalloenzyme for Oxidation Catalysis. *ACS Appl. Mater. Interfaces* **9,** 25387–25396 (2017).
115. Zhang, J.-L., Garner, D. K., Liang, L., Barrios, D. A. & Lu, Y. Non-covalent Modulation of pH Dependent Reactivity of a MnSalen Cofactor in Myoglobin with Hydrogen Peroxide. *Chem. Eur. J.* **15,** 7481–7489 (2009).
116. Ohashi, M., Koshiyama, T., Ueno, T., Yanase, M., Fujii, H. & Watanabe, Y. Preparation of Artificial Metalloenzymes by Insertion of Chromium(III)

Schiff Base Complexes into Apomyoglobin Mutants. *Angew. Chem. Int. Ed. Engl.* **42,** 1005–1008 (2003).
117. Sreenilayam, G., Moore, E. J., Steck, V. & Fasan, R. Metal Substitution Modulates the Reactivity and Extends the Reaction Scope of Myoglobin Carbene Transfer Catalysts. *Adv. Synth. Catal.* **359,** 2076–2089 (2017).
118. Natoli, S. N. & Hartwig, J. F. Noble-Metal Substitution in Hemoproteins: An Emerging Strategy for Abiological Catalysis. *Acc. Chem. Res.* **52,** 326–335 (2019).
119. Hayashi, T., Murata, D., Makino, M., Sugimoto, H., Matsuo, T., Sato, H., Shiro, Y. & Hisaeda, Y. Crystal Structure and Peroxidase Activity of Myoglobin Reconstituted with Iron Porphycene. *Inorg. Chem.* **45,** 10530–10536 (2006).
120. Oohora, K., Kihira, Y., Mizohata, E., Inoue, T. & Hayashi, T. C(sp3)-H bond hydroxylation catalyzed by myoglobin reconstituted with manganese porphycene. *J. Am. Chem. Soc.* **135,** 17282–17285 (2013).
121. Oohora, K., Meichin, H., Kihira, Y., Sugimoto, H., Shiro, Y. & Hayashi, T. Manganese(V) Porphycene Complex Responsible for Inert C-H Bond Hydroxylation in a Myoglobin Matrix. *J. Am. Chem. Soc.* **139,** 18460–18463 (2017).
122. Key, H. M., Dydio, P., Clark, D. S. & Hartwig, J. F. Abiological catalysis by artificial haem proteins containing noble metals in place of iron. *Nature* **534,** 534–537 (2016).
123. Lin, Y.-W., Yeung, N., Gao, Y.-G., Miner, K. D., Lei, L., Robinson, H. & Lu, Y. Introducing a 2-His-1-Glu Nonheme Iron Center into Myoglobin Confers Nitric Oxide Reductase Activity. *J. Am. Chem. Soc.* **132,** 9970–9972 (2010).
124. Yeung, N., Lin, Y.-W., Gao, Y.-G., Zhao, X., Russell, B. S., Lei, L., Miner, K. D., Robinson, H. & Lu, Y. Rational Design of a Structural and Functional Nitric Oxide Reductase. *Nature* **462,** 1079–1082 (2009).
125. Lin, Y.-W., Yeung, N., Gao, Y.-G., Miner, K. D., Tian, S., Robinson, H. & Lu, Y. Roles of glutamates and metal ions in a rationally designed nitric oxide reductase based on myoglobin. *Proc. Natl. Acad. Sci. U.S.A.* **107,** 8581–8586 (2010).
126. Buschmann, S., Warkentin, E., Xie, H., Langer, J. D., Ermler, U. & Michel, H. The structure of cbb3 cytochrome oxidase provides insights into proton pumping. *Science* **329,** 327–330 (2010).
127. Miner, K. D., Mukherjee, A., Gao, Y.-G., Null, E. L., Petrik, I. D., Zhao, X., Yeung, N., Robinson, H. & Lu, Y. A Designed Functional Metalloenzyme that Reduces O2 to H2O with Over One Thousand Turnovers. *Angew. Chem. Int. Ed. Engl.* **51,** 5589–5592 (2012).
128. Yu, Y., Mukherjee, A., Nilges, M. J., Hosseinzadeh, P., Miner, K. D. & Lu, Y. Direct EPR Observation of a Tyrosyl Radical in a Functional Oxidase

Model in Myoglobin during both H2O2 and O2 Reactions. *J. Am. Chem. Soc.* **136,** 1174–1177 (2014).

129. Bhagi-Damodaran, A., Petrik, I. D., Marshall, N. M., Robinson, H. & Lu, Y. Systematic Tuning of Heme Redox Potentials and Its Effects on O2 Reduction Rates in a Designed Oxidase in Myoglobin. *J. Am. Chem. Soc.* **136,** 11882–11885 (2014).
130. Bhagi-Damodaran, A., Kahle, M., Shi, Y., Zhang, Y., Ädelroth, P. & Lu, Y. Insights Into How Heme Reduction Potentials Modulate Enzymatic Activities of a Myoglobin-based Functional Oxidase. *Angew. Chem. Int. Ed. Engl.* **56,** 6622–6626 (2017).
131. Mukherjee, S., Mukherjee, M., Mukherjee, A., Bhagi-Damodaran, A., Lu, Y. & Dey, A. O2 Reduction by Biosynthetic Models of Cytochrome c Oxidase: Insights into Role of Proton Transfer Residues from Perturbed Active Sites Models of CcO. *ACS Catal.* **8,** 8915–8924 (2018).
132. Lombardi, A., Pirro, F., Maglio, O., Chino, M. & DeGrado, W. F. De Novo Design of Four-Helix Bundle Metalloproteins: One Scaffold, Diverse Reactivities. *Acc. Chem. Res.* **52,** 1148–1159 (2019).
133. Chino, M., Maglio, O., Nastri, F., Pavone, V., DeGrado, W. F. & Lombardi, A. Artificial Diiron Enzymes with a De Novo Designed Four-Helix Bundle Structure. *Eur. J. Inorg. Chem.* **2015,** 3371–3390 (2015).
134. Rhys, G. G., Wood, C. W., Beesley, J. L., Zaccai, N. R., Burton, A. J., Brady, R. L., Thomson, A. R. & Woolfson, D. N. Navigating the Structural Landscape of De Novo α-Helical Bundles. *J. Am. Chem. Soc.* **141,** 8787–8797 (2019).
135. Roy, A., Sarrou, I., Vaughn, M. D., Astashkin, A. V. & Ghirlanda, G. De Novo Design of an Artificial Bis[4Fe-4S] Binding Protein. *Biochemistry* **52,** 7586–7594 (2013).
136. Roy, A., Sommer, D. J., Schmitz, R. A., Brown, C. L., Gust, D., Astashkin, A. & Ghirlanda, G. A De Novo Designed 2[4Fe-4S] Ferredoxin Mimic Mediates Electron Transfer. *J. Am. Chem. Soc.* **136,** 17343–17349 (2014).
137. Zastrow, M. L. & Pecoraro, V. L. Designing Hydrolytic Zinc Metalloenzymes. *Biochemistry* **53,** 957–978 (2014).
138. Cangelosi, V. M., Deb, A., Penner-Hahn, J. E. & Pecoraro, V. L. A De Novo Designed Metalloenzyme for the Hydration of CO2. *Angew. Chem. Int. Ed. Engl.* **53,** 7900–7903 (2014).
139. Shiga, D., Funahashi, Y., Masuda, H., Kikuchi, A., Noda, M., Uchiyama, S., Fukui, K., Kanaori, K., Tajima, K., Takano, Y., Nakamura, H., Kamei, M. & Tanaka, T. Creation of a Binuclear Purple Copper Site within a de Novo Coiled-Coil Protein. *Biochemistry* **51,** 7901–7907 (2012).

140. Koebke, K. J. & Pecoraro, V. L. Development of de Novo Copper Nitrite Reductases: Where We Are and Where We Need To Go. *ACS Catal.* **8,** 8046–8057 (2018).
141. Chino, M., Leone, L., Maglio, O., D'Alonzo, D., Pirro, F., Pavone, V., Nastri, F. & Lombardi, A. A De Novo Heterodimeric Due Ferri Protein Minimizes the Release of Reactive Intermediates in Dioxygen-Dependent Oxidation. *Angew. Chem. Int. Ed. Engl.* **56,** 15580–15583 (2017).
142. Reig, A. J., Pires, M. M., Snyder, R. A., Wu, Y., Jo, H., Kulp, D. W., Butch, S. E., Calhoun, J. R., Szyperski, T., Solomon, E. I. & DeGrado, W. F. Alteration of the oxygen-dependent reactivity of de novo Due Ferri proteins. *Nat. Chem.* **4,** 900–906 (2012).
143. Choma, C. T., Lear, J. D., Nelson, M. J., Dutton, P. L., Robertson, D. E. & DeGrado, W. F. Design of a heme-binding four-helix bundle. *J. Am. Chem. Soc.* **116,** 856–865 (1994).
144. Shifman, J. M., Moser, C. C., Kalsbeck, W. A., Bocian, D. F. & Dutton, P. L. Functionalized de Novo Designed Proteins: Mechanism of Proton Coupling to Oxidation/Reduction in Heme-protein Maquettes. *Biochemistry* **37,** 16815–16827 (1998).
145. Gibney, B. R., Isogai, Y., Rabanal, F., Reddy, K. S., Grosset, A. M., Moser, C. C. & Dutton, P. L. Self-assembly of heme A and heme B in a designed four-helix bundle: implications for a cytochrome c oxidase maquette. *Biochemistry* **39,** 11041–11049 (2000).
146. Discher, B. M., Noy, D., Strzalka, J., Ye, S., Moser, C. C., Lear, J. D., Blasie, J. K. & Dutton, P. L. Design of Amphiphilic Protein Maquettes: Controlling Assembly, Membrane Insertion, and Cofactor Interactions. *Biochemistry* **44,** 12329–12343 (2005).
147. Noy, D., Discher, B. M., Rubtsov, I. V., Hochstrasser, R. M. & Dutton, P. L. Design of Amphiphilic Protein Maquettes: Enhancing Maquette Functionality through Binding of Extremely Hydrophobic Cofactors to Lipophilic Domains. *Biochemistry* **44,** 12344–12354 (2005).
148. Kodali, G., Mancini, J. A., Solomon, L. A., Episova, T. V., Roach, N., Hobbs, C. J., Wagner, P., Mass, O. A., Aravindu, K., Barnsley, J. E., Gordon, K. C., Officer, D. L., Dutton, P. L. & Moser, C. C. Design and engineering of water-soluble light-harvesting protein maquettes. *Chem. Sci.* **8,** 316–324 (2016).
149. Fry, B. A., Solomon, L. A., Leslie Dutton, P. & Moser, C. C. Design and engineering of a man-made diffusive electron-transport protein. *Biochim. Biophys. Acta* **1857,** 513–521 (2016).
150. Fry, B. A., Goparaju, G., Moser, C. M., Dutton, P. L. & Discher, B. M. Interprotein Electron Transfer with Protein Maquettes. *Biophys. J.* **106,** 589a (2014).

151. Koder, R. L., Anderson, J. L. R., Solomon, L. A., Reddy, K. S., Moser, C. C. & Dutton, P. L. Design and engineering of an O2 transport protein. *Nature* **458,** 305–309 (2009).
152. D'Souza, A., Wu, X., Yeow, E. K. L. & Bhattacharjya, S. Designed Heme-Cage β-Sheet Miniproteins. *Angew. Chem. Int. Ed. Engl.* **56,** 5904–5908 (2017).
153. D'Souza, A., Mahajan, M. & Bhattacharjya, S. Designed multi-stranded heme binding β-sheet peptides in membrane. *Chem. Sci.* **7,** 2563–2571 (2016).
154. Solomon, L. A., Kronenberg, J. B. & Fry, H. C. Control of Heme Coordination and Catalytic Activity by Conformational Changes in Peptide–Amphiphile Assemblies. *J. Am. Chem. Soc.* **139,** 8497–8507 (2017).
155. Asayama, S., Kawamura, E., Nagaoka, S. & Kawakami, H. Design of Manganese Porphyrin Modified with Mitochondrial Signal Peptide for a New Antioxidant. *Mol. Pharm.* **3,** 468–470 (2006).
156. Umezawa, N., Matsumoto, N., Iwama, S., Kato, N. & Higuchi, T. Facile synthesis of peptide–porphyrin conjugates: Towards artificial catalase. *Bioorg. Med. Chem.* **18,** 6340–6350 (2010).
157. Kleingardner, E. C., Asher, W. B. & Bren, K. L. Efficient and Flexible Preparation of Biosynthetic Microperoxidases. *Biochemistry* **56,** 143–148 (2017).
158. Osman, A. M., Koerts, J., Boersma, M. G., Boeren, S., Veeger, C. & Rietjens, I. M. C. M. Microperoxidase/H2O2-Catalyzed Aromatic Hydroxylation Proceeds by a Cytochrome-P-450-Type Oxygen-Transfer Reaction Mechanism. *Eur. J. Biochem.* **240,** 232–238 (1996).
159. Boersma, M. G., Primus, J.-L., Koerts, J., Veeger, C. & Rietjens, I. M. C. M. Heme-(hydro)peroxide mediated O- and N-dealkylation. *Eur. J. Biochem.* **267,** 6673–6678 (2000).
160. Kadnikova, E. N. & Kostić, N. M. Effects of the Environment on Microperoxidase-11 and on Its Catalytic Activity in Oxidation of Organic Sulfides to Sulfoxides. *J. Org. Chem.* **68,** 2600–2608 (2003).
161. Ichinose, H., Wariishi, H. & Tanaka, H. Effective oxygen transfer reaction catalyzed by microperoxidase-11 during sulfur oxidation of dibenzothiophene. *Enzyme Microbial Technol.* **30,** 334–339 (2002).
162. Dallacosta, C., Monzani, E. & Casella, L. Reactivity study on microperoxidase-8. *J. Biol. Inorg. Chem.* **8,** 770–776 (2003).
163. Dallacosta, C., Casella, L. & Monzani, E. Modified Microperoxidases Exhibit Different Reactivity Towards Phenolic Substrates. *ChemBioChem* **5,** 1692–1699 (2004).
164. Primus, J. L., Boersma, M. G., Mandon, D., Boeren, S., Veeger, C., Weiss, R. & Rietjens, I. M. The effect of iron to manganese substitution on

microperoxidase 8 catalysed peroxidase and cytochrome P450 type of catalysis. *J. Biol. Inorg. Chem.* **4,** 274–283 (1999).
165. Yeh, H.-C., Yu, C.-H., Wang, J.-S., Chen, S.-T., Su, O. Y. & Lin, W.-Y. Stopped-flow kinetic study of the peroxidase reactions of mangano-microperoxidase-8. *J. Biol. Inorg. Chem.* **7,** 113–119 (2001).
166. Munro, O. Q. & Marques, H. M. Heme−Peptide Models for Hemoproteins. 1. Solution Chemistry of N-Acetylmicroperoxidase-8. *Inorg. Chem.* **35,** 3752–3767 (1996).
167. Verbaro, D., Hagarman, A., Kohli, A. & Schweitzer-Stenner, R. Microperoxidase 11: a model system for porphyrin networks and heme-protein interactions. *J. Biol. Inorg. Chem.* **14,** 1289–1300 (2009).
168. Yarman, A., Badalyan, A., Gajovic-Eichelmann, N., Wollenberger, U. & Scheller, F. W. Enzyme electrode for aromatic compounds exploiting the catalytic activities of microperoxidase-11. *Biosensors Bioelectron.* **30,** 320–323 (2011).
169. Gkaniatsou, E., Sicard, C., Ricoux, R., Benahmed, L., Bourdreux, F., Zhang, Q., Serre, C., Mahy, J.-P. & Steunou, N. Enzyme Encapsulation in Mesoporous Metal-Organic Frameworks for Selective Biodegradation of Harmful Dye Molecules. *Angew. Chem. Int. Ed. Engl.* **57,** 16141–16146 (2018).
170. Solomon, L. A., Kodali, G., Moser, C. C. & Dutton, P. L. Engineering the Assembly of Heme Cofactors in Man-Made Proteins. *J. Am. Chem. Soc.* **136,** 3192–3199 (2014).
171. Ghirlanda, G., Osyczka, A., Liu, W., Antolovich, M., Smith, K. M., Dutton, P. L., Wand, A. J. & DeGrado, W. F. De novo design of a D2-symmetrical protein that reproduces the diheme four-helix bundle in cytochrome bc1. *J. Am. Chem. Soc.* **126,** 8141–8147 (2004).
172. Faiella, M., Maglio, O., Nastri, F., Lombardi, A., Lista, L., Hagen, W. R. & Pavone, V. De Novo Design, Synthesis and Characterisation of MP3, A New Catalytic Four-Helix Bundle Hemeprotein. *Chem. Eur. J.* **18,** 15960–15971 (2012).
173. Watkins, D. W., Jenkins, J. M. X., Grayson, K. J., Wood, N., Steventon, J. W., Le Vay, K. K., Goodwin, M. I., Mullen, A. S., Bailey, H. J., Crump, M. P., MacMillan, F., Mulholland, A. J., Cameron, G., Sessions, R. B., Mann, S. & Anderson, J. L. R. Construction and in vivo assembly of a catalytically proficient and hyperthermostable de novo enzyme. *Nat. Commun.* **8,** 1–9 (2017).
174. Anderson, J. L. R., Armstrong, C. T., Kodali, G., Lichtenstein, B. R., Watkins, D. W., Mancini, J. A., Boyle, A. L., Farid, T. A., Crump, M. P., Moser, C. C. & Dutton, P. L. Constructing a man-made c-type cytochrome maquette in vivo: electron transfer, oxygen transport and conversion to a photoactive light harvesting maquette. *Chem. Sci.* **5,** 507–514 (2013).

175. Stenner, R., Steventon, J. W., Seddon, A. & Anderson, J. L. R. A de novo peroxidase is also a promiscuous yet stereoselective carbene transferase. *Proc. Natl. Acad. Sci. U.S.A.* **117,** 1419–1428 (2020).
176. Nastri, F., Lombardi, A., Morelli, G., Maglio, O., D'Auria, G., Pedone, C. & Pavone, V. Hemoprotein Models Based on a Covalent Helix–Heme–Helix Sandwich: 1. Design, Synthesis, and Characterization. *Chem. Eur. J.* **3,** 340–349 (1997).
177. D'Auria, G., Maglio, O., Nastri, F., Lombardi, A., Mazzeo, M., Morelli, G., Paolillo, L., Pedone, C. & Pavone, V. Hemoprotein Models Based on a Covalent Helix–Heme–Helix Sandwich: 2. Structural Characterization of CoIII Mimochrome I δ and λ Isomers. *Chem. Eur. J.* **3,** 350–362 (1997).
178. Lombardi, A., Nastri, F., Sanseverino, M., Maglio, O., Pedone, C. & Pavone, V. Miniaturized hemoproteins: design, synthesis and characterization of mimochrome II. *Inorg. Chim. Acta* **275–276,** 301–313 (1998).
179. Lombardi, A., Nastri, F., Marasco, D., Maglio, O., Sanctis, G. D., Sinibaldi, F., Santucci, R., Coletta, M. & Pavone, V. Design of a New Mimochrome with Unique Topology. *Chem. Eur. J.* **9,** 5643–5654 (2003).
180. Di Costanzo, L., Geremia, S., Randaccio, L., Nastri, F., Maglio, O., Lombardi, A. & Pavone, V. Miniaturized heme-proteins: crystal structure of Co(III)-mimochrome IV. *J. Biol. Inorg. Chem.* **9,** 1017–1027 (2004).
181. Nastri, F., Lista, L., Ringhieri, P., Vitale, R., Faiella, M., Andreozzi, C., Travascio, P., Maglio, O., Lombardi, A. & Pavone, V. A Heme–Peptide Metalloenzyme Mimetic with Natural Peroxidase-Like Activity. *Chem. Eur. J.* **17,** 4444–4453 (2011).
182. Vitale, R., Lista, L., Lau-Truong, S., Tucker, R. T., Brett, M. J., Limoges, B., Pavone, V., Lombardi, A. & Balland, V. Spectroelectrochemistry of FeIII- and CoIII-mimochrome VI artificial enzymes immobilized on mesoporous ITO electrodes. *Chem. Commun.* **50,** 1894–1896 (2014).
183. Vitale, R., Lista, L., Cerrone, C., Caserta, G., Chino, M., Maglio, O., Nastri, F., Pavone, V. & Lombardi, A. An artificial heme-enzyme with enhanced catalytic activity: evolution, functional screening and structural characterization. *Org. Biomol. Chem.* **13,** 4859–4868 (2015).
184. Blasio, B. D., Pavone, V., Lombardi, A., Pedone, C. & Benedetti, E. Noncoded residues as building blocks in the design of specific secondary structures: Symmetrically disubstituted glycines and β-alanine. *Biopolymers* **33,** 1037–1049 (1993).
185. Karle, I. L. Controls exerted by the Aib residue: Helix formation and helix reversal. *Peptide Science* **60,** 351–365 (2001).
186. Banerjee, R. & Basu, G. A Short Aib/Ala-Based Peptide Helix Is as Stable as an Ala-Based Peptide Helix Double Its Length. *ChemBioChem* **3,** 1263–1266 (2002).

187. Caserta, G., Chino, M., Firpo, V., Zambrano, G., Leone, L., D'Alonzo, D., Nastri, F., Maglio, O., Pavone, V. & Lombardi, A. Enhancement of Peroxidase Activity in Artificial Mimochrome VI Catalysts through Rational Design. *ChemBioChem* **19,** 1823–1826 (2018).
188. Firpo, V., Le, J. M., Pavone, V., Lombardi, A. & Bren, K. L. Hydrogen evolution from water catalyzed by cobalt-mimochrome VI*a, a synthetic mini-protein. *Chem. Sci.* **9,** 8582–8589 (2018).

SECTION 2:
Results and discussion

This page was intentionally left blank.

1. MN-MC6*A PREPARATION AND ANALYSIS

apo-MC6*a was obtained by combining solid-phase and solution methods as previously reported.[1] A schematic representation of MC6*a structure and sequence is shown in Scheme 1.1.

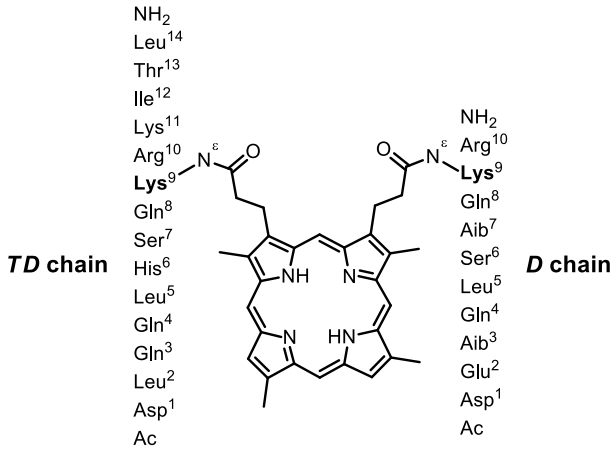

Scheme 1.1. Representation of MC6*a with the sequences of the peptide chains.

Briefly, the synthetic procedure involves the following steps:

- solid–phase synthesis of the peptide chains;
- solution–phase conjugation of the protected peptides to the porphyrin;
- side chain deprotection.

The two peptide chains were synthesized on a medium 20 mmol scale using the 9–fluorenylmethoxycarbonyl (Fmoc) chemistry approach. A super acid labile resin was used in order to obtain protected peptides after cleavage from the solid support. In both peptides, a 4-methyltrityl (Mtt) protecting group was used for Lys^9 side chain, which enables the selective deprotection of this residue during the cleavage from the resin. With this strategy, it is possible to avoid the interference of other residues sidechains and selectively couple deuteroporphyrin IX (DPIX) to Lys^9 of both peptides, following Scheme 1.2.

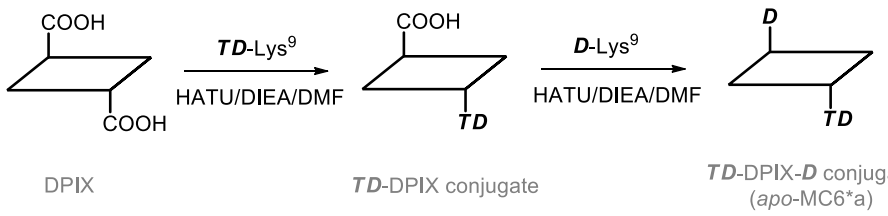

Scheme 1.2. Schematic representation of the MC6*a synthetic strategy. DPIX is depicted as a hollow rectangle.

Manganese ion insertion into *apo*-MC6*a was carried out by using a variation of the classical acetate method,[2] involving $Mn(OAc)_2$ (10 eq) in a mixture of hot (50°C) glacial acetic acid and trifluoroethanol. Reaction progress was followed by analytical RP-HPLC and product identity was assessed by ESI-MS analysis (Experimental mass: (3489.2 ± 0.4) Da; Theoretical mass: 3488.8 Da; see Materials and Methods for a detailed description). Product formation was further confirmed by UV-Vis absorption spectroscopy. In aqueous acidic solution, the Soret band, which is at 401 nm for the *apo*-form (Figure 1.1A), appears to be splitted into two components at 365 and 459 nm for Mn-MC6*a (Figure 1.1B). In the visible region, Mn-MC6*a exhibited two Q bands at 542 (β) and 571 nm (α), while in the spectrum of the *apo*-form four Q bands were present.

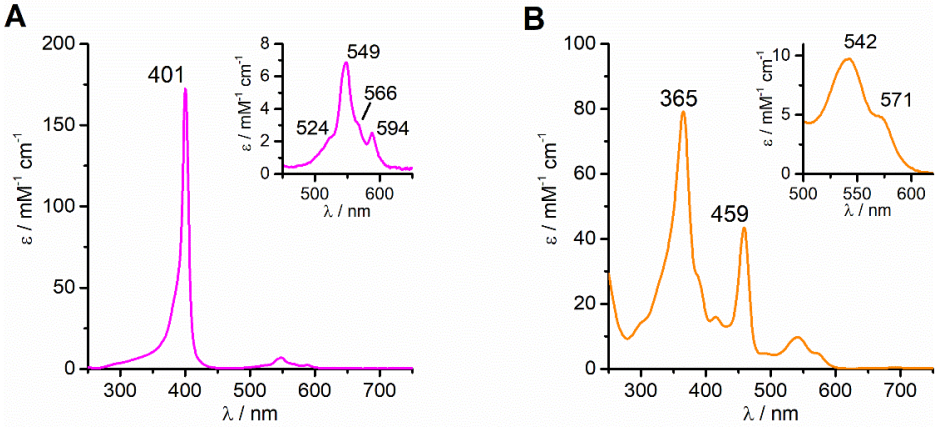

Figure 1.1. UV-Vis spectra of *apo*-MC6*a (A) and Mn-MC6*a (B) at 10 µM concentration in H_2O, 0.1% trifluoroacetic acid.

These spectral features are in good agreement with those reported for high-spin Mn^{III}-porphyrin complexes.[3]

Stock solutions of Mn-MC6*a in H_2O 0.1% trifluoroacetic acid (TFA) were analysed for the metal content by atomic absorption spectroscopy (AAS). Proper dilution of the stock solutions allowed for the determination of the molar extinction coefficient, which was found to be $\varepsilon_{365} = (7.84 \pm 0.02) \cdot 10^4\ M^{-1}\ cm^{-1}$.

2. SPECTROSCOPIC CHARACTERIZATION

UV-vis and circular dichroism (CD) spectroscopies were combined to gain information on the structural and coordination properties of Mn-MC6*a. All data were compared with those already reported for Fe-MC6*a.[1,4]

UV-Vis spectro-electrochemical (SEC) analysis was performed with both Fe- and Mn-MC6*a to get further insight into the metal coordination states at different pHs while analysing the redox properties of the two complexes.

2.1. Structural properties of Mn-MC6*a by CD spectroscopy

Structural properties of Mn-MC6*a in aqueous solution were analysed by CD spectroscopy. In particular, the effect of the helix-stabilizing 2,2,2-trifluoroethanol (TFE) was investigated.[5,6] Far-UV CD spectra were acquired in 5 mM phosphate buffer solution at pH 6.5 with different TFE concentrations (in the range of 0-50% *v/v*; Figure 2.1).

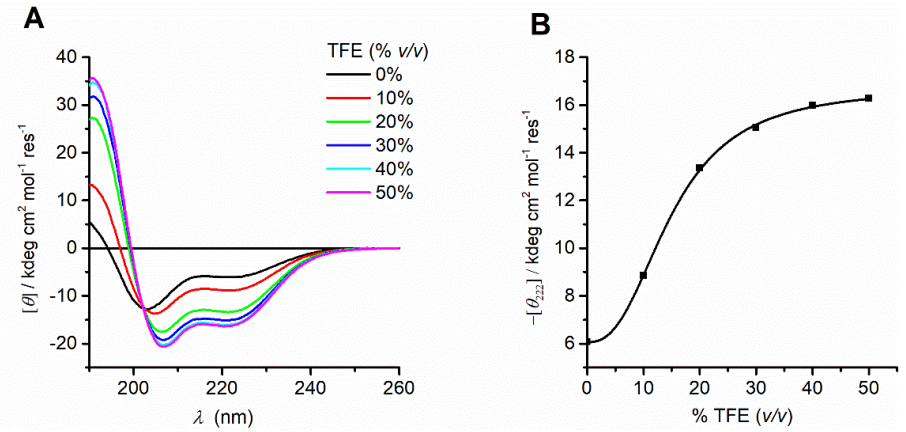

Figure 2.1. (A) Far-UV CD spectra of Mn-MC6*a ($2.0 \cdot 10^{-5}$ M) acquired in 5mM phosphate buffered solution (pH 6.5) at different TFE concentrations (% *v/v*); (B) titration curve showing $-[\theta_{222}]$ as a function of TFE concentration (% *v/v*).

While in the absence of TFE the peptide chains appear as poorly structured, but reminiscent of an α-helix secondary structure[7] (Figure 2.2A), addition of TFE increasingly contributes to enhance the α-helical content, as assessed by:

i) the increase of the mean residue ellipticity at 222 nm (θ_{222}) (Figure 2.2B and Table 2.1, line 2);

ii) the shift of the lower minimum (λ_{min}) towards 207 nm (Table 2.1, line 3);

iii) the enhancement of the θ_{ratio} ($\theta_{222}/\theta_{min}$), progressively approaching the unity (Table 2.1, line 4);

iv) the λ_0 shift to higher wavelengths (Table 2.1, line 5).

Similarly to Fe-MC6*a,[1] the maximum α-helical content was reached at 40% TFE (*v/v*).

Table 2.1: Far UV CD parameters of Mn-MC6*a in phosphate buffer/TFE solution (pH 6.5).

% TFE (*v/v*)	$[\theta_{222}]^{[a]}$	$[\theta_{min}]^{[a,b]}$ (λ, nm)	$\theta_{ratio}^{[c]}$	$\lambda_0^{[d]}$ (nm)
0	-6072	-12742 (202.6)	0.47	194.0
10	-8849	-13732 (204.8)	0.64	197.0
20	-13350	-17523 (206.2)	0.76	198.8
30	-15042	-19228 (206.6)	0.78	199.2
40	-15986	-20263 (206.8)	0.79	199.4
50	-16266	-20648 (207.0)	0.79	199.4

[a] [θ] is expressed as mean residue ellipticity (deg cm^2 $dmol^{-1}$ res^{-1}); [b]: [θ_{min}] represents the [θ] value at the shorter wavelength minimum (reported in parentheses); [c]: θ_{ratio} is the ratio [θ_{222}]/[θ_{min}]; [d]: λ_0 represents the crossover wavelength.

The induced Cotton effects in the Soret region were also examined to investigate the role of TFE on the stabilization of the global structure of the molecule (Figure 2.2). When acquiring CD spectra of Mn-MC6*a in the Soret region at 0 and 40% TFE, two negative Cotton effects at 357 nm and 463 nm were observed in both cases. In the absence of TFE, the most intense band at 357 nm appears very broad,

while it becomes better resolved at 40% TFE (Figure 2.2). Moreover, the intensity of the Cotton effects for all bands increases upon TFE addition.

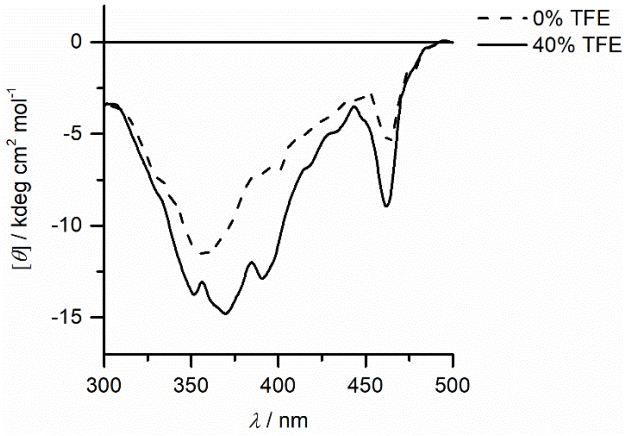

Figure 2.2. CD spectra of Mn-MC6*a ($2.0 \cdot 10^{-5}$ M) in the Soret region acquired in 5 mM phosphate buffer in the absence (dashed line) and in the presence (plain line) of 40% *v/v* TFE.

The overall CD data indicate that both secondary and tertiary structures experience a TFE-dependent stabilization. Accordingly, further spectroscopic and catalytic investigations were performed in aqueous solutions containing 40% (*v/v*) TFE.

2.2. Coordination properties of Mn-MC6*a by UV-Vis pH titration

The coordination properties of Mn-MC6*a were investigated by a UV-vis pH titration, following the changes in the absorption spectrum over a wide pH range (2.0-12.0). The molar extinction coefficient at 365 nm (ε^{365}) was plotted as a function of $[H_3O^+]$ and the experimental data points were fitted to the following equation (2.1) describing pH-dependent equilibria involving four species (see Section 3, Materials and Methods, for details).

$$A_{tot} = \frac{\left(A_D + A_C \cdot \frac{[H^+]}{K_{a3}} + A_B \cdot \frac{[H^+]^2}{K_{a3} \cdot K_{a2}} + A_A \cdot \frac{[H^+]^3}{K_{a3} \cdot K_{a2} \cdot K_{a1}}\right)}{\left(1 + \frac{[H^+]}{K_{a3}} + \frac{[H^+]^2}{K_{a3} \cdot K_{a2}} + \frac{[H^+]^3}{K_{a3} \cdot K_{a2} \cdot K_{a1}}\right)} \quad (2.1)$$

A_A, A_B, A_C, A_D, parameters are the absorbance of the four differently protonated species, which will be referred as species **1-4** in the following.

The best fit gave three transitions with midpoints at pH 4.0 (pK_{a1}), 7.2 (pK_{a2}) and 9.8 (pK_{a3}) (Figure 2.3A). At pH 2, the *bis*-aquo species was predominant (species **1,** Figure 2.3C and 2.3D), characterized by two absorption bands at 365 and 458 nm in the Soret region (see Table 2.2 and Figure 2.3B).[3] A significant decrease in the absorbance, along with slight wavelength shifts of both bands, occurs as pH increases from 2.0 to 5.4. The component at 365 nm is blue-shifted while the other one is red-shifted. These spectral changes are reasonably attributed to the deprotonation of the His^6 side chain ($pK_{a1} = 4.0$), to give a His-aquo coordination (species **2**).[8] A further pH increase from 5.4 to 8.4 only causes a small increase of the Soret extinction coefficients. These spectroscopic features suggest the presence of a deprotonation equilibrium involving a second shell residue ($pK_{a2} = 7.2$), which does not perturb the first coordination environment and gives rise to species **3**. Upon pH increase from 8.4 to 12.0, substantial spectral changes occur both in intensity and position of the Soret band. They may account for the deprotonation of the metal-bound water ligand ($pK_{a3} = 9.8$), leading to the alkaline form of Mn-MC6*a, with the His-hydroxy axial coordination (species **4**).

Table 2.2: UV-vis absorption maxima of Mn-MC6*a in H_2O/TFE solution (60/40 *v/v*) at different pH values.

pH	Species	Soret bands λ (nm)	Soret ε[a] (mM^{-1} cm^{-1})	Q bands (β,α) λ (nm)
2.0	1	365, 458	79	542, 573
5.6	2	362, 462	64	547, 575 (sh)
8.3	3	362, 462	68	547, 575 (sh)
10.8	4	348, 460	65	552, 590 (sh)

[a] Soret ε refers to the band with a lower wavelength.

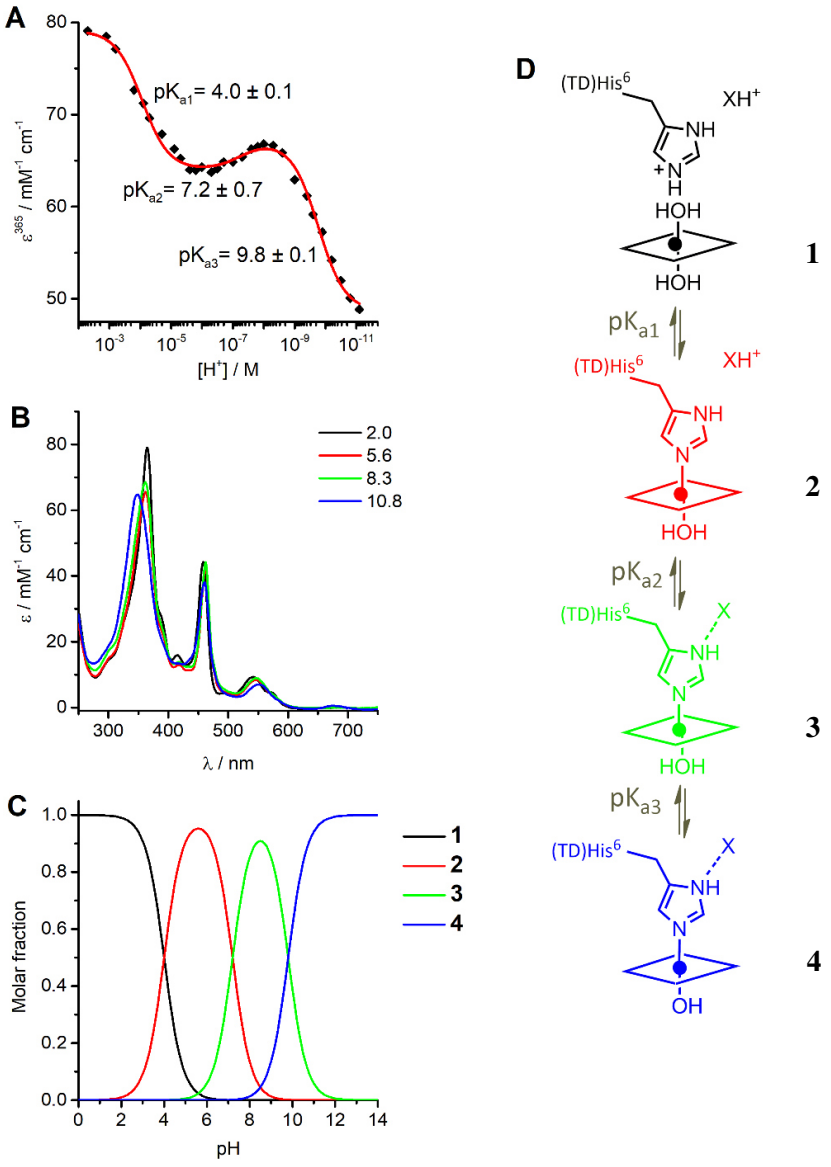

Figure 2.3. Plot of the ε^{365} (Soret) variation as a function of $[H^+]$ obtained from the UV-vis pH titration of Mn-MC6*a (15 μM) in aqueous solution containing 40% TFE (*v/v*), T=25°C. Data points were fitted as described in the experimental Section. (B) Absorption spectra of the four species involved in the acid-base equilibria. Curves of different colours represent the different pH values, as indicated in the legend. (C) pH-dependent speciation diagram obtained from the titration data. (D) Schematic representation of the acid-base equilibria.

2.3. Spectro-electrochemical (SEC) analysis of Fe- and Mn-MC6*a

UV-Vis SEC titrations were performed to completely characterise the redox and spectroscopic properties of the Fe^{II}/Fe^{III} and Mn^{II}/Mn^{III} couples of MC6*a metal complexes. Compared to classical electrochemical methods (e.g. cyclic voltammetry), the spectro-electrochemical technique holds the advantage to be independent from capacitive currents, which usually affect the accuracy of electrochemical data.[9,10] Furthermore, SEC offers the possibility to elucidate cross-correlations between the spectroscopic and redox properties of the redox-active species.[11,12] This part of the study was aimed at underlining the role of different coordination states on the relative stability of the oxidized and reduced forms. To this end, SEC titrations were performed in different pH conditions. The spectro-electrochemical characterization of Fe- and Mn-MC6*a was conducted in collaboration with Dr. Ross Anderson and Prof. Emma Raven at the University of Bristol.

The experimental apparatus consisted of a thin layer quartz cell (0.3 mm pathlength) set up for UV−Vis and electrochemical measurements (Figure 2.4). A Pt gauze working electrode (WE) was inserted into the thin layer cell containing a small volume of catalyst solution (120 μL) in buffer with 10% glycerol. Redox mediators were also added to facilitate equilibration between the electrode and the metal centre. A larger volume of buffer containing no glycerol, mediators or catalyst was added to the upper part of the cell, in which counter (Pt) and reference (Ag/AgCl) electrodes were placed. Mixing between the two solutions was prevented by their different viscosity.

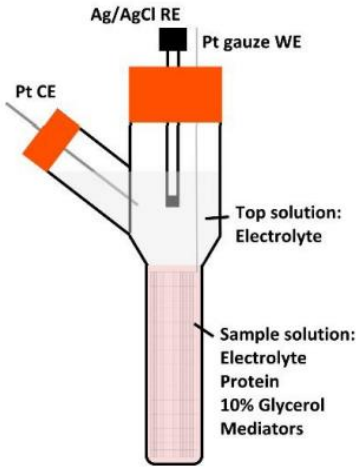

Figure 2.4. Diagram of spectro-electrochemical cell setup. The lower portion of the cell, containing the sample solution has a pathlength of 0.3 mm, while the upper part containing only the buffer widens to a diameter of 2 cm. Reproduced with permission from reference [12].

The applied potential was varied with selected discrete steps (20 to 50 mV) and UV-Vis spectra were collected at each potential value after 30 minutes of equilibration time. Both a reduction and an oxidation scan were acquired in each experiment to check equilibration. Applied potential values were subsequently reported versus NHE (Normal Hydrogen Electrode), considering -225 mV as the potential of reference electrode.

*2.3.1. pH-dependent SEC titrations of Fe-MC6*a*

For Fe-MC6*a, the first SEC titration was performed at pH 6.5 (100 mM phosphate buffer) in the range from 0 to -300 mV vs NHE.

A red-shift of the Soret peak from 391 nm to 411 nm was observed upon reduction, together with an increased molar absorptivity at the maximum (Figure 2.4). The Q bands, that appeared very broad and weak in the ferric state, became better resolved in the ferrous state. In particular, two Q bands at 523 (β) and 545 (α) nm were observed, with a β/α intensity ratio lower than the unity. These spectral

features display a good correspondence with those reported for several heme-proteins in the ferrous form.[13,14]

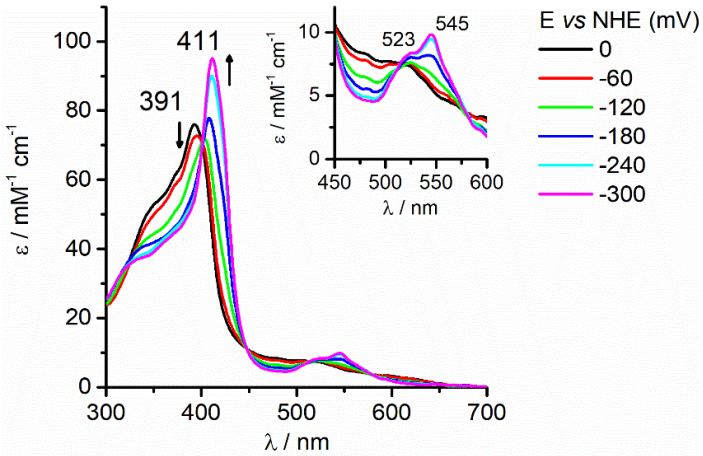

Figure 2.4. Selected spectra acquired during the UV-Vis SEC titration of Fe-MC6*a (100 μM) at pH 6.5 (100 mM phosphate buffer); the inset shows a focus on the Q-band region.

For the determination of the reduction potential, absorbance values at 411 nm from the SEC titration were normalized and plotted as the fraction of reduced species towards the applied potential (Figure 2.5). Data points were fitted to the following function (Equation. 2.2):[12]

$$y = A + \frac{B \cdot 10^{\frac{E_m - x}{59/n}}}{1 + 10^{\frac{E_m - x}{59/n}}} \qquad (2.2)$$

Equation 2.2 was obtained by rearranging the Nernst equation to express the molar fraction of the reduced species (y) as a function of the applied potential (x). E_m stands as the midpoint potential and n represents the number of electrons involved in the redox reaction, while A and B are fitting parameters.

A redox equilibrium with midpoint potential of E_m = - 160 mV was found at pH 6.5 (Figure 2.5A). However, Fe-MC6*a did not display a behaviour consistent with a single redox-active species in the present experimental conditions, because

n ~ 0.5 was found. This finding suggests the presence of two species in solution involved in an acid-base equilibrium.

Data points were thus fitted to a function that takes into account the presence of two species involved in two distinct one-electron redox processes (Equation. 2.3).[12]

$$y = \frac{A + B \cdot 10^{\frac{x - E_{m1}}{59}} + C \cdot 10^{\frac{E_{m2} - x}{59}}}{1 + 10^{\frac{x - E_{m1}}{59}} + 10^{\frac{E_{m2} - x}{59}}} \qquad (2.3)$$

In equation 2.3, y represents the total fraction of reduced species, E_{m1} and E_{m2} are the midpoint potentials of the two redox reactions. The number of electrons (n) of each redox process does not explicitly appear because it is fixed at the value of 1.

Two reduction potentials of - 107 mV and - 207 mV were observed (Figure 2.5B) and were respectively attributed to the His-aquo and the His-hydroxy axial coordination states of Fe-MC6*a. This result is consistent with the pK_a = 6.8, which was found from previously reported UV-Vis pH titrations of Fe-MC6*a and attributed to the deprotonation of the axially bound water ligand.[4]

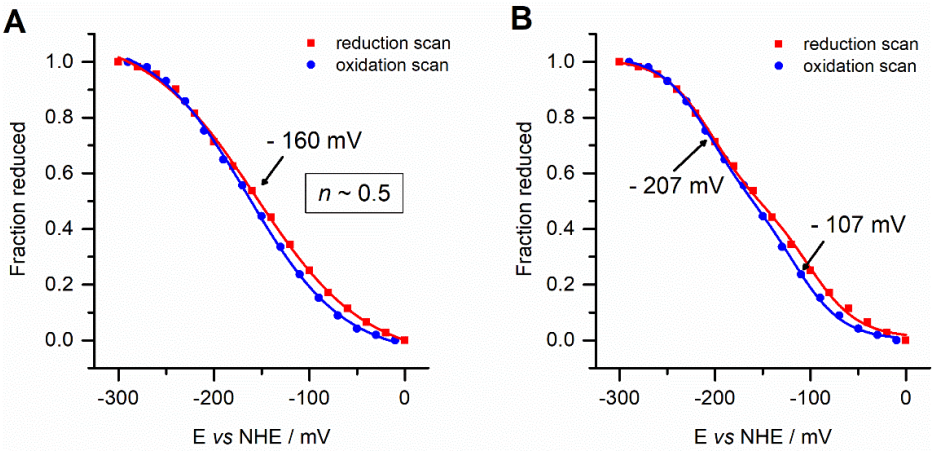

Figure 2.5. SEC titration curves of Fe-MC6*a at pH 6.5. Data points were fitted to: (A) Eq. 2.2 or (B) Eq. 2.3.

SEC titrations were also performed at pH values where a single coordination state was expected to be predominant. Experiments at pH 5.0 (100 mM citrate buffer) and 8.5 (100 mM CHES buffer, 100 mM NaCl) gave midpoints at -97 mV and at -198 mV, respectively (Figure 2.6). These values are in good agreement with those found at pH 6.5. In these cases, data were fitted to the general Nernst model (Equation. 2.2) and values of *n* close to 1 were observed.

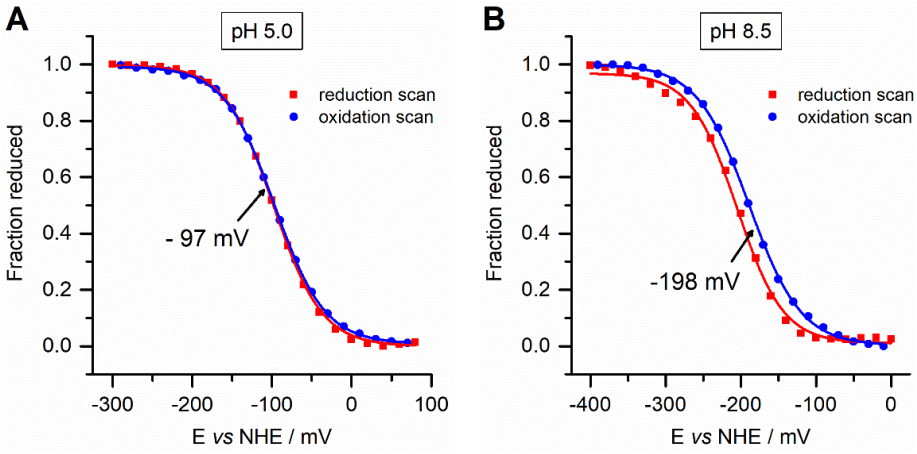

Figure 2.6. SEC titration curves of Fe-MC6*a at (A) pH 5.0 and (B) pH 8.5. Data points were fitted to Eq. 2.2.

The reduction potential of Fe-MC6*a was greatly affected by pH, since a -100mV shift was observed going from pH 5.0 to 8.5. These data indicate that hydroxide binding provides great stabilization to the ferric form relatively to the ferrous form.

*2.3.2. pH-dependent SEC titrations of Mn-MC6*a*

UV-Vis SEC experiments with Mn-MC6*a were performed in a range of applied potential between 0 and -600 mV *vs* NHE, since a lower reduction potential with respect to Fe-MC6*a was expected.

The UV-Vis spectrum of the reduced Mn^{II} form was characterised by a single, very intense Soret band at 419 nm (Figure 2.6).

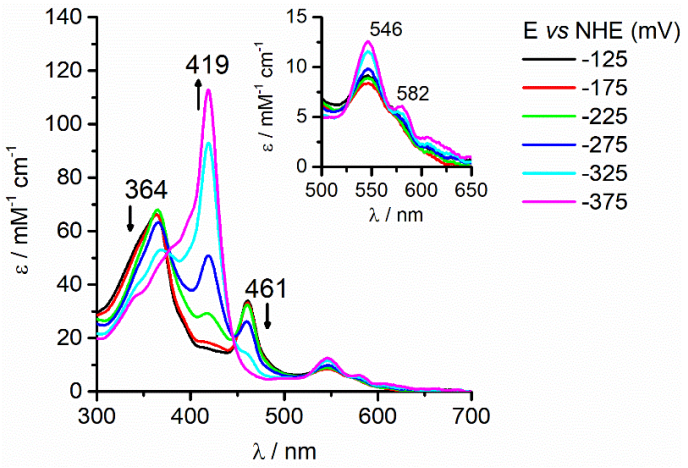

Figure 2.6. Selected spectra acquired during the UV-Vis SEC titration of Mn-MC6*a (30 μM) at pH 6.5 (100 mM phosphate buffer); the inset shows a focus on the Q-band region.

Experiments at pH 6.5 evidenced the presence of a single redox-active species with a midpoint potential of - 293 mV, confirming that the His-aquo axial coordination state is the only present under these conditions (Figure 2.7A). No significant variations in the reduction potential were observed between pH 5.0 and 8.5 (data not shown), supporting that the acid-base equilibrium occurring around pH ~ 7 does not alter the metal first-coordination sphere. The reduction potential of Mn-MC6*a was less sensitive to pH with respect to the Fe analogue. Indeed, a - 50 mV shift was observed increasing the pH to 12.0 (100 mM phosphate buffer; Figure 2.7C), when the hydroxy-bound species was predominant. SEC titrations were also performed at pH 10 (100 mM carbonate buffer; Figure 2.7B), a value close to the pK_a for the water/hydroxide equilibrium found by UV-Vis acid-base titrations.[15] In these conditions, it was not possible to clearly distinguish the contribution of the two species and a midpoint potential of - 313 mV was observed.

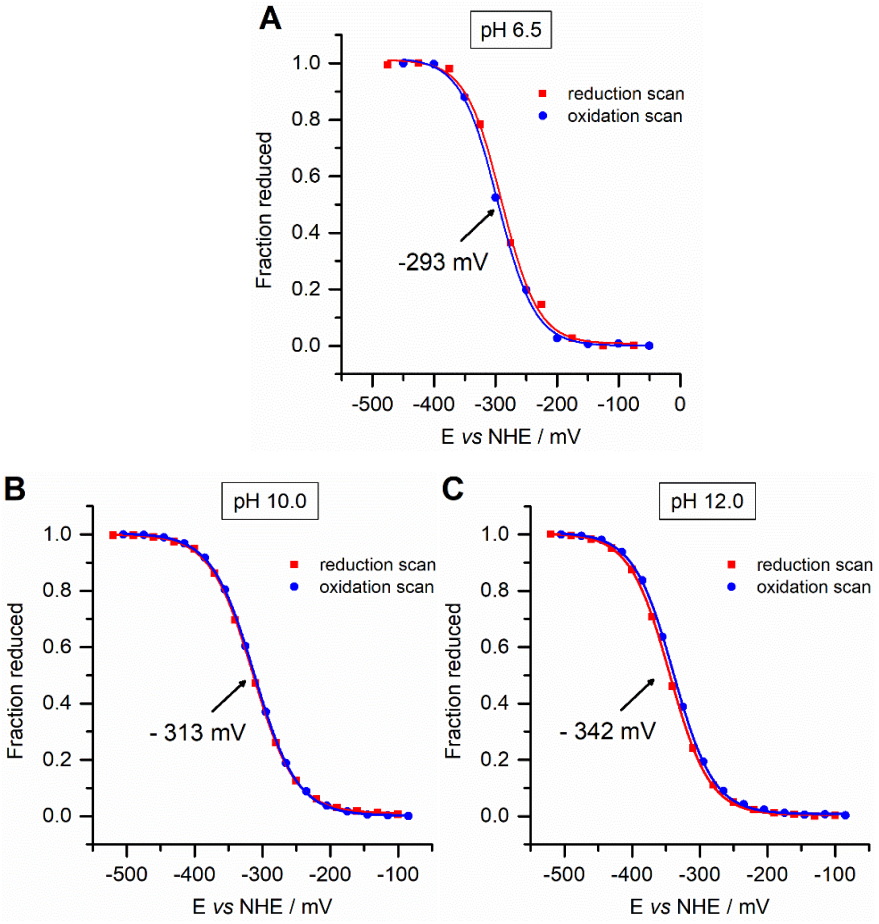

Figure 2.7. SEC titration curves of Mn-MC6*a at: (A) pH 6.5; (B) pH 10.0; (C) pH 12.0. Data points were fitted to Eq. 2.1.

Attempts to measure the reduction potential of the *bis*-H_2O axial coordination states of the catalysts were not successful because the metal ions were lost upon reduction at pH 2.0. This finding indicates that His^6 coordination is essential for the stabilization of the Fe^{II}-and Mn^{II}- porphyrin species.

2.4. Formation of high-valent Mn-species

Spectroscopic studies following the treatment of Mn-MC6*a with oxidizing agents were carried out with the aim to evaluate the formation of high-valent Mn species.

First experiments were carried out by adding an excess of hydrogen peroxide (100 eq.) to a buffered solution (60 mM carbonate containing 40% TFE (*v/v*), pH 10) of the complex (20 μM) and monitoring the evolution of the UV-Vis spectrum over the time. A significant decrease in the intensity of the Soret absorption bands at 358 and 461 nm, with the concurrent appearance of a single Soret band at 393 nm, was observed. In the visible region, the intensity of the band at 547 nm decreased, while three new bands at 504, 530 and 612 nm appeared (Figure 2.8A).

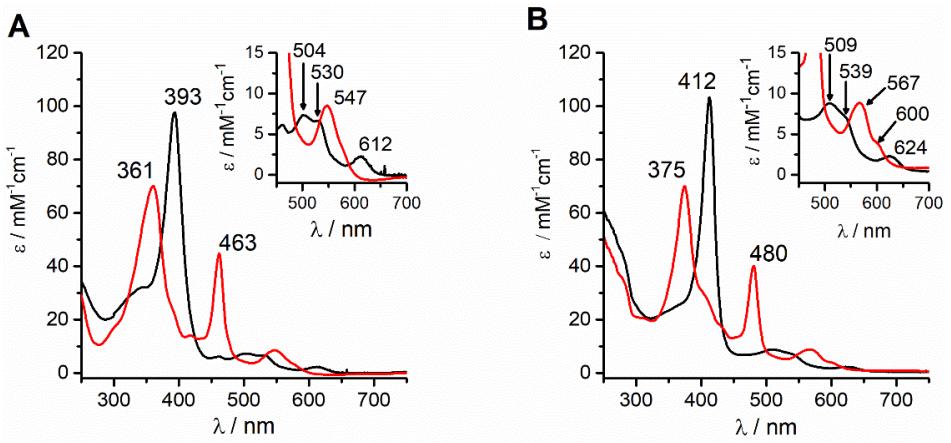

Figure 2.8. Comparative UV-Vis profiles of (A) Mn-MC6*a (20 μM, 60 mM carbonate buffer pH 10 with 40% *v/v* TFE) and (B) Mn-HRP (8 μM, 100 mM phosphate buffer pH 7.0) before (red lines) and after (black lines) addition of 100 eq H_2O_2. The insets show details of the Q-bands.

These spectral changes are consistent with the formation of the oxomanganyl $[Mn^{IV}=O]^{\cdot+}$ radical cation. Indeed, the observed spectroscopic profile closely matches those reported for Mn-reconstituted horseradish peroxidase[16] (Mn-HRP, Figure 2.8B) and Mn-microperoxidase 8 (Mn-MP8)[17] upon reaction with

hydrogen peroxide. In the case of Mn-HRP, this spectrum was attributed to the Mn-analogue of heme-peroxidases Compound I based on EPR studies.[18,19]

Reaction of Mn-MC6*a with *t*-BuOOH (100 eq.), NaOCl (1000 eq.) or $KHSO_5$ (100 eq.) provided the same UV-Vis absorption profile (data not shown), thus excluding the formation of Mn^{V}=O species. This behaviour distinguishes Mn-MC6*a from small-molecule Mn-porphyrin complexes, which are typically able to form both Mn^{IV} and Mn^{V}-oxo species.[20] In this respect, Mn-MC6*a appears more similar to Mn-HRP, which selectively forms the same species (Mn-Compound I) regardless the nature of the oxidizing agent employed.[16,21,22] However, HRP-Mn-Compound I was characterised by a high chemical stability and was formed quantitatively even after equimolar addition of hydrogen peroxide. Conversely, the formation and stability of Mn-MC6*a Compound I was highly dependent from the equivalents of peroxide employed (Figure 2.9).

Mn-MC6*a was quantitatively converted into Mn-Compound I within 5 s upon reaction with 100 eq. of hydrogen peroxide, then underwent complete bleaching within 20 minutes (Figure 2.9A). When lower amounts of peroxide were used, both the observed rate and yield of Mn-Compound I formation decreased, but the catalyst spontaneously returned to the resting state. Yields of Mn-Compound I formation were calculated based on the molar absorptivity at 393 nm detected in the reaction with 100 eq. of hydrogen peroxide. Treatment of Mn-MC6*a with 10 eq. of H_2O_2 led to Mn-Compound I with a 76% yield within 40 s (Figure 2.9B), while the reaction with an equimolar amount of H_2O_2 provided Mn-Compound I in 45% yield within 90 s (Figure 2.9C). Catalyst restoring was also determined considering the intensity of the Soret band of the Mn^{III} species (361 nm) observed when changes were no longer detected in the UV-Vis spectrum. When 10 eq. of hydrogen peroxide were used, 55% of the catalyst was recovered, while the restoring was almost quantitative (> 90%) with 1 eq. of hydrogen peroxide.

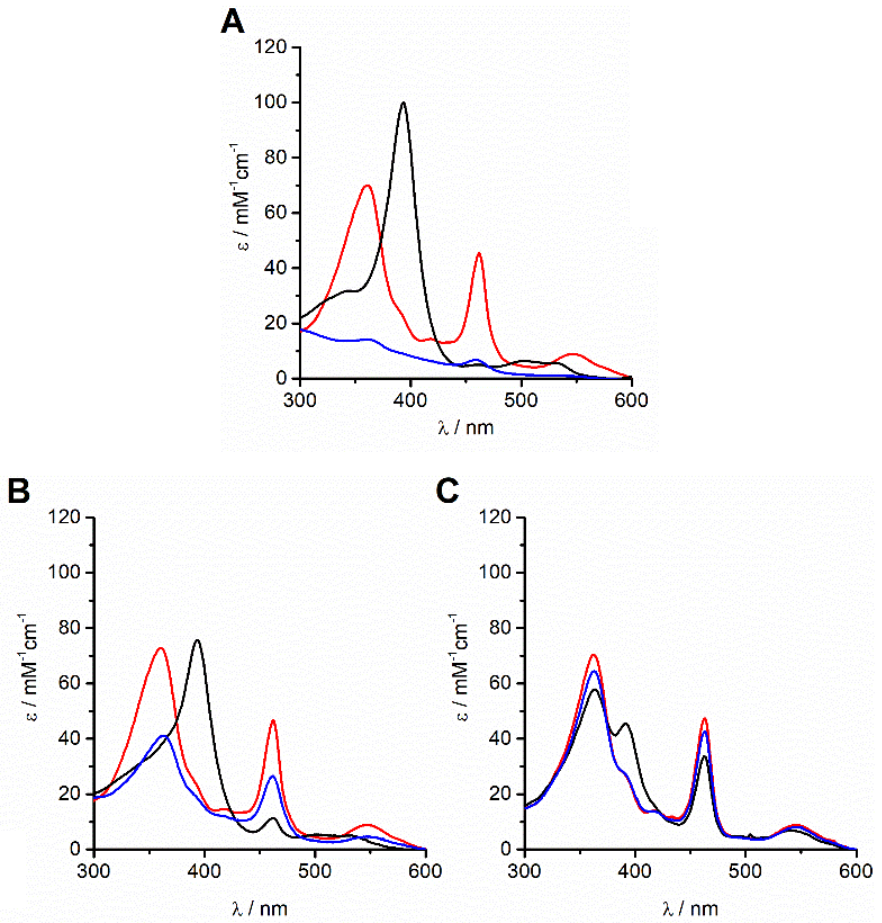

Figure 2.9: UV-Vis spectra of Mn-MC6*a upon treatment with different amounts of H_2O_2: (A) 100 eq.; (B) 10 eq. and (C) 1 eq. Spectra acquired prior to addition of peroxide are depicted as red lines. Black lines represent the maximal conversion of Mn^{III}-MC6*a into Compound I (observed at t = 5 s, 40 s and 90 s after the addition of peroxide for 100 eq., 10 eq. and 1 eq., respectively). Blue lines represent the spectra acquired after 20 minutes by the addition of peroxide. [Mn-MC6*a] = 20 μM in 60 mM carbonate buffer containing 40% TFE (*v/v*), pH 10; T = 25 °C.

The effect of pH on the rate of H_2O_2 activation by Mn-MC6*a was also evaluated. The time-course of the reaction was monitored by following the variations in the absorbance at 393 nm upon addition of H_2O_2 under different pH conditions

(Figure 2.10). Kinetic assays were carried out using 1 eq. of H_2O_2 in order to better highlight the differences between the different pH conditions screened. The initial rates of Compound I formation are reported in Table 2.3.

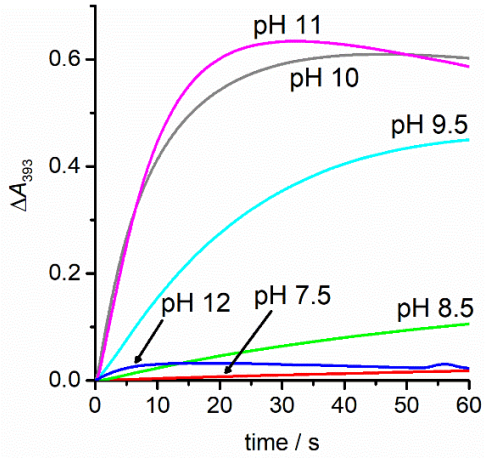

Figure 2.10. Time-course of Mn-Compound I formation in different pH conditions. Experimental curves at different pH are reported with different colours: pH 7.5, red; pH 8.5, green; pH 9.5, cyan; pH 10, grey; pH 11, magenta; pH 12, blue. ΔA^{393} represents the absorbance at 393 nm subtracted of the initial value. *Reaction conditions*: Mn-MC6*a, 20 µM; H_2O_2, 20 µM; T=25°C. Various buffers were used depending on the pH, as described in Section 3, Materials and Methods.

Table 2.3: Initial rates (v_0) of Mn-Compound I formation in different pH conditions.

pH	***v*₀ (10^{-2} µM s^{-1})**
7.5	0.39
8.5	2.56
9.5	16.4
10.0	62.8
11.0	57.2
12.0	5.74

The formation of Mn-Compound I was remarkably slow at pH values below 7.5 and a negligible amount of the high-valent species was observed. The initial reaction rate was greatly influenced by pH, reaching the highest value at pH 10.0. At pH 11.0, a similar oxidation rate was observed, even though a subsequent decay of the $[Mn^{IV}=O]^{\cdot+}$ species occurred. A significant drop in the reactivity was then found above pH 11, which may be attributed to either the decomposition of hydrogen peroxide in the alkaline medium and/or to Compound I instability.[23]

2.5. Discussion

The spectroscopic characterisation of Mn-MC6*a allowed to highlight similarities and differences with respect to the iron analogue.

CD studies in the far UV region evidenced that TFE exerts an essential role in the folding of the peptide chains. The presence of an iso-dichroic point at 202 nm suggests that TFE induces a transition from a random coil to an α-helical conformation,[6] that appears to be complete at 40% TFE (*v/v*). As expected, Fe- to Mn- substitution does not greatly affect the folding of the peptide chains. Indeed, both complexes reach the maximum α-helical content at similar TFE concentrations (50% TFE (*v/v*) for Fe-MC6*a).[1] As reported earlier for this class of compounds,[1,5,24] CD analysis in the Soret region highlights that the helical folding drives the peptide chains to interact with the porphyrin moiety, with a consequent stabilization of the global sandwiched structure.

Even though metal substitution does not alter the structural properties of the molecule, pH-titration studies by UV-vis spectroscopy revealed some fundamental differences concerning the metal coordination properties. For Fe-MC6*a, two acid-base equilibriums were found centred at $pK_{a1} = 4.0$ and $pK_{a2} = 6.8$.[1] The first equilibrium was interpreted as the deprotonation of His^6 and its consequent coordination to the metal ion, while the latter was attributed to the deprotonation of a water molecule at the sixth coordination position of the heme

iron. His[6] coordination seems to occur under identical conditions even for Mn-MC6*a, since an equilibrium centred at pK_{a1} = 4.0 was also detected. Conversely, the deprotonation of the metal-bound water ligand occurs 3 units of pH higher in the case of the Mn-complex (pKa_3 = 9.8), reflecting the lower Lewis acidity of Mn^{III} compared to Fe^{III}.[25] An additional acid-base equilibrium was detected for Mn-MC6*a at pH values falling between the other two equilibria (pK_{a2} = 7.0). It is possible that other amino acid side-chains participate to this equilibrium (*e.g.* Asp[1] on the tetradecapeptide chain) creating a second-shell interaction that influences the UV-Vis absorption properties of the complex. This equilibrium was not detectable in studies with Fe-MC6*a, whose absorption properties appear less sensitive to changes in the coordination environment, compared to those of the Mn-analogue. The presence of this equilibrium does not significantly alter the redox properties of Mn-MC6*a, since the reduction potential was found to be pH independent in the range between 5.5 and 7.5. This observation provides support to the hypothesis that the ionizable group is not directly bound to the metal ion.

It is worth to note here that the pK_a for Mn-bound water molecule (pKa_3 = 9.8)[15] is lower compared to other Mn-porphyrin peptide conjugates such as Mn-microperoxidase 8 (Mn-MP8, pK_a = 11.2)[17] and Mn-GGH (pK_a = 12).[23] Likewise, the E_m value obtained for the His-aquo coordination state of Mn-MC6*a (E_m = - 293 mV) is less negative than those reported for Mn-MP8 (E_m = - 0.361 mV *vs* NHE at pH 7.5)[26] and MnGGH (E_m = - 444 mV *vs* NHE)[23] in the same coordination state. This indicates that the relative stability of oxidized relatively to the reduced state is decreased in the Mn-MC6*a complex. The same trends can be observed from a comparison of the pK_a values for water deprotonation and the E_m of His-aquo species of Fe-MC6*a with Fe-MP8[17] and FeGGH.[23] These observations are summarized in Table 2.4.

Table 2.4. Comparison of E_m of the His-aquo species and pK_a for water deprotonation of metalloporphyrin-peptide conjugated systems.

Species	pK_a [ref.]	E_m (mV *vs* NHE) [ref.]
Fe-MC6*a	6.8 [4]	- 97
Fe-MP8	9.2[26]	- 207[16]
Fe-GGH	9.0[23]	- 255[23]
Mn-MC6*a	9.8[15]	- 292
Mn-MP8	11.2[26]	- 361[16]
Mn-GGH	12.0[23]	- 444[23]

As widely reported in the literature for heme-proteins and metalloporphyrin complexes,[27,28] solvent accessibility to the metal cofactor is also responsible of variations in the redox potential. In particular, a hydrophobic core, causing water exclusion from the heme environment, determines a positive shift in the reduction potential. Thus, the observed shift of the E_m value for the His-aquo form of both Mn- and Fe-MC6*a, with respect to MP8 and GGH metal derivatives, can be also attributed to a different environment around the metallo-porphyrin. Both MP8 and GGH lack a distal peptide chain, and therefore one side of the porphyrin is fully exposed to the solvent. On the opposite, the presence of the distal decapeptide chain in MC6*a creates a different environment, with a hydrophobic patch formed by the Aib methyl groups.[29] In such an environment, the reduced form of the redox center, as well as the His-hydroxy oxidized form, would be stabilized, thus causing a positive shift of the reduction potential and a downshift of the bound water pK_a value with respect to metal derivatives of MP8 and GGH. Finally, the hydrogen bond network within residues of the designed distal pocket may also play a role in favouring water deprotonation (Figure 2.11)

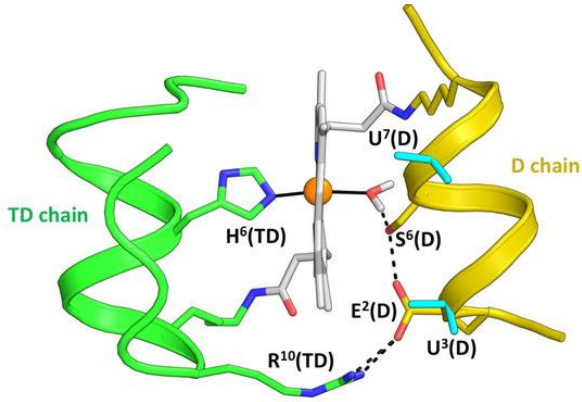

Figure 2.11. Designed model of MC6*a metal complex, with highlighted the hydrogen bond network between the residues in the metal-bound water molecule and the residues (Ser^6 and Glu^2) in the distal site. Adapted with permission from reference [1].

Reaction of Mn-MC6*a with hydrogen peroxide produced a high-valent Mn-oxo species, whose spectral features match those of Mn-Compound I of Mn-HRP. Mn-Compound I formation was negligible at pH lower than 7.5, when the His-aquo coordination state is predominant in solution. The highest rate and yield of Mn-Compound I was observed at pH = 10, which is 3.5 pH units higher compared to the best conditions for peroxidase activity found for Fe-MC6*a (pH 6.5). The alkaline pH value corresponding to the maximum reaction rate in Mn-Compound I formation is not unexpected. Indeed, as previously reported for manganese reconstituted heme-proteins and for model systems, manganese is less efficient than iron in lowering the pK_a value of H_2O_2. Thus, a pH increase is required in order to assist H_2O_2 deprotonation, which is necessary for peroxide heterolytic cleavage and Compound I formation.[16,25,30,31] Among peptide-porphyrin complexes, we evidenced that the pK_a of the distal axial ligand of Mn- and Fe-MC6*a is downshifted as compared with Mn- and Fe-MP8, respectively. This most likely explains that the maximum reactivity towards hydrogen peroxide for our complexes (pH 6.5 for Fe-MC6*a and pH 10 for Mn-MC6*a) is observed at lower pH values with respect to MP8 complexes (pH 9 for Fe-MP8 and pH 11.9

for Mn-MP8).[31] Based on these results, it appears that Fe- and Mn-MC6*a approach the properties of native HRP (optimum pH = 4.6 for ABTS oxidation)[5] and Mn-reconstituted HRP (highest reactivity for Mn-Compound I formation at pH 7)[16] better than the corresponding metal complexes of MP8.

3. SULFOXIDATION OF PHENYL THIOETHERS

3.1. Thioether oxidation catalysed by Mn-MC6*a

The catalytic properties of Mn-MC6*a in promoting the oxygenation of organic substrates were investigated. In first studies, the oxidation of phenyl thioethers was chosen as a model reaction. Since the ability of the Mn-complex to activate hydrogen peroxide was established, catalytic assays were first conducted under the optimized conditions found for the formation of Mn-Compound I ([Mn-MC6*a] = 20 μM; Mn-MC6*a:H_2O_2 = 1:100, pH 10.0). Thioanisole was used as substrate in equimolar concentrations with respect to hydrogen peroxide. The reaction progress was monitored by GC-MS analysis at fixed times during the course of the reaction. Substrate conversion was determined using the internal standard method (see Section 3, Materials and methods for a detailed description of the experimental procedure).

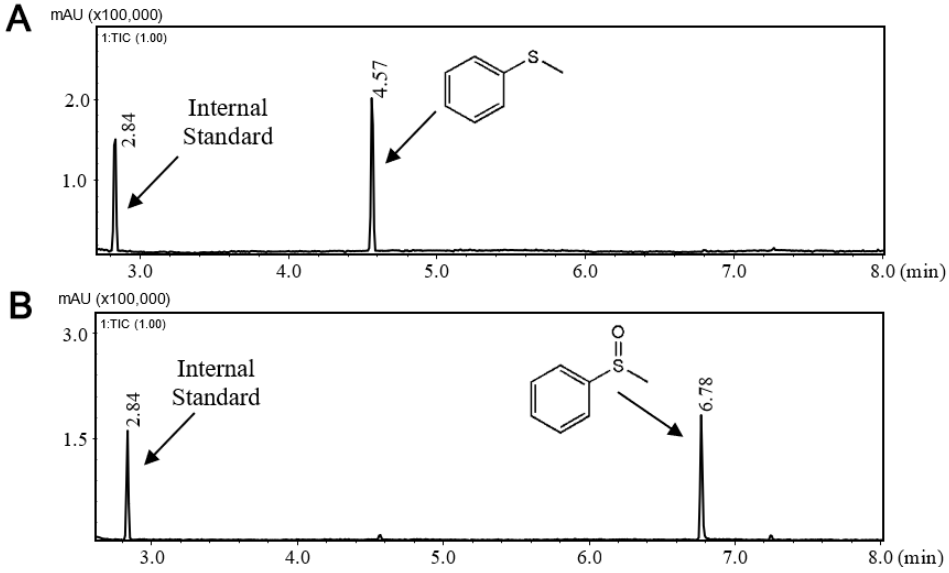

Figure 3.1. GC-MS TIC profile of thioanisole sulfoxidation: (A) before addition of peroxide and (B) after 5 minutes of reaction. Peak eluted at Rt = 2.84 min is relative to anisole (internal standard).

In these conditions, Mn-MC6*a acted as a fast and chemoselective catalyst, since complete conversion of the substrate into the corresponding sulfoxide was achieved within the first 5 minutes (Figure 3.1).

As the formation of Mn-Compound I was found to be strongly pH-dependent, the effect of pH on thioanisole sulfoxidation was evaluated to investigate the role of the high-valent Mn-oxo species as the reactive intermediate in the oxygenation of the substrate. Reactions were carried out in different pH conditions (from 6.5 to 11) and substrate consumption after 5 minutes was monitored (Figure 3.2A).

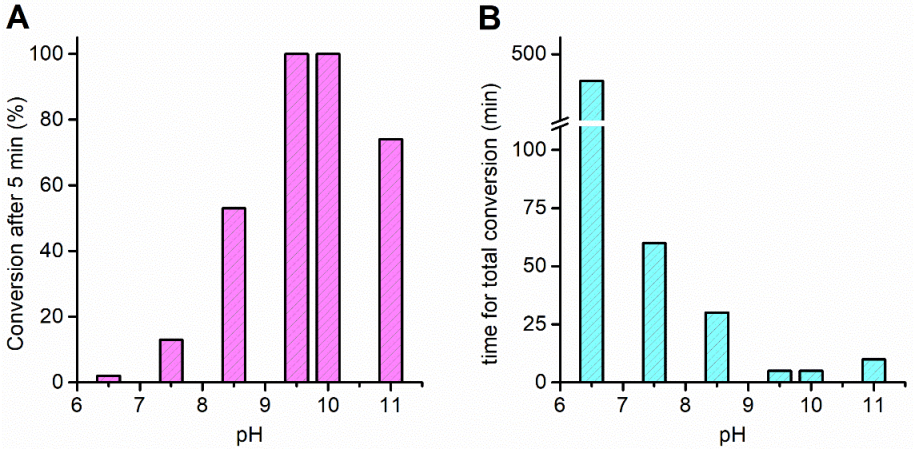

Figure 3.2. pH-dependent oxidation of thioanisole catalysed by Mn-MC6*a. (A) Substrate conversion observed after 5 minutes by the addition of the oxidant; (B) time required for a complete conversion of the substrate. *Reaction conditions*: Mn-MC6*a, 20 μM; H_2O_2, 2.0·mM; thioanisole 2.0 mM; different buffers were used depending on the pH value examined, as described in Section 3, Materials and Methods.

Substrate conversion was very low at pH 6.5 (2% conversion after 5 minutes). A considerable increase (up to 50-fold) was observed by raising the pH, reaching a complete conversion of the substrate at pH 9.5. No differences were detectable between pH 9.5 and pH 10. A further increase of pH caused a small drop in reaction yield (74% conversion at pH 11).

When the reactions were carried out for longer times, complete conversion of the substrate was observed in almost all cases, even though on different timescales (Figure 3.2B). The time required for total conversion progressively decreased by increasing pH, reflecting the trend observed for the partial conversion at 5 minutes. The reaction proceeded very slowly at pH 6.5, and an overall time of 7 h was required for the complete consumption of the starting material. As a unique exception, the reaction stopped at 74% conversion at pH 11, but complete conversion was rapidly achieved upon further addition of hydrogen peroxide (100 eq.). This behaviour excludes that a lowering of the reaction yield was caused by catalyst inactivation, while it suggests the occurrence of an alternative pathway that involves unproductive consumption of hydrogen peroxide at pH > 10. Control reactions in the absence of the catalyst were also carried out in the same experimental conditions ([thioanisole] = 2 mM; [H_2O_2] = 2 mM; pH 6.5 – 11.0) and no significant product formation was observed over the same timescales.

UV-Vis analysis performed after reaction completion (5 min) revealed substantial (78 %) catalyst recovery at pH 9.5 (Figure 3.3).

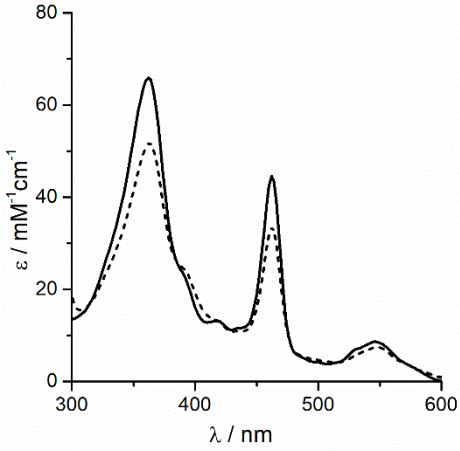

Figure 3.3. UV-Vis absorption spectra collected before (plain line) and after (dashed line) thioanisole sulfoxidation by Mn-MC6*a at pH 9.5.

This result points out the protecting role exerted by the substrate during turnovers, since complete catalyst degradation was observed upon treatment with 100 eq. H_2O_2 in the absence of external substrates (see Figure 2.9A in Section 2.4). The recovery of the catalyst after complete substrate consumption in the explored experimental conditions (Mn-MC6*a:substrate:H_2O_2 = 1:100:100) also indicates that Mn-MC6*a could be able to perform more than 100 turnovers.

Experiments were subsequently carried out using increasing amounts of substrate, with the aim of determining the total turnover number (TON) of Mn-MC6*a in thioanisole sulfoxidation. When the reaction was performed using 1000 eq. of substrate (20 μM Mn-MC6*a; 20 mM H_2O_2; 20 mM thioanisole, pH 9.5), the catalyst promoted an 87% conversion of the substrate, thereby it was judged able to perform 870 turnovers in this reaction.

Mn-MC6*a was also screened in the sulfoxidation of several phenyl thioethers, to evaluate the role of activating or deactivating groups by electronic or steric effects on the reaction outcome. To this aim, *p*-chlorothioanisole, *p*-nitrothioanisole, *p*-methoxythioanisole and cyclopropyl-phenyl sulphide were used as substrates. Similar reactivities were observed among all substrates. The reaction proceeded with high chemoselectivity between the sulfoxide and the sulfone products in all cases. In particular, no traces of sulfone were detected for all substrates except of *p*-chlorothioanisole, whose oxidation resulted in the formation of 77% sulfoxide and 13% sulfone. The enantioselectivity of the catalyst was also investigated by performing GC-MS analyses of the reaction mixtures on a chiral column. Unfortunately, no detectable enantiomeric excess was observed in all cases.

3.2. Investigation of the sulfoxidation mechanism

The pH-dependent profile of thioanisole sulfoxidation well correlates with the pH-dependent formation of Mn-Compound I. This finding strongly suggests the involvement of the high-valent Mn-oxo species as the reactive intermediate in

substrate oxygenation. To gain insight into the reaction mechanism, thioanisole oxidation catalysed by Mn-MC6*a was carried out using ^{18}O-labeled hydrogen peroxide as the oxidant. GC-MS analysis of the reaction mixture evidenced complete incorporation of ^{18}O label into the sulfoxide product (Figure 3.4). This result indicates that Mn-MC6*a promotes thioanisole sulfoxidation in a peroxygenase-like mechanism, with the incorporation of the ^{18}O atom, derived from hydrogen peroxide, mediated by the Mn^{IV}-oxo intermediate.

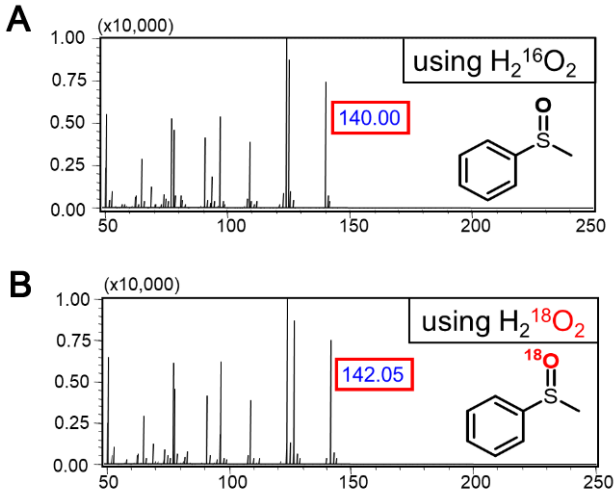

Figure 3.4.: EI-MS spectra of methyl-phenyl sulfoxide observed in thioanisole oxidation using (A) H_2O_2 or (B) ^{18}O-labeled H_2O_2.

The reaction mechanism could either occur through a direct oxygen transfer, involving the nucleophilic attack of the sulphide to Mn-Compound I, or a two-step single-electron transfer process, involving the formation of a substrate-based radical and a non-radical Mn^{IV}-oxo (Mn-Compound II) intermediate (Scheme 3.1).[32]

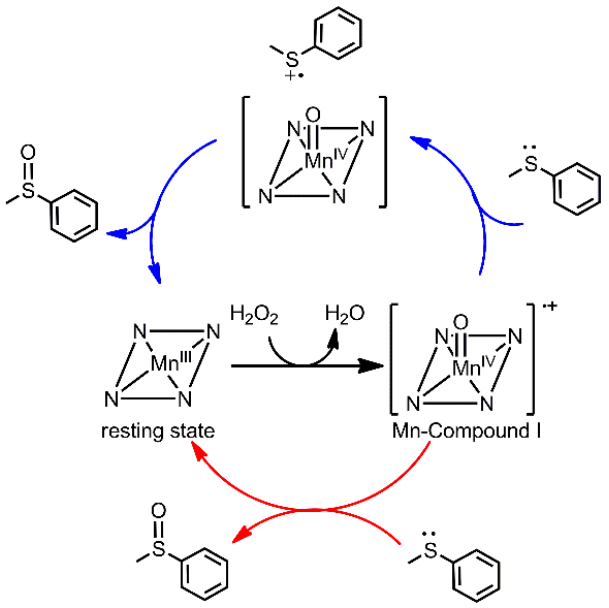

Scheme 3.1.: Schematic representation of thioanisole oxidation mechanism by Mn-MC6*a involving a two-step single electron transfer process (blue arrows) or a direct oxygen transfer (red arrows).

In order to elucidate this aspect, thioanisole oxidation was monitored by UV-Vis spectroscopy. Differently from the other catalytic assays, the reaction was not initialized by addition of hydrogen peroxide to a solution of the catalyst preloaded with the substrate. Mn-Compound I was pre-formed upon reaction of H_2O_2 (2 mM) with Mn-MC6*a (20 µM), then thioanisole (2 mM) was suddenly added when the highest content of the Mn^{IV}-oxo species was observed. Addition of the substrate led to a rapid decrease of the absorption bands associated to Mn-Compound I with the concurrent increase of those associated to the catalyst resting state (Figure 3.5).

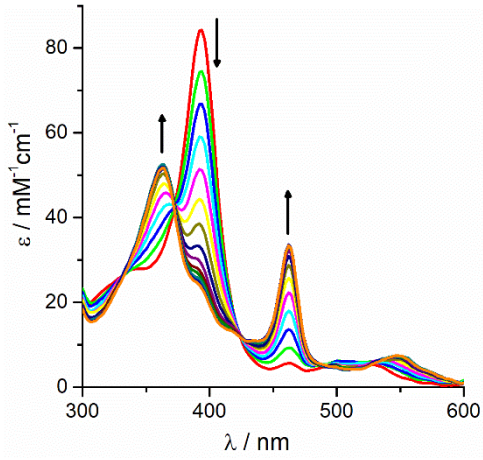

Figure 3.5. UV-Vis absorption spectra collected upon addition of thioanisole to Compound I of Mn-MC6*a; arrows indicate the direction of absorbance variations during reaction progress. *Reaction conditions*: Mn-MC6*a, 20 μM; H_2O_2, 2.0 mM; thioanisole 2.0 mM; 60 mM carbonate buffer with 40% TFE (*v/v*), pH 9.5; T=25°C.

The presence of isosbestic points at 332, 373, 424 and 491 nm indicates a single-step conversion from the Mn^{IV}-oxo species to Mn^{III} without the presence of any detectable intermediate. This observation indirectly excludes a mechanism involving multiple-steps and appears to be consistent with a direct oxygen-transfer mechanism. Furthermore, an almost complete recovery of Mn-MC6*a was observed (87% based on the Soret band absorbance), indicating negligible catalyst degradation.

3.3. Thioether oxidation catalysed by Fe-MC6*a

Fe-MC6*a has been already demonstrated to behave as a very efficient catalyst towards peroxidase-like reactions.[29] Sulfoxidation of phenyl thioethers was studied also with Fe-MC6*a as catalyst, with the aim of investigating the reactivity of the putative ferryl-oxo Compound I towards oxygenation reactions.

Reactions were first performed in the best conditions found for peroxidase catalysis (pH 6.5, 50% TFE *v/v*), using the same concentrations of all the reagents

as in the assays with Mn-MC6*a. Complete conversion of the substrate was achieved within the first 5 minutes in these experimental conditions. A decrease in substrate consumption was observed by increasing the pH up to 9.5, where 62% conversion was achieved in the first 5 minutes of reaction progress.

As observed with Mn-MC6*a, reactions proceeded with high chemoselectivity, since no traces of aryl sulfones were detected.

In the case of Fe-MC6*a, UV-Vis monitoring of the reaction between Compound I and thioanisole cannot provide a clear indication of the reaction mechanism, because the Fe^{III} and the Fe^{IV}-oxo species have very close Soret absorption wavelengths.

Isotopic labelling experiments were performed using ^{18}O-labelled hydrogen peroxide and, similarly to Mn-MC6*a, complete incorporation of labelled oxygen atom into the sulfoxide was found. These results strongly suggest that the reaction proceeds through a peroxygenase mechanism also in the case of Fe-MC6*a.

Under optimized reaction conditions (Fe-MC6*a, 10 μM; thioanisole, 20 mM; H_2O_2, 20 mM, pH 6.5, 50% *v/v* TFE), the catalyst was able to perform 1500 turnovers in thioanisole oxidation.

3.4. Discussion

Spectroscopic characterization provided evidences for the formation, upon treatment of Mn-MC6*a with hydrogen peroxide, of a high-valent Mn-oxo species identified with Mn-Compound I. Furthermore, this species was demonstrated to promote the oxygenation of phenyl thioethers in high yields. Experimental evidences indicate that the reaction occurs through a direct oxygen transfer from Mn-Compound I to the substrate. A similar peroxygenase activity was also detected for Fe-MC6*a, previously demonstrated to be one of the most stable and efficient catalysts in peroxidase reactions.[29]

It is worth noting that the activity of Fe- and Mn-MC6*a places them among the most active artificial biocatalysts available to date in the H_2O_2-mediated thioanisole oxidation.[33–38] In particular, a comparison of the catalytic performance in terms of TON between our catalysts and a variety of artificial metalloenzymes (Table 3.1) reveals that Mn-MC6*a and Fe-MC6*a are among the most robust catalysts.

Table 3.1. H_2O_2 mediated sulfoxidation of thioanisole catalysed by different metalloenzymes.

Catalyst	Catalyst:substrate:H_2O_2 (catalyst concentration)	Yield, % (time, min)	TON	Ref.
Mn-MC6*a	**1:100:100 (20 μM)**	**100 (5)**	**870[a]**	[15]
Fe-MC6*a	**1:100:100 (20 μM)**	**97 (5)**	**1500[b]**	[15]
Mn-HRP	1:100:100 (9 μM)	4 (5)	4	[15]
Fe-HRP	1:30:40 (330 μM)	95 (60)	28	[39]
Cr-salophen-Mb(H64D/A71G)	1:100:100 (10 μM)	–[c]	–[c]	[33]
Mn-Cor-BSA	1:50:75 (200 μM)	83 (90)	150	[34]
Fe(T*p*CPP)-Xln10A	1:425:175 (20 μM)	85 (138)	145	[35]
Mn-salen-Mb(T39C/L72C)	1:40:40 (130 μM)	17 (10)	7[d]	[38]
Fe-T*p*SPP-NCS-3.24	1:500:500 (5 μM)	1.3 (120)	6.5[d]	[36]
CoL-BSA	1:100;150 (2.7 μM)	98 (1680)	98[d]	[37]

[a] TON was determined using a 1:1000:1000 catalyst:substrate:H_2O_2 ratio.

[b] TON was determined using a 1:2000:2000 catalyst:substrate:H_2O_2 ratio.

[c] Yield and TON not available from the reference. The reported reaction rate is $78 \cdot 10^{-3}$ TON min^{-1}.

[d]TON was calculated based on the reported yield and catalyst:substrate ratio.

SECTION 2: *Results and discussion*

A comparison of Fe-MC6*a and Mn-MC6*a with native and manganese-reconstituted HRPs revealed interesting features of the miniaturized protein scaffold. It is well known that HRP is evolved for the reduction of hydroperoxides because of its binding pocket, which is able to properly accommodate H_2O_2. Its high valent iron-oxo intermediate (Compound I) usually catalyses one- or two-electron oxidations of several substrates with high efficiency.[40] Native HRP is not efficient in promoting peroxygenase reactions, in which the two-electron reduction of Compound I is coupled to the transfer of the ferryl oxygen to a substrate. The only exception is the sulfoxidation of phenyl thioethers.[39] However, HRP mutants with decreased steric hindrance on the heme distal site showed an enhanced peroxygenase activity, thus highlighting that direct interaction with substrates is hindered by intrinsic inaccessibility of the ferryl oxygen in the native protein.[41–43] Further, oxidation of substrates by HRP through oxygen transfer is in competition with enzyme inactivation by spontaneous self-oxidation. The rate of enzyme inactivation strongly depends on the concentration of oxidants and the nature of the reducing substrate.[39,44] Indeed, an enhancement in the peroxygenase activity of peroxidases has been obtained by keeping the concentration of H_2O_2 at a low level.[44] Manganese substitution in HRP causes a further decrease in its peroxygenase activity, because the high chemical stability of Mn-HRP Compound I[22] prevents any reactivity in oxygen-transfer reactions.

For a straightforward comparison with our systems, the reactivity of native HRP and Mn-HRP were analysed under the same experimental conditions used with MC6*a catalysts, *i.e.* catalyst/oxidant/substrate ratio 1:100:100. Under these conditions, native HRP showed poor peroxygenase activity (10% yield, Table 3 entry 4), probably because of catalyst inactivation by excess peroxide. Substitution of iron to manganese caused a further decrease in peroxygenase reactivity (4% yield, Table 3 entry 3). Instead, in the case of MC6*a, swapping of iron to manganese leaves the catalytic activity almost unchanged. This behaviour

endows our complex with broad catalytic activity and versatility. The finding that oxygenation of thioanisole can be performed with high efficiency at two very different pH values, simply changing iron to manganese (pH 6.5 and 9.5, respectively) can be important for applications with pH sensitive substrates.

4. INDOLE OXIDATION

Based on the catalytic potential of Fe- and Mn-MC6*a discussed in the previous section, subsequent research has been focused to widen the scope of transformations accessible by these catalysts in oxidative chemistry. To this aim, indole oxidation has been chosen as test reaction.

4.1. Indole oxidation by heme-proteins and metallo-porphyrins: a challenge for selectivity

Over the last decades, indole oxidation has become a widespread model reaction to test the efficacy of heme-protein catalysts and their mimics.[45–51] Despite the structural simplicity of this molecule, indole oxidation commonly results in the formation of a large number of products, including mono-oxygenated, doubly oxygenated and dimeric compounds (Scheme 4.1).

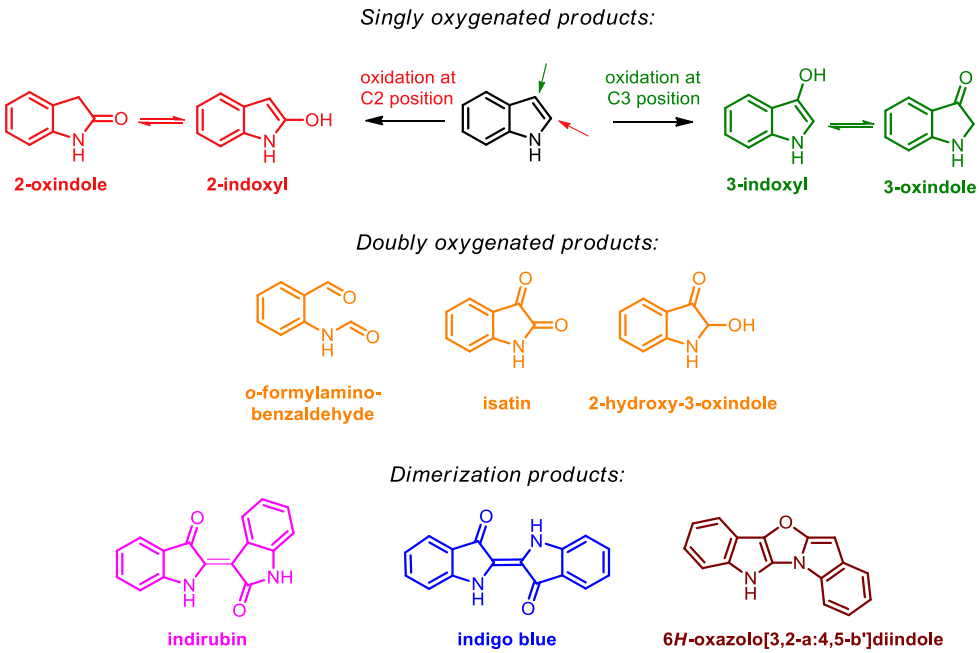

Scheme 4.1. Most representative indole oxidation products, including mono-oxygenated, di-oxygenated and dimeric compounds.

Among metalloporphyrin complexes, a comparative study between Fe- and Mn-based catalysts evidenced different product selectivity depending on the nature of the metal ion, with the Mn-porphyrin system displaying moderate selectivity (64%) towards 2-oxindole and the Fe-porphyrin producing modest amounts of indigo dye (20% selectivity).[45]

The majority of heme-proteins catalysed indole oxidation providing mixtures of products (Scheme 4.2). Among them, almost all enzymes produced 2-oxindole as the major reaction product, along with variable amounts of other by-products. Human cytochromes P450s predominantly formed 2-oxindole and the fused pentacyclic compound 6*H*-oxazolo[3,2-*a*:4,5-b']diindole , with a ratio depending on the enzyme isoform.[46] The tryptophan catabolizing enzyme indoleamine 2,3-dioxygenase (IDO) also showed peroxygenase activity towards indole, leading to a mixture of 2- and 3-oxindole and minor amounts of over-oxidized products.[47] Dehaloperoxidase from *Amphitrite ornata* promoted the formation of 3-oxindolenine in comparable amounts with 2-oxindole.[48] In all cases, weaker selectivity towards any of the reaction products was observed. In contrast to native proteins, an engineered myoglobin (F43Y Mb) was recently reported to promote the selective formation of the commercial dye indigo blue (80% selectivity).[49] Even though mechanistic hypotheses have been proposed to explain the product distribution observed in each case, no strong evidences have been reported and the detailed mechanism of heme-catalysed indole oxidation remains not completely understood.

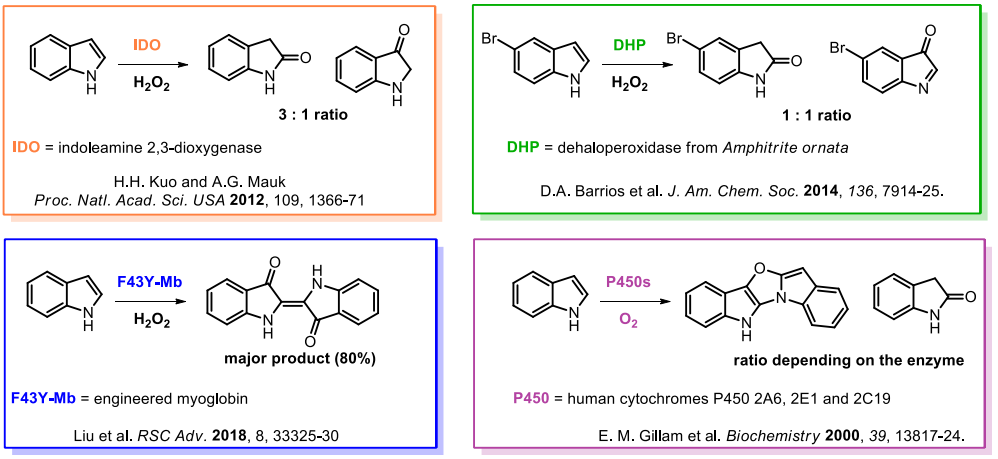

Scheme 4.2. Indole oxidation catalysed by heme-proteins.

Based on the literature data, part of this PhD work has been devoted to study the catalytic properties of Mn- and Fe-MC6*a towards indole oxidation. The main focus of the work was devoted to the identification of the most suited reaction conditions to optimize product selectivity. A variety of variables, including pH and substrate substitution, have been explored, to evaluate their role on product distribution and to provide indication on the reaction mechanism.

4.2. Indole oxidation catalysed by Mn-MC6*a

Catalytic assays with Mn-MC6*a were performed in buffered solutions containing 40% TFE (*v/v*), using hydrogen peroxide as the oxidant and a catalyst/substrate/oxidant ratio of 1:100:100 ([Mn-MC6*a] = 10 μM). Following previous pH-dependent studies on Mn-Compound I formation, experiments were performed at several pH values, in order to explore the role of the Mn-oxo species on product distribution. The reaction progress was monitored at fixed times by analytical RP-HPLC.

*4.2.1. pH-dependence of indole oxidation catalysed by Mn-MC6*a*

Mn-MC6*a acted as a fast and selective catalyst for indole oxidation. A 62% conversion of the starting indole into a predominant oxidation product was observed within 5 minutes at pH 8.5 (Figure 4.1). The main product (87% selectivity) was identified to be 3-oxindolenine based on its UV-Vis absorption profile and high-resolution mass spectrum (HRMS), which were compared with literature data[48] (Figure 4.2).

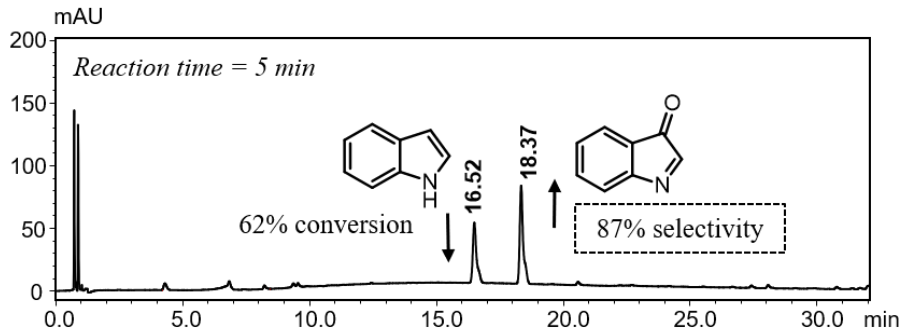

Figure 4.1. HPLC profile of indole oxidation products obtained by Mn-MC6*a catalysis at pH 8.5 acquired after 5 minutes of reaction progress. Arrows indicate changes of peak intensities during reaction. Molecular structures of indole and of the main product are also shown.

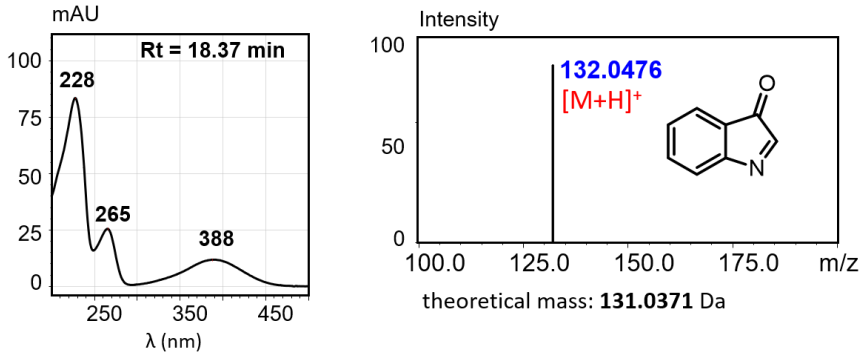

Figure 4.2. Experimental UV-Vis absorption spectrum (left side) and high-resolution mass spectrum (right side) of 3-oxindolenine (Rt = 18.37 min).

It is worth to note that when the reaction was left for longer times at pH 8.5, 3-oxindolenine was gradually consumed with the concurrent formation of a second oxidation product (Figure 4.3). The latter was identified as isatin, based on its MS and UV-Vis properties which were compared with literature data[47,48] (Figure 4.4). Further confirmation was obtained by HPLC and MS analyses of the synthesized standard compound under the same experimental conditions (see Section 3, Materials and Methods).

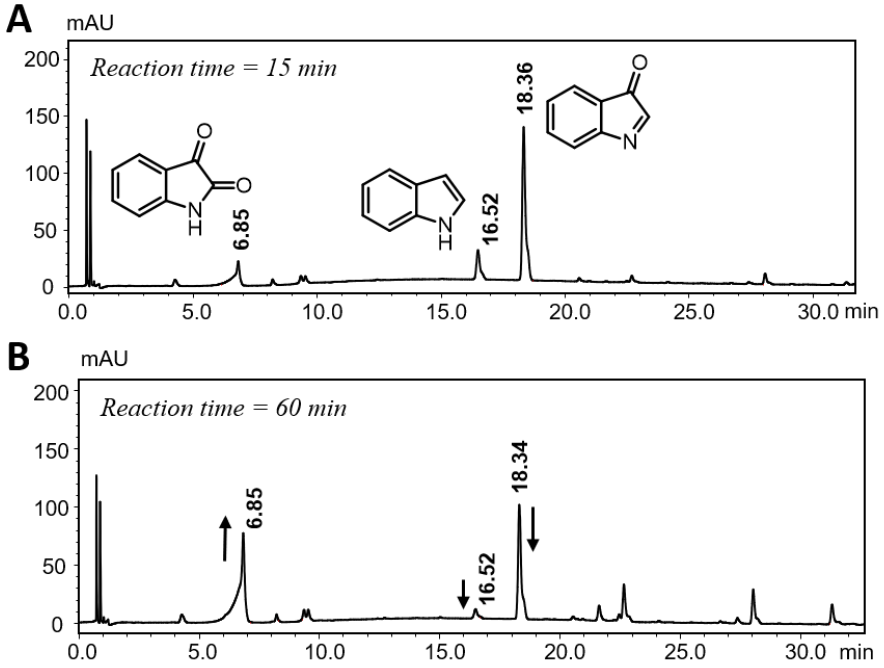

Figure 4.3. HPLC profiles of indole oxidation products obtained by Mn-MC6*a catalysis at pH 8.5 acquired after (A) 15 and (B) 60 minutes of reaction progress. Arrows indicate the intensity variations of the peaks during time.

Product selectivity gradually decreased over longer reaction times (Figure 4.3B), since increasing amounts of by-products were also detected. Among them, 2-oxindole, *o*-formyl-amino-benzaldehyde and dimeric species were identified.

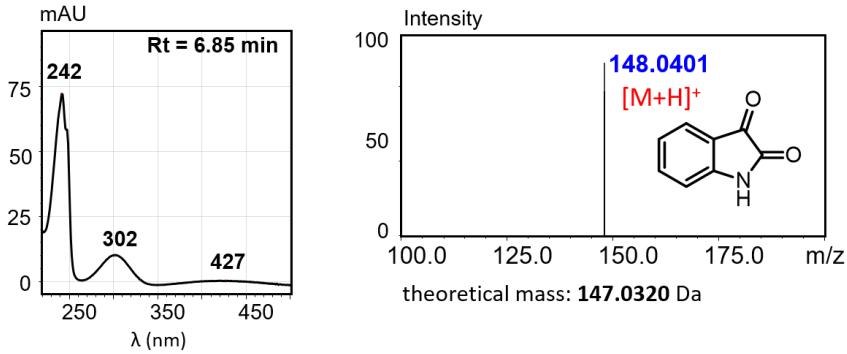

Figure 4.4. Experimental UV-Vis absorption spectrum (left side) and high-resolution mass spectrum (right side) of isatin (Rt = 6.85 min).

In line with the pH-dependent studies of Mn-Compound I formation,[15] the reaction was found to be faster at high pH values, leading to the almost quantitative consumption of indole (90% conversion) within the first 5 minutes at pH 9.5. Under these conditions, isatin represented the predominant product (44%), although a significant quantity of other by-products (22%) was also detected. When reaction pH was moved to 10.5, an enhanced selectivity towards isatin (69%) was observed, while 3-oxindolenine was not detected by HPLC analysis of the reaction mixture after the first 5 minutes. This finding may be interpreted considering that 3-oxindolenine was formed and already consumed within the first 5 minutes. Indeed, HPLC analysis after 1 minute of reaction revealed 83% conversion of the starting indole with 3-oxindolenine (29%) and isatin (34%) present in similar amounts in the reaction mixture. Conversely, the reaction proceeded more slowly at pH 7.5, achieving 34% conversion of the substrate within the first 5 minutes and a high selectivity towards 3-oxindolenine (90%). Results concerning indole conversion and product selectivity in different pH conditions are summarized in Table 4.1 and Figure 4.5.

Table 4.1. Substrate conversion and product distribution observed in indole oxidation catalysed by Mn-MC6*a at different pH values. Data were determined by HPLC analysis of the reaction mixture after 5 minutes of reaction progress.

pH	Conversion (%)	3-oxindolenine (%)[a]	Isatin (%)[a]	Others (%)[b]
7.5	34	90	-	10
8.5	62	87	6	7
9.5	90	32	45	23
10.5	100	-	69	31

[a] Selectivity was calculated as the ratio between the HPLC peak area of the specific product and the sum of all the peaks detected in the chromatogram (excluded the starting material).
[b] Others include all the products with the exception of isatin and 3-oxindolenine.

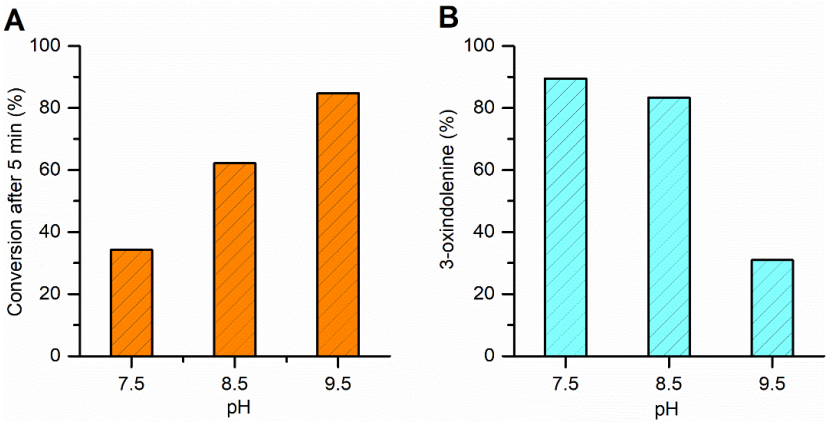

Figure 4.5. pH-dependent oxidation of indole catalysed by Mn-MC6*a. (A) Substrate conversion observed after 5 minutes of reaction progress; (B) selectivity towards 3-oxindolenine. *Reaction conditions*: Mn-MC6*a, 10 μM; H_2O_2, 1.0·mM; indole 1.0 mM; different buffers were used depending on the pH value, as described in Section 3, Materials and Methods.

Indole oxidation was also performed at pH 6.5. These results are not included in Table 4.1 since indole conversion after 5 minutes was negligible. In this case, the reaction proceeded very slowly compared with the previously discussed conditions and longer reaction times were required for substrate conversion. Even though the formation of Mn-Compound I was not significant at this pH value (see

section 2.4), the role of the catalyst was ascertained by performing control experiments in the absence of Mn-MC6*a. Interestingly, a different product distribution was observed (Figure 4.6).

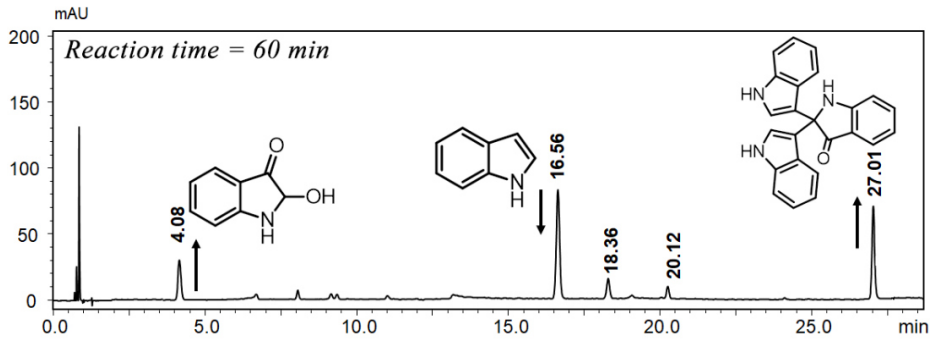

Figure 4.6. HPLC profile of indole oxidation catalysed by Mn-MC6*a at pH 6.5 acquired after 60 minutes by the addition of the oxidant. Arrows indicate changes of peak intensities during the course of the reaction. Chemical structures of indole and of the major reaction products are also shown.

A lower selectivity was found at pH 6.5, with the formation of two main oxidation products. UV-Vis and MS analysis of the product eluted at Rt = 4.1 min revealed complete match with 3-oxindolenine, even though the different retention times in the RP-HPLC analysis highlighted divergent properties. Owing to its lower retention time, the first product detected at pH 6.5 appeared more hydrophilic compared to 3-oxindolenine. Therefore, it was conceivably identified with 2-hydroxy-3-oxindole, which is likely to undergo elimination of a water molecule during the MS analysis. This compound was also detected among minor products (referred as "others" in Table 4.1) in the experiments at higher pH values. The second product observed at pH 6.5 was instead characterised by a highly lipophilic character (Rt = 27.0 min). The UV-Vis profile of this species did not correspond to any of the most common indole oxidation products reported in literature. MS analysis suggested that the trimeric compound 2,2-bis(3'-indolyl)-3-oxoindole was formed in this case (*m/z* 364.147 Th, $[M+H]^+$, Figure 4.7). MS/MS analysis

provided a further indication, since fragmentation of the selected parent ion (364.147 Th) led to signals at $[(M-28)+H]^+$, corresponding to a loss of CO, and at $[(M-117)+H]^+$, attributed to a loss of an indole unit.

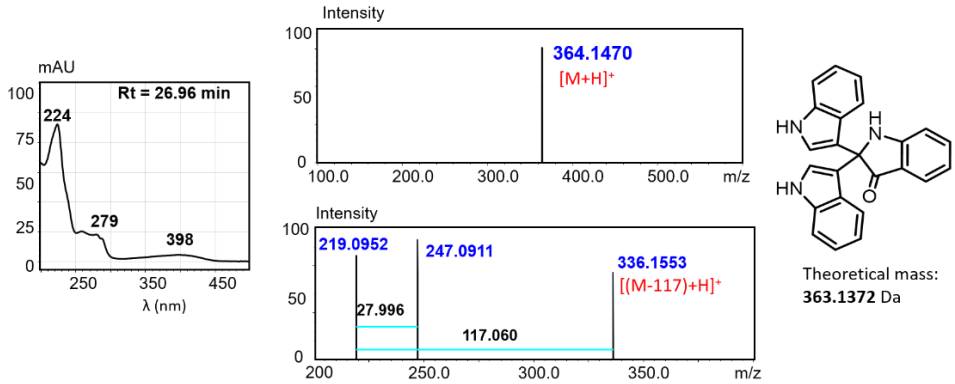

Figure 4.7. Experimental UV-Vis absorption spectrum (left side) and high-resolution MS and MS/MS spectra (right side) of indole trimeric product (Rt = 27.0 min).

Small amounts of 3-oxindolenine (Rt = 18.34 min) were also detected, along with another minor product eluted at Rt = 20.1 min. MS analysis provided identification of the latter with a dimeric species resulting from the coupling of 3-oxindolenine and indole (*m/z* = 247.086 Th, $[M+H]^+$).

The pH dependent screening of indole oxidation catalysed by Mn-MC6*a showed that both indole conversion into 3-oxindolenine and its subsequent oxidation into isatin are favoured by increasing the pH from 7.5 to 10.5. Based on these results, pH 8.5 appeared as the most suitable condition for the isolation of 3-oxindolenine with good yields. Differently from isatin and other minor products detected in the reactions, commercial standards are not available for 3-oxindolenine and easy synthetic routes are not described. For this reason, the formation and isolation of 3-oxindolenine was considered highly important. Indeed, due to the marked electrophilic character of the C2 position, this molecule could be exploited in reactions with potential synthetic interest.[52–55]

4.3. Indole oxidation catalysed by Mn-MC6*a: a mechanistic hypothesis

Mechanistic hypotheses have been formulated to explain the peculiar reactivity of Mn-MC6*a in indole oxidation.

First of all, pH dependent rate of indole oxidation suggests the involvement of Mn-Compound I as the active oxidizing species, since the formation of the latter is also pH dependent, as established earlier (see Section 2.4). As described for thioether oxidation (Section 3.2), the reaction between indole and Mn-Compound I could occur either by a direct-oxygen transfer mechanism (path a), or by a two-step pathway involving a H· radical-abstraction from the substrate (path b; Scheme 4.3).

Differently from thioether substrates, indole oxidation products have UV-Vis absorption bands in the same region of the catalyst, therefore reaction monitoring by UV-Vis spectroscopy could not be performed to clarify this aspect.

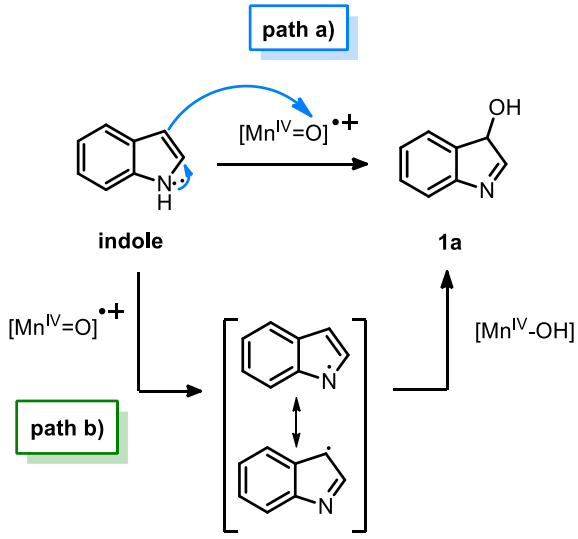

Scheme 4.3. Possible pathways for indole oxygenation promoted by Mn-MC6*a. The path a) involves a direct oxygen transfer, while the path b) consists of a two-step radical mechanism.

In the effort to provide indications of a peroxygenase mechanism, indole oxidation was performed using $H_2{}^{18}O_2$ as the oxidizing agent and only 20% of ^{18}O-incorporation was found for 3-oxindolenine. In this case, isotopic labelling studies did not provide a clear indication of the mechanism, since the poor ^{18}O-incorporation into the product could also result from a process of Lewis acid-mediated ketone acetalization (Scheme 4.4), rapidly replacing ^{18}O with the H_2O-deriving ^{16}O atom.

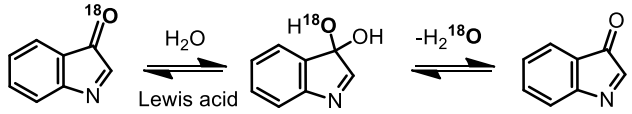

Scheme 4.4. Acetalization/deacetalization equilibrium of 3-oxindolenine.

Indole oxidation was then carried out in the presence of D-mannitol (2.0 eq. with respect to indole), which is reported to act as a radical OH scavenger.[56] A comparison between Figures 4.8 and 4.1 shows that reaction outcome was not altered in the presence of the scavenger at pH 8.5.

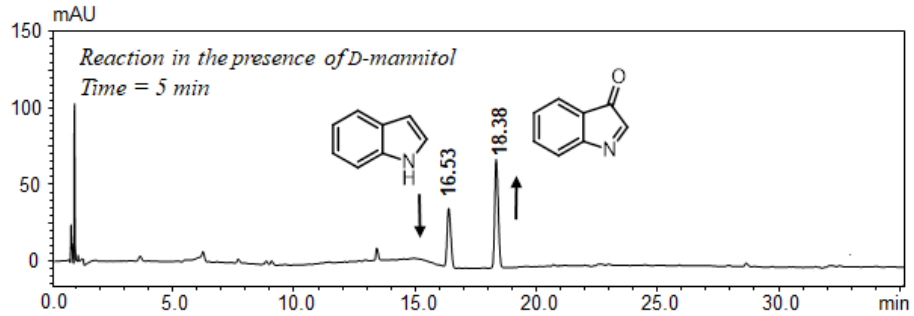

Figure 4.8. HPLC profile of indole oxidation catalysed by Mn-MC6*a at pH 8.5 in the presence of D-mannitol as radical scavenger. Trace acquired after 5 minutes by the addition of the oxidant.

Even though no strong evidences of a peroxygenase mechanism were obtained at this point, this finding suggests that the reaction is not likely to proceed through a radical mechanism.

In most of the explored experimental conditions, 3-oxindolenine was found as the primary reaction product of indole oxidation. Regardless the molecular mechanism followed in the oxygenation process, C3 oxygenation of indole by Mn-Compound I is expected to give 3-hydroxy-indolenine (species **1a**, Schemes 4.3 and 4.5). This species, in aqueous solution, is involved in an equilibrium with 3-indoxyl (**2a**) and in turn with its tautomeric form, 3-oxindole (**3a**). However, none of these species was detected under the explored experimental conditions and 3-oxindolenine was obtained instead. To explain the observed behaviour, the rapid benzylic oxidation of **1a** in the presence of ambient O_2 was proposed, which would lead to 3-oxindolenine, preventing the accumulation of species **2a** and **3a**. The subsequent formation of isatin has been rationalized as resulting from nucleophilic addition of H_2O to 3-oxindolenine, leading to 2-hydroxy-3-oxindole (**4a**, Scheme 4.5). The latter would undergo further spontaneous oxidation at the C2, yielding isatin. The hydration step would be favoured in alkaline conditions, in line with the increased selectivity towards isatin observed at pH 9.5 and 10.5.

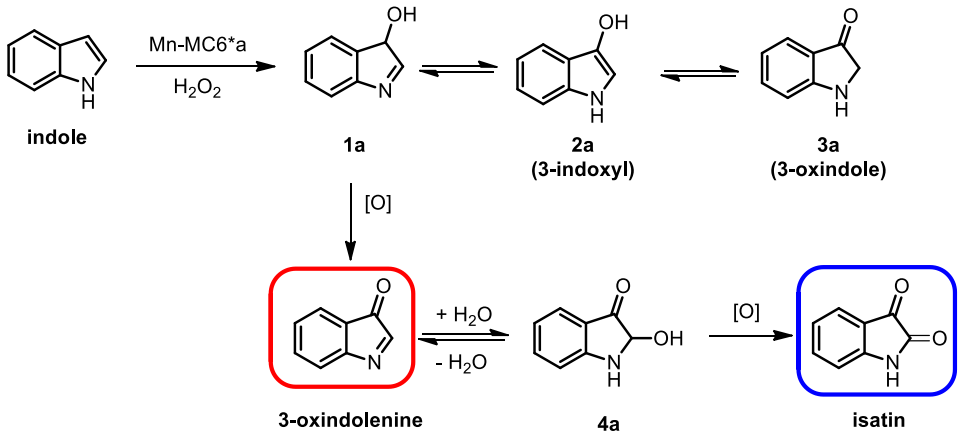

Scheme 4.5. Proposed reaction pathway for indole oxidation catalysed by Mn-MC6*a. The predominant products observed at pH 8.5 (3-oxindolenine) and at pH 9.5 (isatin) are highlighted with a red and blue circle, respectively.

Based on this assumption, dioxygen appears to play a crucial role in the formation of both 3-oxindolenine and isatin. In support of this hypothesis, indole oxidation was carried out under nitrogen atmosphere. HPLC analysis of the reaction mixture revealed that 3-oxindolenine and isatin formation are both inhibited in the absence of O_2. Indeed, only traces of 3-oxindolenine were detected after 5 minutes of reaction at pH 8.5 (Figure 4.9A). Small amounts of 3-oxindolenine and isatin were formed during the course of the reaction, possibly due to residual oxygen content in solution. Under these conditions, HPLC analysis of the reaction mixture evidenced the presence of several peaks at the end of the elution gradient. These peaks gradually increased their intensity during the reaction (Figure 4.9B) and were attributed to the formation of multiple species with high lipophilicity. The nature of these species was not clear, and an accurate characterisation was not pursued at this point.

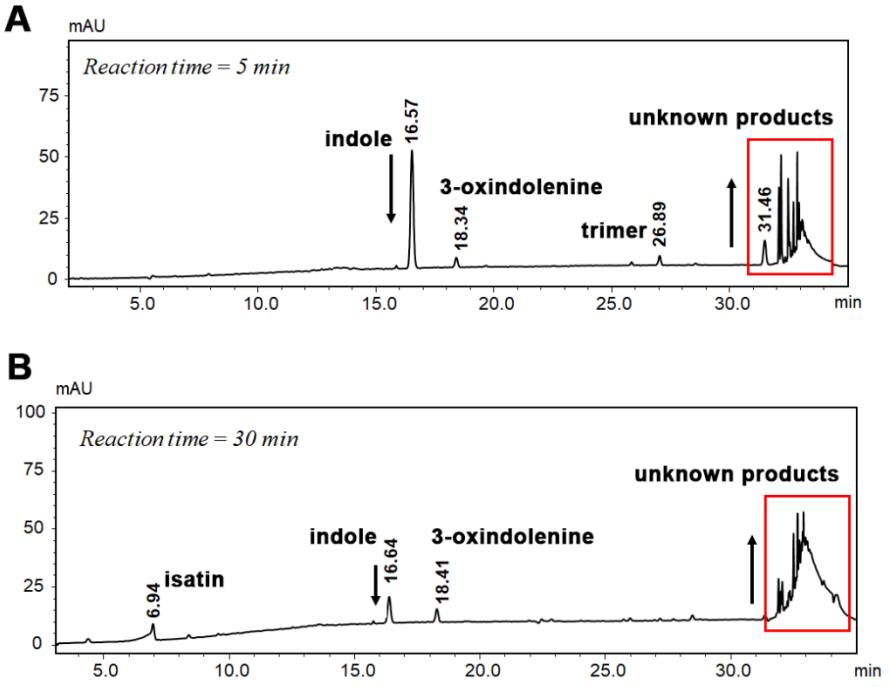

Figure 4.9. HPLC profiles of indole oxidation catalysed by Mn-MC6*a at pH 8.5 in the absence of O_2. Traces acquired after (A) 5 minutes and (B) 60 minutes.

The working hypothesis also explains the product distribution observed at pH 6.5. Formation of the trimeric compound apparently relies on the occurrence of a small amount of 3-oxindolenine along with an excess of the starting indole. Indeed, it is conceivable that the coupling reaction of indole with 3-oxindolenine could have first provided the dimeric 2-(3-indolyl)-3-oxindole (**5a**, Scheme 4.6). The fast oxidation of the latter would give 2-(3-indolyl)-3-oxindolenine (**6a**, Scheme 4.6), which was detected in small amounts during the reaction. Another coupling involving a second indole molecule would have then given the observed trimeric compound.

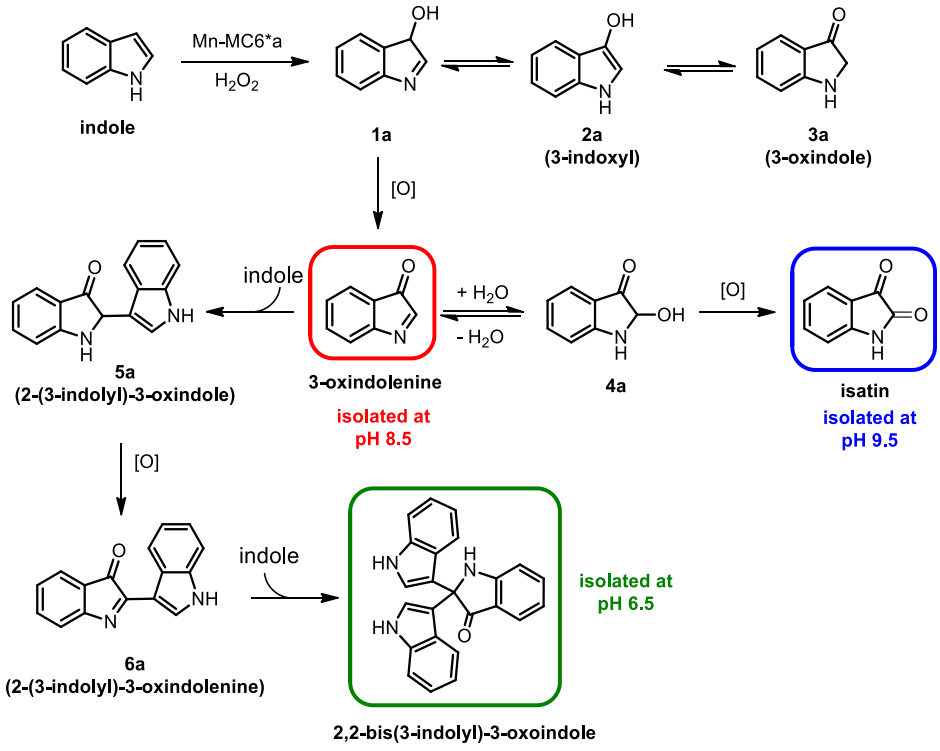

Scheme 4.6. Proposed reaction mechanism for indole oxidation catalysed by Mn-MC6*a. The major products isolated in different pH conditions are highlighted with different colours.

*4.3.1. Oxidation of methyl-substituted indoles catalysed by Mn-MC6*a*

In the effort to gain further insight into the reaction mechanism, the effect of substrate substitution was evaluated. The mechanism proposed in the previous section involves the formation of a key intermediate (3-hydroxy-indolenine, **1a**), which has been postulated to act as precursor of 3-oxindolenine. Methyl groups were introduced in specific positions of the substrate to change the reactivity of the species **1a**, consequently altering the reaction outcome. Catalytic assays were carried out in the same experimental conditions used for unsubstituted indole.

First, 3-methyl-indole was screened as substrate. The substitution at C3 was introduced to inhibit the benzylic oxidation of **1a**, which is crucial for 3-oxindolenine formation.

Mn-MC6*a catalysed the oxidation of 3-methyl-indole, leading to the formation of a different product with high selectivity (Rt = 11.4 min, Figure 4.10). This product was isolated and identified as *o*-formyl-amino-acetophenone, based on its HRMS (m/z 164.071 Th, $[M+H]^+$) and UV-Vis spectra (Figure 4.11A) which were compared with literature data.[47,48] A minor product was also observed (Rt = 25.6 min), whose HRMS spectrum (m/z 279.149 Th, $[M+H]^+$) was consistent with that of a dimeric species (Figure 4.11B).

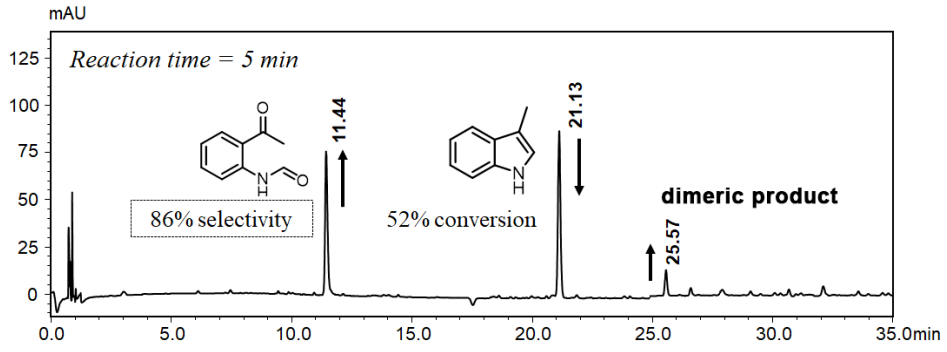

Figure 4.10. HPLC profile of 3-methyl-indole oxidation catalysed by Mn-MC6*a at pH 8.5 acquired after 5 minutes by the addition of the oxidant.

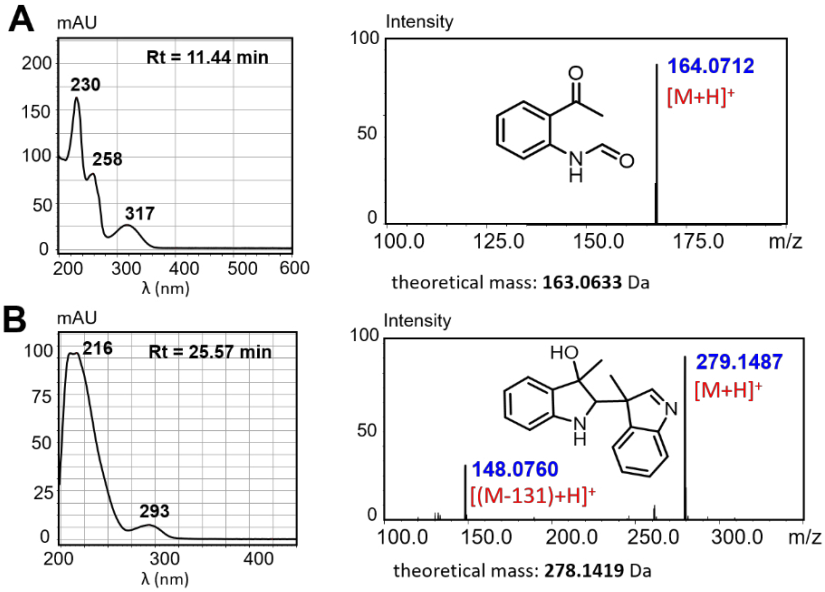

Figure 4.11. Experimental UV-Vis absorption spectra (left side) and high-resolution mass spectra (right side) of: (A) *o*-formyl-amino-acetophenone (Rt = 11.44 min); (B) the dimeric 2-(3-methyl-indolyl)-3-methyl-indolin-3-ol (Rt = 25.6 min).

Table 4.2. Substrate conversion and product distribution observed in 3-methyl-indole oxidation catalysed by Mn-MC6*a at different pH values. Data were determined by HPLC analysis of the reaction mixture after 5 minutes.

pH	Conversion (%)	*o*-formyl-amino-acetophenone (%)[a]	Others (%)[b]
7.5	20	81	19
8.5	52	86	14
9.5	82	85	15

[a] Selectivity was calculated as the ratio between the HPLC peak area of the specific product and the sum of all the peaks detected in the chromatogram (excluded the starting material).

[b] Others include all the products with exception of *o*-formyl-amino-acetophenone.

Substrate conversion monitored at 5 minutes showed the same pH dependent behaviour observed in the case of indole oxidation in terms of reaction rate (Table 4.2). However, similar selectivity (81 - 86%) towards *o*-formyl-amino-acetophenone was observed at all the screened pH values.

Formation of *o*-formyl-amino-acetophenone can be explained invoking a similar mechanistic hypothesis compared to that proposed when using indole as substrate. Indeed, C3 oxygenation would lead to 3-methyl-3-hydroxy-indolenine (**1b**, Scheme 4.7). This species cannot form 3-oxindolenine, but still retains the electrophilic character at the C2 position. Similarly to 3-oxindolenine, species **1b** can easily undergo nucleophilic addition of H_2O to C2, yielding the doubly oxygenated intermediate 3-methyl-indoline-2,3-diol (**4b**). The latter would then undergo oxidative ring opening by C-C cleavage, yielding *o*-formyl-amino-acetophenone. Conversely, the addition of a second substrate molecule to **1b** would lead to the observed dimeric product, 2-(3-methyl-indolyl)-3-methyl-indolin-3-ol.

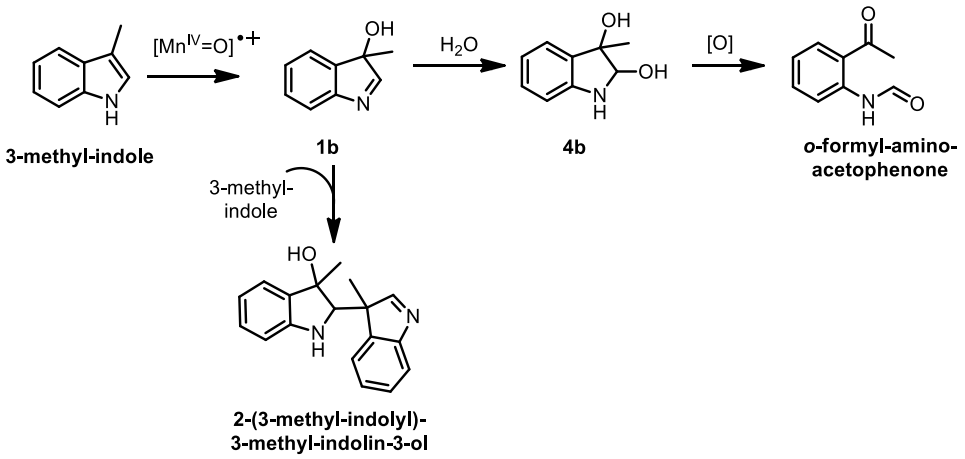

Scheme 4.7. Proposed reaction scheme of 3-methyl-indole oxidation by Mn-MC6*a.

Further, the effect of methyl group substitution on the pyrrole nitrogen was investigated. When *N*-methyl-indole was used as substrate, the reaction selectivity

was altered again, and one predominant oxidation product was observed (Figure 4.12).

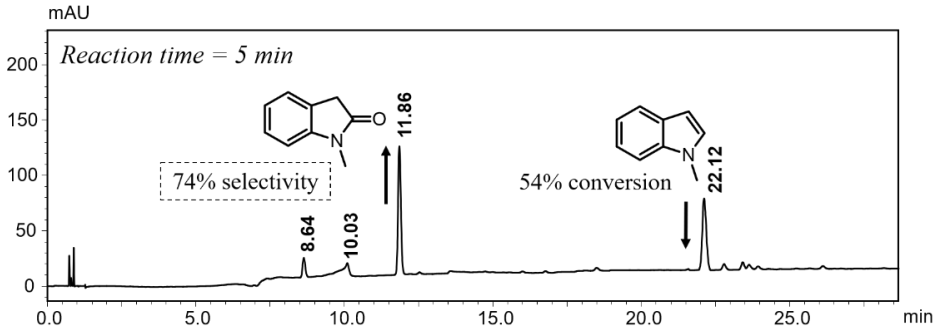

Figure 4.12. HPLC profile of *N*-methyl-indole oxidation catalysed by Mn-MC6*a at pH 8.5 acquired after 5 minutes.

MS analysis of the isolated compound (Figure 4.12) was consistent with a single oxygenation product of *N*-methyl-indole (*m/z* 148.0774, $[M+H]^+$). The UV-Vis profile of this product (Figure 4.13) was very close to that of 2-oxindole.[47,48] Unequivocal identification with *N*-methyl-2-oxindole was achieved by analysing the home-made reference compound under the same experimental conditions (see experimental section). As in the case of 3-methyl-indole oxidation, reaction selectivity towards the main product was not affected by pH (Table 4.3).

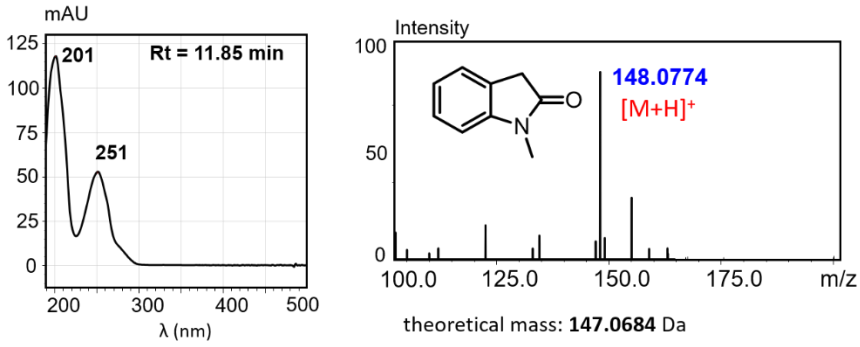

Figure 4.13. Experimental UV-Vis absorption spectrum (left side) and high-resolution mass spectrum (right side) of *N*-methyl-2-oxindole (Rt = 11.85 min).

Table 4.3. Substrate conversion and product distribution observed in *N*-methyl-indole oxidation catalysed by Mn-MC6*a at different pH values. Data were determined by HPLC analysis of the reaction mixture after 5 minutes.

pH	Conversion (%)	*N*-methyl-2-oxindole (%)[a]	Others (%)[b]
7.5	25	70	30
8.5	54	74	26

[a] Selectivity was calculated as the ratio between the HPLC peak area of the specific product and the sum of all the peaks detected in the chromatogram (excluded the starting material).
[b] Others include all the products with exception of *N*-methyl-2-oxindole.

To explain the formation of *N*-methyl-2-oxindole, the reaction would involve the formation of an epoxide intermediate (**7c**, Scheme 4.8), which is then reported to undergo an internal rearrangement,[50] yielding the observed product. One possible pathway is that described for the selective olefin epoxidation by Mn-porphyrins.[57] In such a scenario, a concerted mechanism is preferred and the intermediate resulting from C3 hydroxylation (**1c**, Scheme 4.8), would not be formed. However, the electron-donating effect of the methyl group further increases the nucleophilic character of the substrate at C3 position. Therefore, the same mechanism proposed for indole oxidation still appears the most likely to occur. In this case, the formation of *N*-methyl-3-oxindolenine is disfavoured since it would retain the positive charge of **1c**. For this reason, *N*-methyl-substitution has also the effect of enhancing the electrophilic character at C2 of the intermediate **1c** compared to **1a**. At this stage, **1c** likely undergoes intramolecular nucleophilic attack on the C2, leading to *N*-methyl-indoline-2,3-epoxide (**7c**).

In order to explore the role of the activating group, an electron-withdrawing substituent was introduced, and *N*-acetyl-indole was screened as substrate. In this case, no product formation was observed (data not shown), further indicating that

indole reactivity towards Mn-Compound I relies on the electron donation from the pyrrolic nitrogen towards C3 position.

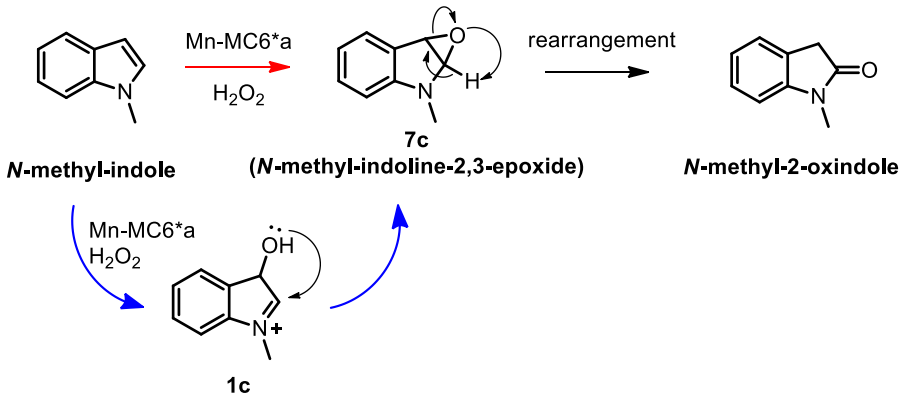

Scheme 4.8. Possible reaction pathways for *N*-methyl-2-oxindole formation promoted by Mn-MC6*a. The red arrow indicates a concerted mechanism; blue arrows indicate a two-step mechanism involving C3 hydroxylation and subsequent intramolecular reaction of the intermediate **1c**.

N-methyl-indole oxidation also provided another important clue on the reaction mechanism. Indeed, *N*-methyl-2-oxindole is not involved in an acetalization equilibrium and it is suitable for isotopic labelling studies. Experiments with $H_2{}^{18}O_2$ evidenced complete incorporation of the labelled oxygen atom into the product (Figure 4.14), thus suggesting a peroxygenase mechanism.

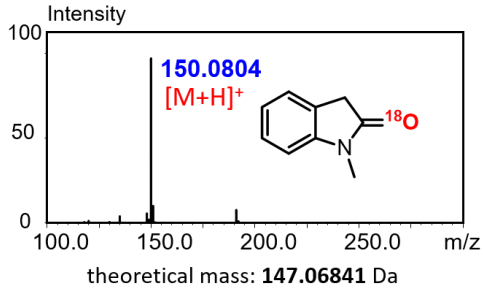

Figure 4.14. Experimental HRMS spectra of *N*-methyl-2-oxindole obtained when $H_2{}^{18}O_2$ was used in *N*-methyl-indole oxidation. Theoretical mass represents the monoisotopic mass of the product containing the most abundant isotopes of all the elements.

4.4. Indole oxidation catalysed by Fe-MC6*a

Indole oxidation was studied also with Fe-MC6*a as catalyst, using the same experimental conditions employed for Mn-MC6*a (e.g. a catalyst/substrate/H_2O_2 ratio of 1:100:100 with [Fe-MC6*a] = 10 μM and buffered solutions containing 40% TFE *v/v*). As for the Mn-analogue, reactions were carried out exploring several pH conditions.

First experiments with Fe-MC6*a were performed at pH 6.5, since it represents the best condition for peroxidase[1] and peroxygenase activity (see paragraph 3.2 of this section).[15] Unexpectedly, indole oxidation in the presence of Fe-MC6*a did not lead to significant formation of products over 5 minutes of reaction (data not shown). Long reaction times (120 min) were required to detect substrate consumption (Figure 4.15), which led to the formation of the trimeric product also observed in the assays with Mn-MC6*a at pH 6.5.

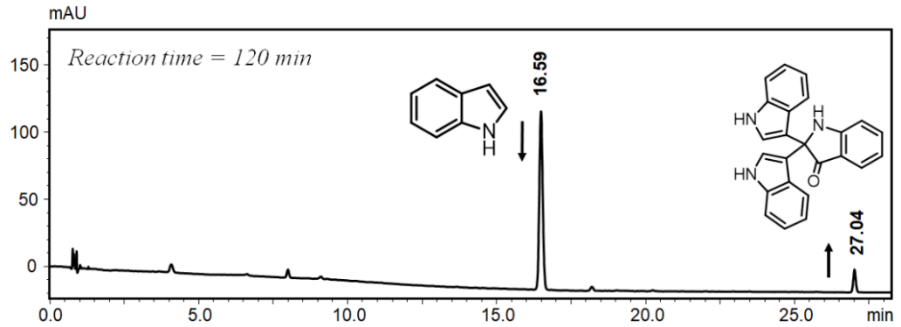

Figure 4.15. HPLC profile of indole oxidation catalysed by Fe-MC6*a at pH 6.5 acquired after 120 minutes by the addition of the oxidant. Arrows indicate changes of peak intensities during reaction. Chemical structures of indole and of the trimeric product are also shown.

For a straightforward comparison with the Mn-analogue, indole oxidation was performed at pH 8.5 with Fe-MC6*a. In these conditions, only a 20% substrate conversion was achieved within 30 minutes and 3-oxindolenine was observed as the only product (Figure 4.16).

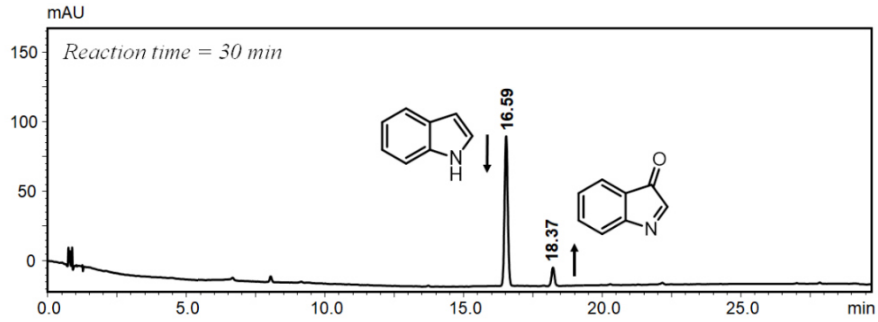

Figure 4.16. HPLC profile of indole oxidation catalysed by Fe-MC6*a at pH 8.5 acquired after 30 minutes. Arrows indicate changes of peak intensities during the course of the reaction. Chemical structures of indole and 3-oxidolenine are also shown.

These data highlight that Fe-MC6*a behaves as a less efficient catalyst with respect to Mn-MC6*a towards the oxidation of indole. This result is unexpected, considering the high reactivity demonstrated by Fe-MC6*a in promoting peroxygenase reactions.

The same product distribution was observed for both Fe- and Mn-MC6*a, suggesting that both complexes promote the formation of the same species, whose subsequent evolution is strictly dependent by pH conditions.

In order to investigate the reasons for the low reaction yields observed with the iron complex, UV-Vis studies following indole oxidation were carried out (Figure 4.17).

First, Fe-MC6*a (10 µM) was preloaded with an excess (100 eq.) of the substrate. No changes in the UV-Vis profile of the catalyst were detected, suggesting that indole does not directly coordinate to the iron ion. Addition of 2 eq. H_2O_2 suddenly led to a 20% decrease and a slight red shift of the Soret band (Figure 4.17A). No more changes in the spectrum were observed, even upon further addition of hydrogen peroxide. Another experiment was performed by first treating Fe-MC6*a with 2eq. H_2O_2. This led to a consistent (50%) decrease of the Soret band, which was attributed to the formation of the ferryl-oxo Compound I. Excess of

indole (100 eq.) was suddenly added, leading to restoring of the Soret absorbance with 70% yield (Figure 4.17B).

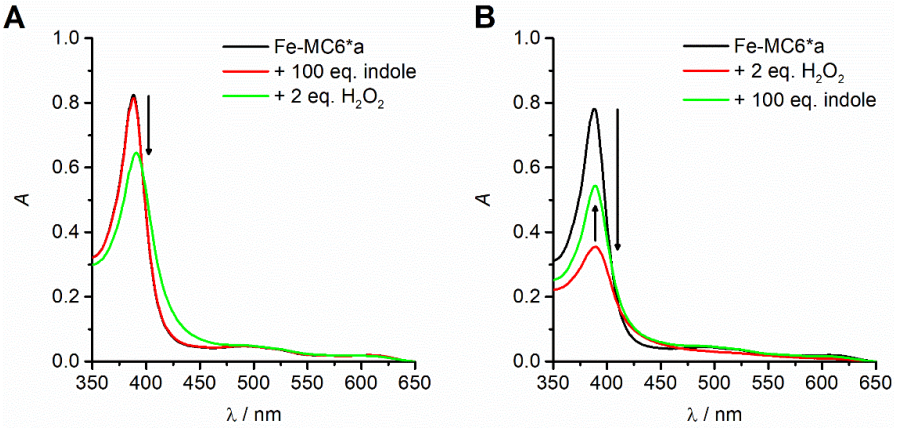

Figure 4.17. UV-Vis monitoring of indole oxidation catalysed by Fe-MC6*a at pH 6.5. (A) Spectra collected upon addition of hydrogen peroxide to the catalyst preloaded with the substrate; (B) spectra acquired upon addition of indole to pre-formed Compound I. Arrows indicate direction of absorbance changes during reaction. *Reaction conditions*: Fe-MC6*a, 10 μM; H_2O_2, 20 μM; indole 1.0 mM; 60 mM phosphate buffer with 40% TFE (*v/v*), pH 6.5.

The increase of the Soret absorbance can be ascribed to the return of the catalyst to the ferric state and the concomitant formation of the oxygenation product. Indeed 3-oxindolenine, as well as ferric MC6*a, is characterised by UV-Vis absorption at 388 nm (Figure 4.2).

UV-Vis experiments indicate that Compound I of Fe-MC6*a rapidly reacts with indole, regardless the order in which substrate and peroxide are added. A possible explanation for the low yields evidenced by HPLC analysis is the tight coordination of the oxygenation product (**1a**) to the iron ion. In this case, the dissociation of the catalyst-product complex would be rate-limiting in the catalytic turnover (Scheme 4.9).

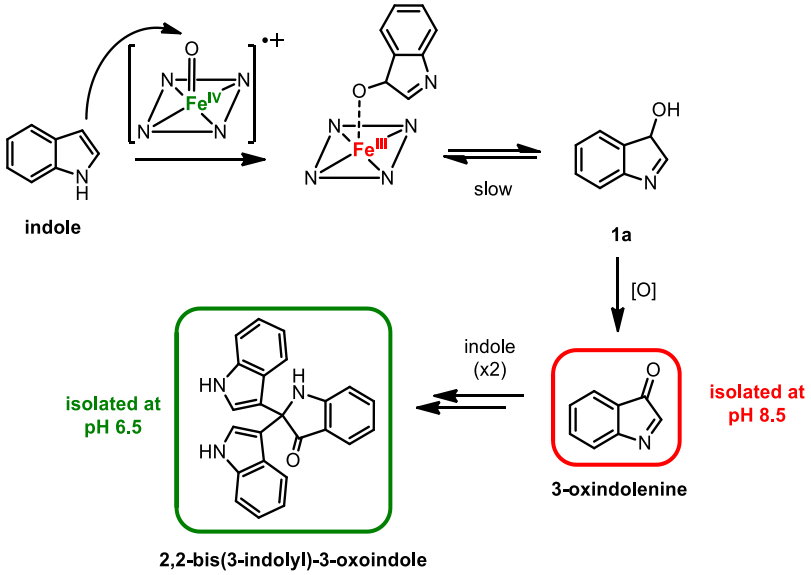

Scheme 4.9. Proposed mechanism for indole oxidation catalysed by Fe-MC6*a.

*4.4.1. Oxidation of methyl-substituted indoles by Fe-MC6*a*

The effect of indole methyl-substitution was studied also in the Fe-MC6*a catalysed reaction. When 3-methyl-indole was used as substrate, higher reaction yields were observed compared to unsubstituted indole. Indeed, 80% conversion was obtained within 5 minutes at pH 6.5 (Figure 4.18).

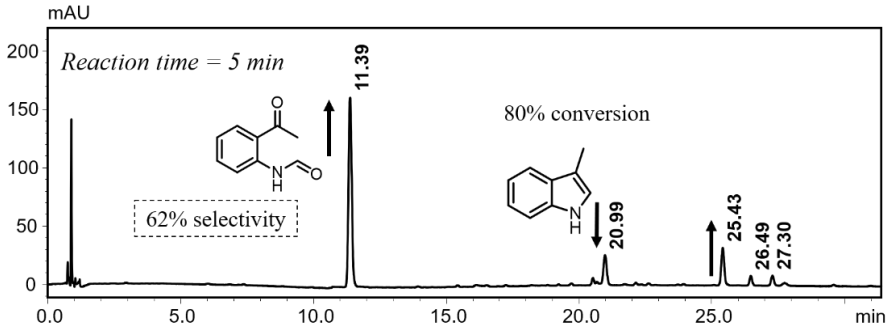

Figure 4.18. HPLC profile of 3-methyl-indole oxidation catalysed by Fe-MC6*a at pH 6.5 acquired after 5 minutes of reaction progress. Arrows indicate changes of peak intensities during reaction. Chemical structures of the substrate and the main product are also shown.

The reaction outcome, both in terms of conversion and selectivity, was not significantly affected by pH. The same products observed with Mn-MC6*a were found, even though reaction proceeded with lower selectivity towards *o*-formyl-amino-acetophenone and higher yields of the dimeric 2-(3-methyl-indolyl)-3-methyl-indolin-3-ol. The high conversion found in the oxidation of 3-methyl-indole may appear unexpected considering the low yields of indole oxidation. Whereas the coordination to the heme iron has the effect of stabilizing the intermediate **1a** disfavouring its benzylic oxidation, the formation of both the observed products of 3-methyl-indole occur through nucleophilic addition of a water or a substrate molecule to **1b** (Scheme 4.7). The tight coordination to the heme iron would further increase the electrophilic character at C2 of this species, driving the reaction towards product formation.

Oxidation of *N*-methyl-indole resulted in almost quantitative conversion of the substrate within the first 5 minutes. Differently from the highly selective Mn-MC6*a-catalysed reaction, four different products were obtained in comparable amounts (Figure 4.19).

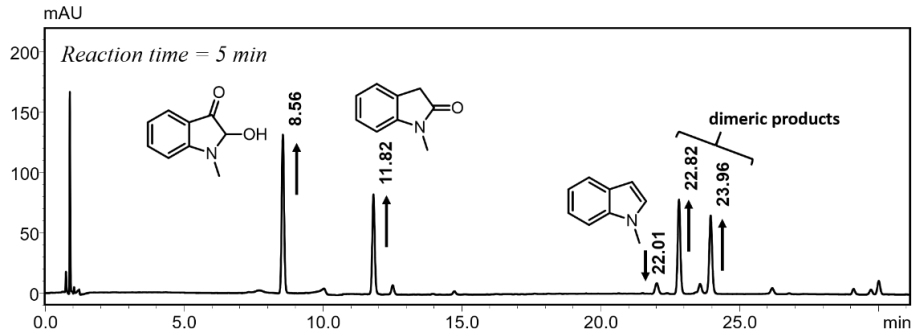

Figure 4.19. HPLC profile of *N*-methyl-indole oxidation catalysed by Fe-MC6*a at pH 6.5 acquired after 5 minutes of reaction progress. Arrows indicate changes of peak intensities during reaction. Molecular structures of the substrate and the main products are also shown.

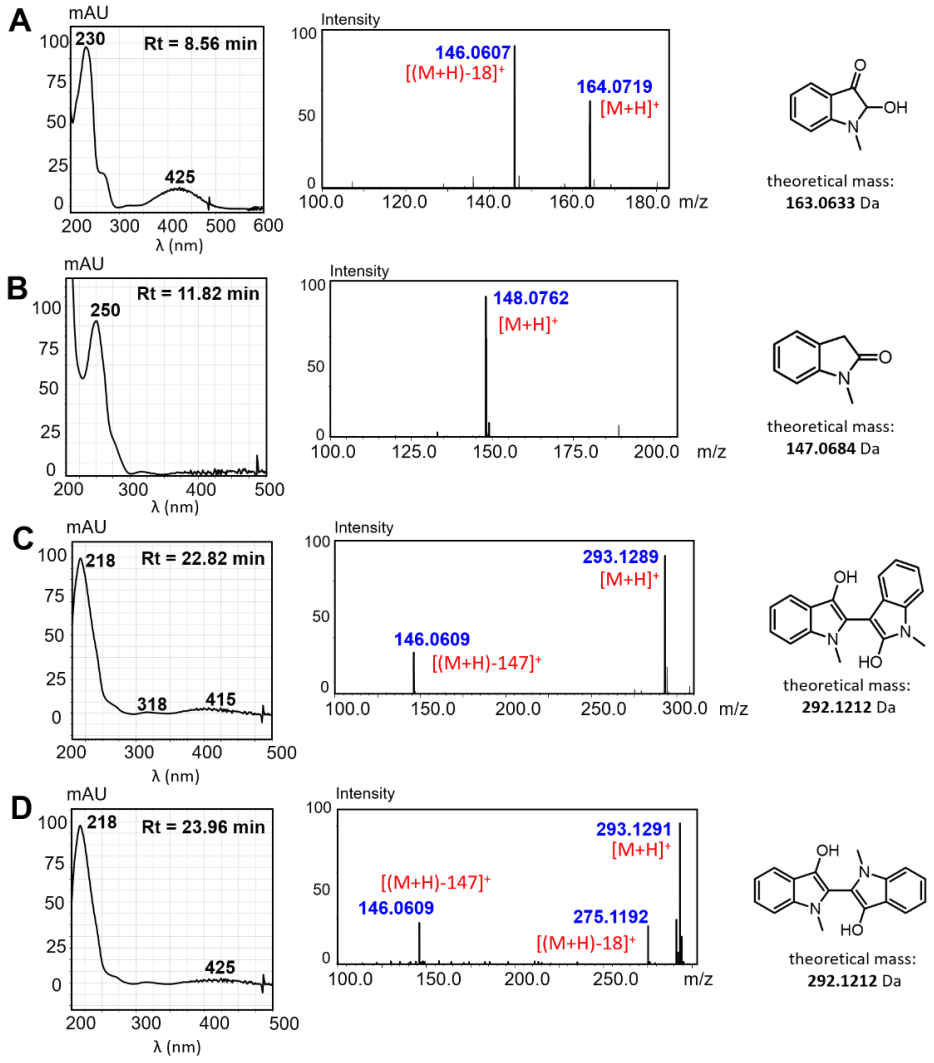

Figure 4.20. Experimental UV-Vis absorption spectra (left side) and high-resolution mass spectra (right side) of: (A) *N*-methyl-2-hydroxy-3-oxindole (Rt = 8.56 min); (B) *N*-methyl-2-oxindole (Rt = 11.82 min); (C-D) the dimeric products attributed to 1,1'-dimethyl-1*H*,1'*H*-[2,2'-biindole]-3,3'-diol and 1,1'-dimethyl-1*H*,1'*H*-[2,3'-biindole]-2',3-diol.

The most hydrophilic species among the obtained reaction products (Rt = 8.56 min) showed an UV-Vis profile which closely resembled those reported for 3-oxindole[47] (Figure 4.20A). This compound was identified as the *N*-methyl-2-

hydroxy-3-oxindole based on MS analysis. Indeed, HRMS spectrum of this product showed two peaks at *m/z* values of 164.072 Th and 146.061 Th. The latter corresponds to *N*-methyl-3-oxindoleninium ion, which could conceivably result from loss of a water molecule ($[(M+H)-18]^+$) from the former ion ($[M+H]^+$) during the ionization process.

The product eluted at Rt = 11.82 min was easily identified with *N*-methyl-2-oxindole based on its retention time, UV-Vis and HRMS spectra (Figure 4.20B) compared to those of the major product formed with Mn-MC6*a.

Both products eluted at Rt = 22.82 min and at Rt = 23.96 min showed similar UV-Vis properties and the same experimental mass (*m/z* = 293.129 Th, $[M+H]^+$). This suggests dimerization between two mono-oxygenated products of *N*-methyl-indole (Figure 4.20C-D). Owing to the presence of both C2 and C3 oxygenation products, two possible structures were proposed, but unambiguous identification of the two species was not obtained.

The low product selectivity observed in the oxidation of *N*-methyl-indole is in line with previous mechanistic hypotheses on the role of Fe-MC6*a in indole and 3-methyl-indole oxidation. Indeed, in all cases the catalyst is meant to promote substrate oxygenation at C3. Tight coordination of the resulting species (**1a**, **1b** and **1c** for indole, 3-methyl-indole and *N*-methyl-indole, respectively) accounts for the wide product distribution observed in each case. In particular, the species **1c** can evolve through at least two different pathways (Scheme 4.10).

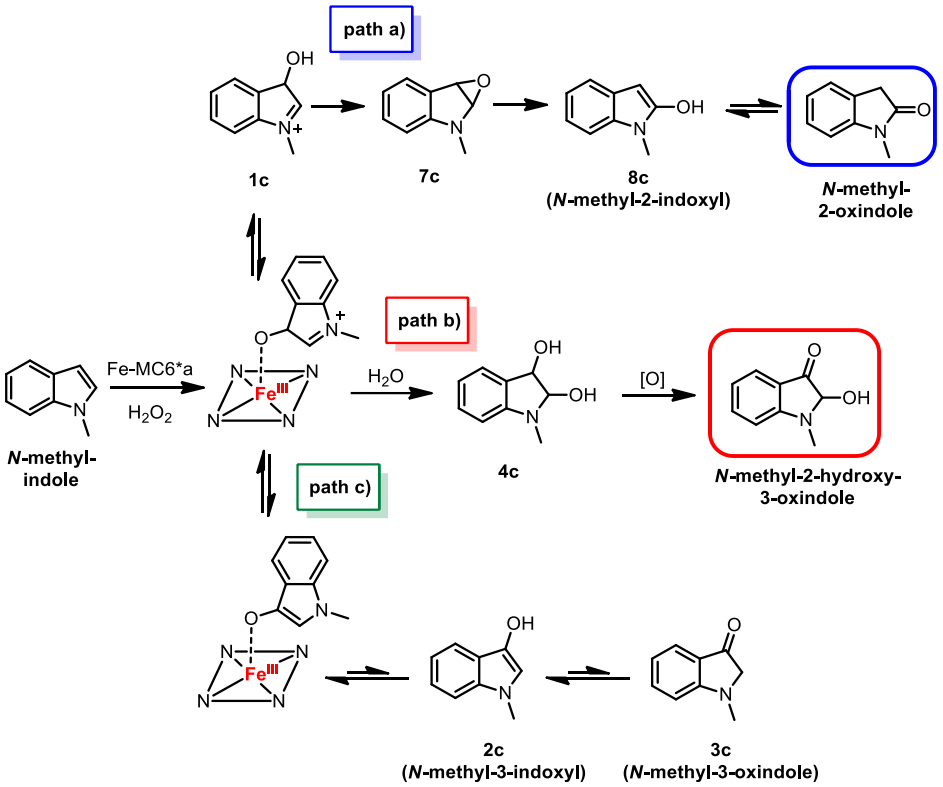

Scheme 4.10. Proposed mechanism of *N*-methyl-indole oxidation catalysed by Fe-MC6*a.

One possible pathway consists in the intramolecular nucleophilic attack, that leads to an epoxide intermediate (**7c**) and then results in *N*-methyl-2-oxindole formation (path a). Another route involves the addition of H_2O at C2, leading to *N*-methyl-2-hydroxy-3-oxindole. The former is likely to occur when the product is released in solution, while the latter is preferred if the hydroxyl group of **1c** is coordinated to the metal ion. Furthermore, metal ion coordination would also promote the tautomerization of **1c** (path c), stabilizing the enol-enamine (**2c**) with respect to the ketone (**3c**). In this frame, formation of the dimeric species conceivably results from the condensation of *N*-methyl-2-hydroxy-3-oxindole with the enolate ion of *N*-methyl-2- or 3-indoxyl (Scheme 4.11).

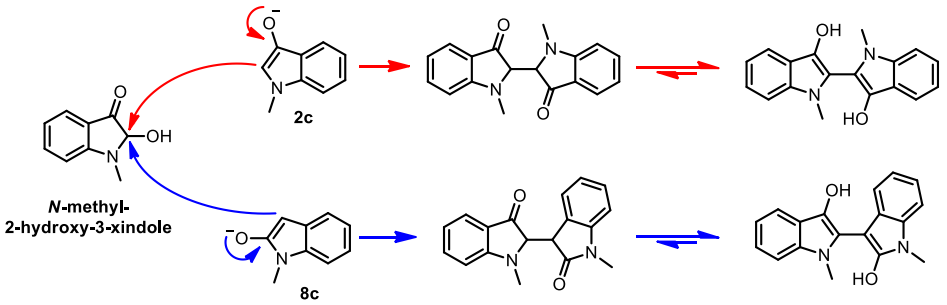

Scheme 4.11. Proposed mechanism for the formation of *N*-methyl-indole dimeric products.

Isotopic labelling studies of *N*-methyl-indole oxidation catalysed by Fe-MC6*a using $H_2{}^{18}O_2$ provided confirmation to the proposed mechanism. Interestingly, *N*-methyl-2-hydroxy-3-oxindole showed considerable incorporation of one labelled oxygen atom (Figure 4.21A; 33% *m/z* = 164.072 Th and 67% *m/z* = 166.074 Th; 60% *m/z* = 146.061 Th and 40% *m/z* = 148.065 Th). Single ^{18}O incorporation suggests that one oxygen atom is derived from Compound I and the other one from the solvent. Retaining of the ^{18}O label in the peak at $[M-18]^+$ strongly suggests the occurrence of a hydration/dehydration equilibrium. Further, the presence of significant incorporation in the C3 oxygenation product indicates that the enolic form is stabilized in solution. Indeed, unlike the ketone, the corresponding enol ether is not involved in the acetalization equilibrium that is responsible for the loss of the labelled oxygen atom.

Complete incorporation of ^{18}O was found for *N*-methyl-2-oxindole (Figure 4.21B; *m/z* = 150.081 Th, $[(M+2)+H]^+$), as already observed in the same studies when using the Mn-containing catalyst. This finding further suggests that the two catalysts react through the same peroxygenase mechanism.

Both dimeric products showed complete incorporation of two labelled oxygen atoms (Figure 4.21C-D; *m/z* = 297.137 Th, $[(M+4)+H]^+$). This result validates the hypothesis of condensation reactions between ^{18}O-containing indoxyls.

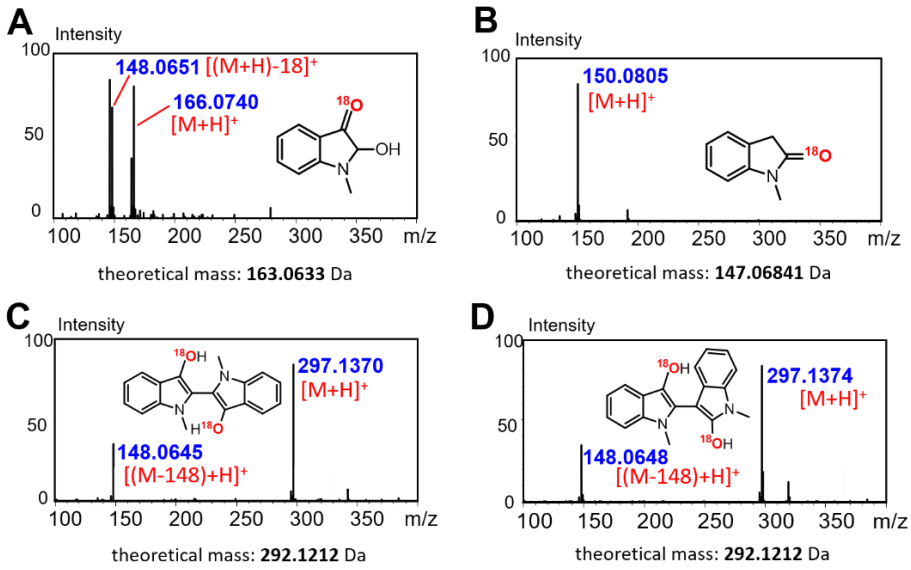

Figure 4.21. Experimental HRMS spectra of *N*-methyl-indole oxidation products obtained using Fe-MC6*a as catalyst and $H_2{}^{18}O_2$: (A) *N*-methyl-2-hydroxy-3-oxindole; (B) *N*-methyl-2-oxindole; (C) and (D) represent the spectra of the dimeric products. Theoretical mass represents the monoisotopic mass of the product containing the most abundant isotopes of all the elements.

4.5. Discussion

Oxidation of indole by heme-enzymes including chloroperoxidase (CPO),[51] P450s,[58] DHP[48] and IDO[47] is well-studied and the product distributions are different in all cases. The detailed mechanism of heme-catalysed indole oxidation has been matter of extensive investigations in the literature.[47,48,59] Chemoselectivity in indole oxidation mostly relies on the mechanism of oxygen addition to the C2–C3 double bond of the substrate. Formation of 2-oxindole likely results from an epoxidation pathway, while the route to 3-oxindole and related products (3-oxindolenine, 2-hydroxy-3-oxindole, indigo) derives from C3 hydroxylation.[50] The first mechanism appears predominant in heme-thiolate enzymes, with CPO selectively promoting the formation of 2-oxindole as the only reaction product.[51] P450s also forms 2-oxindole as the main product, but significant amounts of 6*H*-oxazolo[3,2-*a*:4,5-*b*']diindole are also obtained. The latter compound is thought to derive from the coupling of indole with 3-indoxyl radical, suggesting that both the C2 and C3 activation pathways occur in the P450-catalysed reaction.[58] Myoglobin was recently engineered to promote the formation of indigo from indole.[59,60] In the proposed mechanism, the enzyme selectively catalyses C3 hydroxylation of indole, generating 3-indoxyl, which in turn undergoes one-electron oxidation. Coupling between 3-indoxyl radicals finally leads to indigo.[59,60] IDO and DHP are characterised by an intermediate reactivity, leading to mixtures of both 2- and 3-oxygenated products in different amounts.[47,48] Radical mechanisms have been ruled out for both these enzymes, that display peroxygenase activity.[47,48]

The results herein presented highlight the ability by Mn-MC6*a to oxidize indole under unprecedented site-selective conditions. Mn-MC6*a selectively promotes substrate oxygenation at the C3 position, yielding the not commercially available 3-oxindolenine as the main product. The latter was also identified among other products in the DHP-catalysed reaction,[48] but no catalyst to date has ever been

reported to promote its formation with similar selectivity. Reaction conditions have been optimized to maximize the yields of this product, which is spontaneously converted into isatin as a consequence of its high reactivity.

Remarkably, product selectivity of Mn-MC6*a indole oxidation is altered when 3-methyl-indole or *N*-methyl-indole are used as substrates. In all cases, a predominant but different oxidation product was obtained with high selectivity. Mn-MC6*a also displays superior chemo-selectivity and efficiency compared to its Fe-analogue. Low substrate conversion was observed when Fe-MC6*a was used as catalyst in indole oxidation and the formation of several products was obtained from *N*-methyl-indole.

Based on the results obtained, a general scheme for the oxidation of indoles by Mn-MC6*a has been proposed (Scheme 4.12).

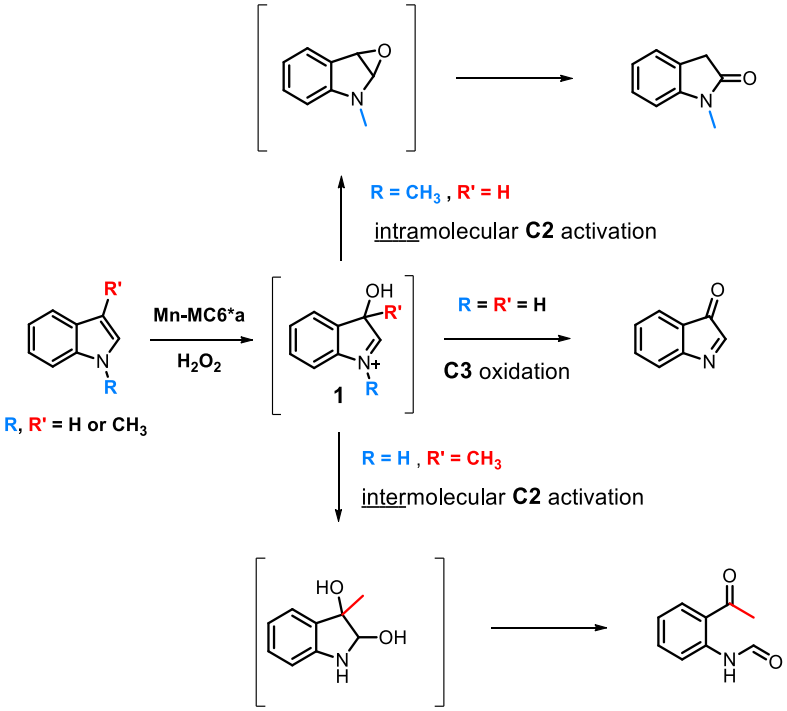

Scheme 4.12. Proposed mechanism for oxidation of indoles by Mn-MC6*a.

A common reaction mechanism involving the C3 hydroxylation by Mn-MC6*a is proposed to explain the observed reactivity. In this scenario, even the formation of *N*-methyl-2-oxindole results from the initial C3 oxygenation of the substrate. The reactivity of intermediate **1** is greatly influenced by substrate substitution, pushing the reaction towards different products.

In a comparative study between Fe- and Mn-porphyrin systems, the divergent chemo-selectivity of the catalysts was attributed to different reactive species involved in the oxygenation reaction.[50] Since (differently from literature data[50]) it is not expected that Fe- and Mn-MC6*a may react through the formation of other reactive intermediates than Fe^{IV}- or Mn^{IV}-oxo species (Compounds I), the different reaction outcomes can be rationalized simply considering the higher Lewis acidity of the Fe^{III}-porphyrin compared to the Mn^{III}-porphyrin. The higher electrophilic character of Fe^{III} compared to Mn^{III}, which is responsible for the lower pK_a of metal-bound water deprotonation and for a higher reactivity towards hydrogen peroxide also results in an enhanced affinity towards oxygenated ligands. The increased electrophilicity makes Fe-MC6*a able to provide an efficient stabilization to the oxygenated products through metal-coordination, thus altering their subsequent reactivity.

Isotopic labelling studies using $H_2{}^{18}O_2$ with *N*-methyl-indole provided an indication of peroxygenase activity with both catalysts. Further, the lack of products derived from indoxyl radicals, such as indigo or 6*H*-oxazolo[3,2-*a*:4,5-*b*']diindole, in the reactions catalysed by Mn- and Fe-MC6*a, also suggests that a radical mechanism is not likely to occur.

Compared to the other metalloporphyrin catalysts examined to the same end, Mn-MC6*a represents one of the most efficient candidates, mainly due to the possibility to control the formation of different oxidation products. Among them,

the isolation of the reactive 3-oxindolenine is highly important, because it can represent a useful synthon in organic synthesis.

The peculiar reactivity of Mn-MC6*a compared to small-molecule metallo-porphyrins and heme-proteins also suggests that the peptide scaffold could play an important role in determining reaction selectivity. Whereas metal substitution in MC6*a greatly affects the fate of the primary oxygenation product, indole oxygenation appears to proceed through the same mechanism with both the iron and the manganese complexes. Reactivity studies with the MC6*a derivative lacking the distal (*D*) peptide chain are currently under course, aimed to clarify its role in driving reaction selectivity.

5. EXPLORING REACTIVITY BEYOND OXYGENATION: CARBENE TRANSFER CHEMISTRY

5.1. Heme-mediated carbene transfer reactions

The results discussed in the previous sections outlined the ability of both Fe- and Mn-MC6*a to act as powerful catalysts in oxidation reactions. Further efforts have been devoted to expanding the range of synthetic applications of these catalysts beyond oxidation chemistry.

The interest towards the application of biocatalysts in abiotic catalysis has exponentially grown over the past few years, since several groups have reported that heme-proteins can provide abiological reactivities through the formation of heme-carbenoid intermediates.[61–63] These species are typically formed upon reaction of ferrous heme with diazo-compounds and can be considered as analogues of the native ferryl-oxo species (Scheme 5.1).

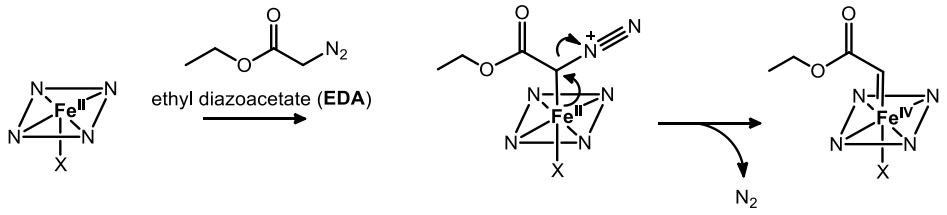

Scheme 5.1. Reaction of ferrous heme with ethyl diazoacetate (EDA) as an example of carbene precursor. X denotes protein derived axial ligand, such as cysteine or histidine.

Heme-carbenoid intermediates have been reported to promote a variety of significant transformations, including cyclopropanation,[64–66] C–H insertion,[67] S–H insertion,[68] N–H insertion,[69,70] boron alkylation[71] and C–Si bond formation.[72] All these reactions occur through carbene transfer from an electrophilic heme-carbenoid to a suitable nucleophilic substrate (Scheme 5.2), following a mechanism that resembles the oxygenation of the same substrates mediated by Compound I.

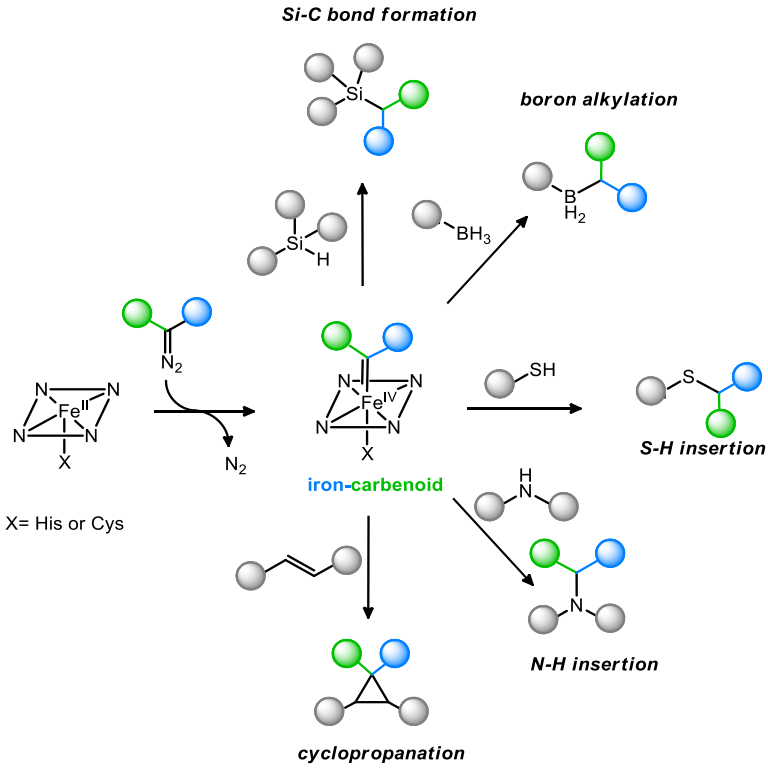

Scheme 5.2. Heme-mediated carbene transfer reactions. Grey spheres denote aliphatic and/or aromatic moieties present in the substrates, while blue and green spheres represent those derived from the carbene precursor.

P450s and myoglobin have been mostly studied for carbene transfer chemistry.[64–70] Native proteins have been carefully engineered by modulating the environment of the heme cofactor[73–75] and, in some cases, by replacing iron with different metals[76,77] with the aim of repurposing them towards abiological catalysis.

The research in this field has experienced a significant boost since the advent of directed evolution, which emerged as a powerful technique to optimize the catalytic efficiency and stereoselectivity of the artificial biocatalysts.[78–80]

Only recently, a *de novo* heme-enzyme has been demonstrated to act as an efficient and promiscuous carbene-transferase.[81] These latest achievements

prompted us to test whether the miniaturized mimochrome scaffold could be exploited to host a metallo-carbenoid species and to promote carbene-transfer reactions.

The following studies have been performed at the University of Bristol in collaboration with Dr. Ross Anderson and Prof. Emma Raven.

5.2. Metallo-carbenoid formation and reactivity assays

The ability of Fe- and Mn-MC6*a to form metallo-carbenoid species was evaluated using ethyl diazoacetate (EDA) as the carbene source. In first instance, the reactions were conducted in the same experimental conditions used by Anderson and co-workers with the *de novo* enzyme C45,[81] except for the reaction buffer, as we used 100 mM phosphate buffer (pH 6.5) and 50% *v/v* trifluoroethanol (TFE). All the assays were carried out under nitrogen inside an anaerobic glovebox ($[O_2] < 10$ ppm). In a typical experiment, the catalyst was pre-mixed with a large excess of sodium dithionite, to achieve its complete reduction. The reduced catalyst was then mixed with EDA in a stopped-flow spectrophotometer and the changes in the UV-Vis spectrum were monitored over different time periods (1-1000 s).

The first spectrum observed in the reaction of Fe-MC6*a (5 μM) with EDA (500 μM) showed a sharp Soret peak at 400 nm (Figure 5.2). Unexpectedly, this trace did not match the UV-Vis profile of Fe^{II}-MC6*a detected by spectro-electrochemistry studies. A species with a red-shifted Soret band at 412 nm, closely resembling the ferrous catalyst, was formed within the first 0.25 s of reaction. This intermediate subsequently decayed over 5 s, displaying a further red-shift to 418 nm. The latter spectra was consistent with an iron-carbenoid intermediate, since carbene adducts of diverse heme-proteins are reported to display red-shifted Soret bands.[61,81] The role of the reducing agent was also

investigated, to better understand the nature of the species detected during reaction.

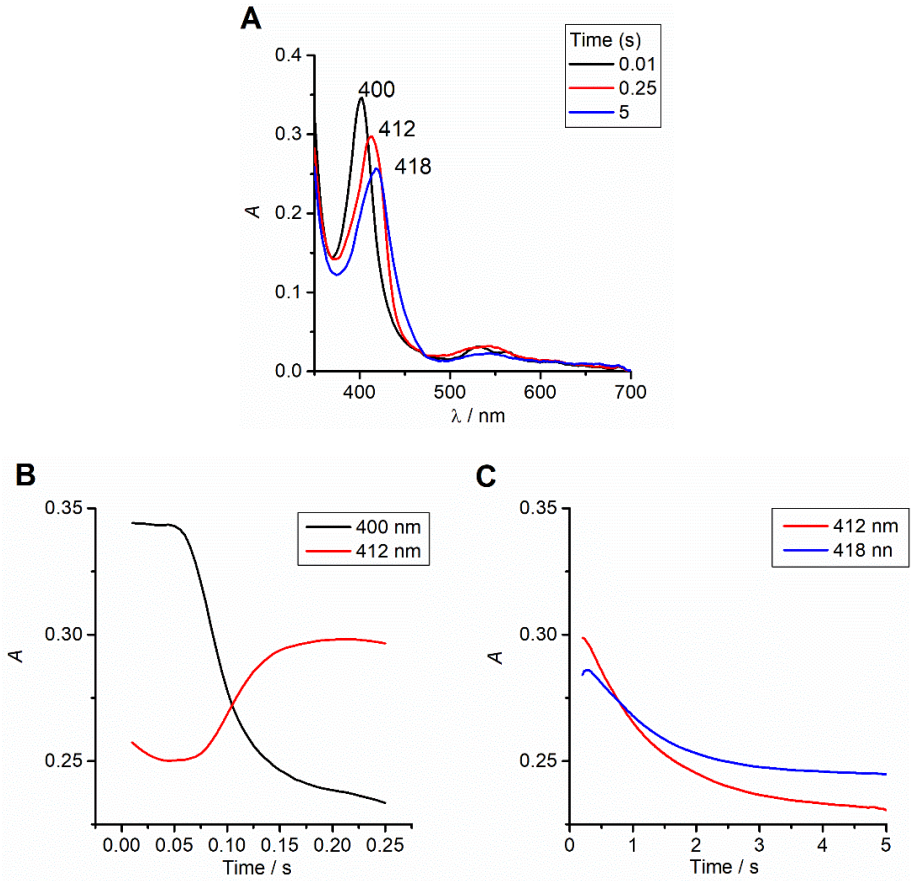

Figure 5.2. UV-Vis stopped-flow monitoring of the reaction between Fe-MC6*a (5 μM) and EDA (500 μM). Spectra collected at different reaction times (A); progress curves at selected wavelengths acquired during 0.25 s (B) or 5 s (C) of reaction.

To collect the spectrum of the dithionite reduced catalyst, a solution of Fe^{II}-MC6*a (10 μM, pre-treated with an excess of sodium dithionite), was anaerobically mixed with a solution of sodium dithionite in the stopped-flow spectrophotometer. In this case, a Soret band centred at 418 nm was observed (Figure 5.3, blue line), which is slightly red-shifted with respect to the

electrochemically reduced catalyst (Figure 5.3, red line). This difference was ascribed to the coordination of sulphite to ferrous heme upon dithionite reduction, that was confirmed by spectro-electrochemical analysis of the catalyst in the presence of 100 eq. sodium sulphite (Figure 5.3, black line).

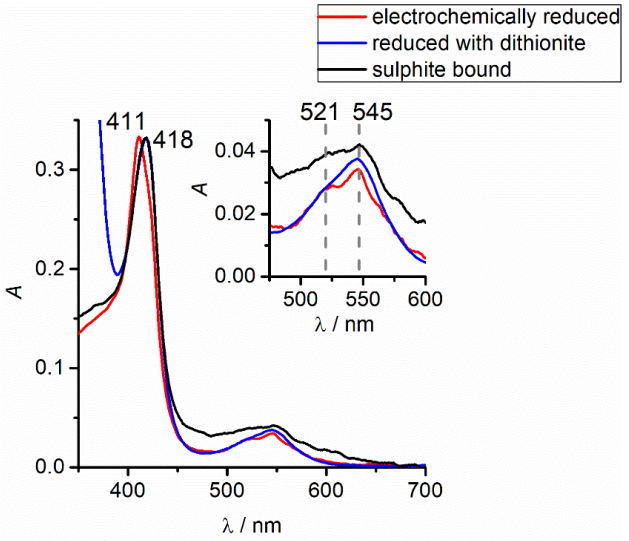

Figure 5.3. Comparison of the UV-Vis spectra of Fe^{II}-MC6*a obtained by: chemical reduction with sodium dithionite (blue trace); electrochemical reduction in the absence (red trace) and in the presence (black trace) of sodium sulphite.

The absorption spectrum of sulphite-bound Fe^{II}-MC6*a also resembled that of the final species detected in iron-carbenoid formation assays. Therefore, in the effort to provide experimental evidences of the iron-carbenoid formation, the reaction of Fe-MC6*a with EDA was also examined using electrospray ionization (ESI) mass spectrometry (MS). Comparison of the mass spectra of Fe-MC6*a acquired before and after addition of EDA evidenced a mass difference of 86.1 Da, corresponding to the carbene fragment (Figure 5.4).

This result confirmed the formation of a carbene adduct. The mass spectrum remained unchanged over at least 30 minutes. The high stability of such species

suggested that covalent modification of the catalyst occurred in the absence of an external nucleophilic substrate, as reported by Renata et al.[82]

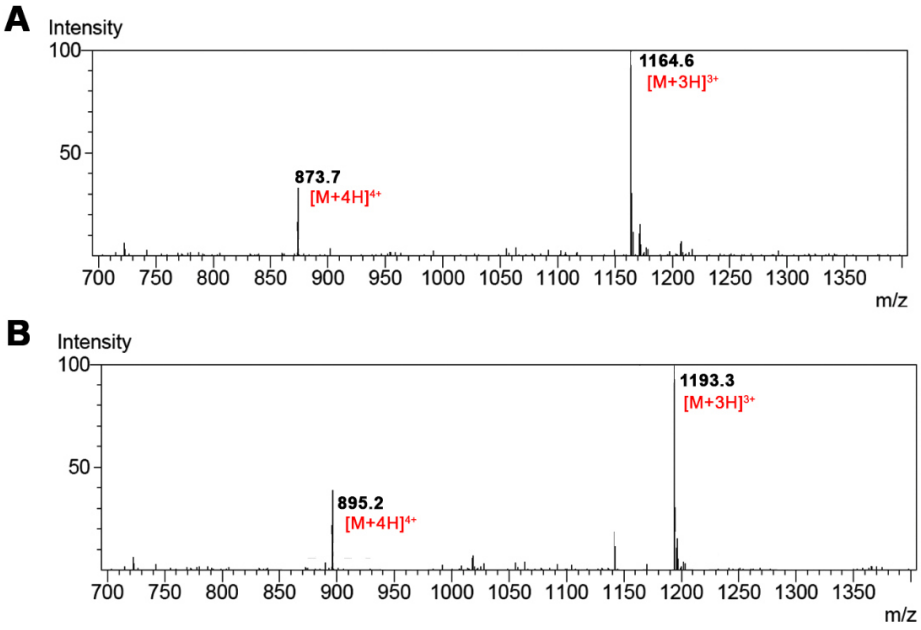

Figure 5.4. ESI-MS spectra of Fe-MC6*a acquired before (A) and after (B) the reaction with EDA.

The ability of Fe-MC6*a to promote carbene-transfer reactions was then examined by using styrene as model substrate for cyclopropanation. In the first screening, the catalyst (10 μM) was reduced with sodium dithionite and preloaded with the substrate (30 mM). Reaction was initialized by anaerobic addition of the carbene precursor (10 mM) and kept anaerobically under stirring at room temperature for 2 hours. Unfortunately, no reaction product was observed by HPLC analysis (data not shown).

The effect of various reaction parameters was investigated in order to favour substrate functionalization with respect to catalyst self-inactivation. In particular, a higher catalyst loading (from 0.1% to 1%) and a higher excess of the

nucleophilic substrate with respect to the carbene source (from 3- to 10-fold) were employed. However, no progress of the reaction was observed in all cases. Further attempts were carried out at low temperature (T = 5°C) or by gradual addition of EDA (20 eq. every 5 minutes until 100 eq.). The use of bulkier carbene precursors than EDA, i.e. benzyl-diazoacetate (BnDA) and *tert*-butyl-diazoacetate (*t*-BuDA), was also evaluated, since it was thought to disfavour an intra-molecular nucleophilic attack in the carbene adduct. Piperidine was chosen as the acceptor substrate for carbene N-H insertion, due to its higher nucleophilic character compared to styrene. However, no carbene-transfer activity was detected in all the explored conditions.

The same experiments were performed also with Mn-MC6*a for comparative analysis. In the stopped-flow studies of the reaction between Mn-MC6*a (5 µM) and EDA (500 µM), the transient formation of a weak absorption band at 459 nm was detected in the first 0.2 seconds, then it decayed back to the initial spectrum (Figure 5.5).

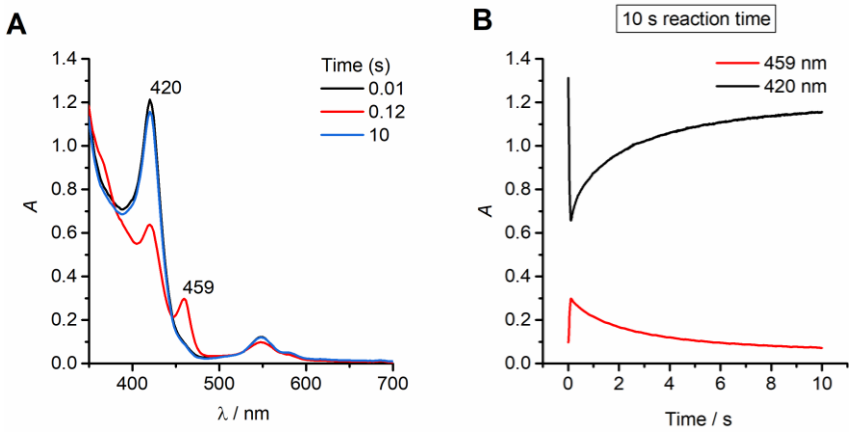

Figure 5.5. UV-vis stopped flow monitoring of the reaction between Mn-MC6*a and EDA. Spectra collected at different reaction times (A); progress curves at selected wavelengths acquired during 10 s of reaction (B).

The band at 459 nm was attributed to the partial oxidation of the catalyst to the Mn^{III} state by residual oxygen. The lower wavelength Soret peak at 365 nm could

not be clearly observed due to the strong absorption of dithionite in the same spectral region.

The emergence of the oxidized catalyst suggested that residual oxygen could also have a role in the assays with Fe-MC6*a. Oxygen binding studies were subsequently performed with both catalysts in search for experimental indications of this hypothesis.

5.3. Oxygen-binding studies

The ability of Fe^{II}- and Mn^{II}-MC6*a to bind O_2 was investigated by performing stopped-flow experiments with oxygen-purged buffer solutions.

The experiments were performed at T = 5°C since the binding kinetics was expected to be very fast. In first instance, reactions were carried out in 100 mM phosphate buffer pH 6.5 in the absence of TFE, due to the low solubility of phosphate in the mixed solvent at low temperature.

The reaction between Fe^{II}-MC6*a (5 µM) and O_2-saturated buffer ([O_2] ~ 600 µM, based on the solubility of O_2 in H_2O of 1.2 mM[83]) led to the immediate formation of a species with Soret absorption maximum at 399 nm and Q bands at 530 and 563 nm (Figure 5.6A). This UV-Vis profile closely resembled that of the starting species observed in metallo-carbenoid formation assays. The slight wavelength shift could be attributed to the presence of TFE and ethanol in those experiments. Such species was identified with the oxy-ferrous complex by comparison with literature data on horseradish peroxidase[13] and C45 *de novo* enzyme.[84]

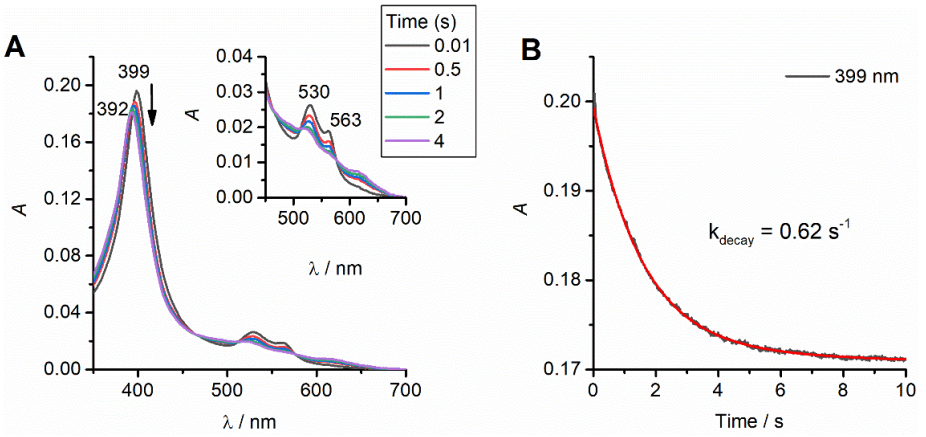

Figure 5.6. UV-Vis stopped flow monitoring of the reaction between Fe^{II}-MC6*a (5 µM) and O_2 (600 µM) in 50 mM phosphate buffer pH 6.5, T = 5°C. (A) Spectra collected during the reaction course; (B) progress curve at 399 nm fitted to a single exponential model.

The ferrous-oxy species spontaneously decayed to ferric (392 nm) within 10 s as result of an autoxidation process without any detectable intermediate. The kinetics of decay was measured by plotting the absorbance at 399 nm against time. Data were fitted to a single exponential model and an apparent first-order rate constant of 0.62 s^{-1} was observed (Figure 5.6B). The observed value is extremely close to that reported for R38G mutant of horseradish peroxidase (k_{decay} = 0.58 s^{-1}), which also exhibited a 100-fold higher rate constant for the ferrous-oxy complex formation compared to the native enzyme (R38G HRPC: k_{on} = 3.0 ·10^6 M^{-1} s^{-1}; HRPC: k_{on} = 5.3 ·10^4 M^{-1} s^{-1}).[13]

Control experiments were performed by mixing Fe^{II}-MC6*a with a buffer solution allowed to equilibrate with N_2-atmosphere overnight into the glovebox. In these conditions, ferrous MC6*a spontaneously reverted to ferric, even though the oxy-ferrous species could not be clearly detected (Figure 5.7).

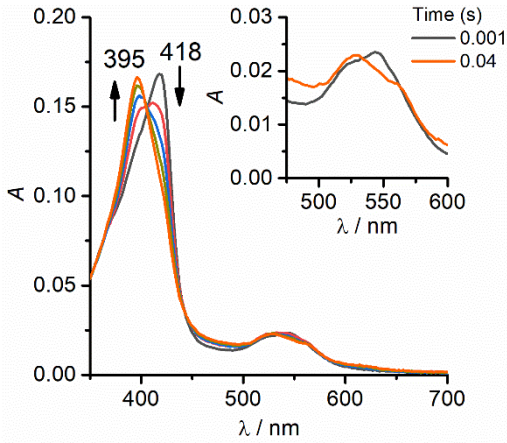

Figure 5.7: UV-Vis stopped flow monitoring upon mixing of Fe-MC6*a (5 µM) with degassed buffer solution. Spectra collected every 10 ms. The inset shows a focus on the Q bands in the spectra acquired after 1 and 40 ms.

This finding suggested that Fe^{II}-MC6*a is very sensitive towards O_2, since only trace amounts of the gas might be present in the nitrogen equilibrated buffer. To clarify the role of dioxygen in this process, glucose oxidase (GOx, 20 µg/mL) and D-glucose (10 mM) were added to the buffer solution to ensure the complete removal of dissolved oxygen. Catalase (2 µg/mL) was also added to remove hydrogen peroxide produced by the GOx-catalysed reaction. In this case, the ferrous form remained stable over at least 60 s (data not shown).

With the aim of following the binding process, experiments were carried out at lower O_2 concentrations (60 µM and 6 µM). Only at 6 µM O_2 an increase of the absorbance at 399 nm was observed in the first 8 ms after mixing (Figure 5.8).

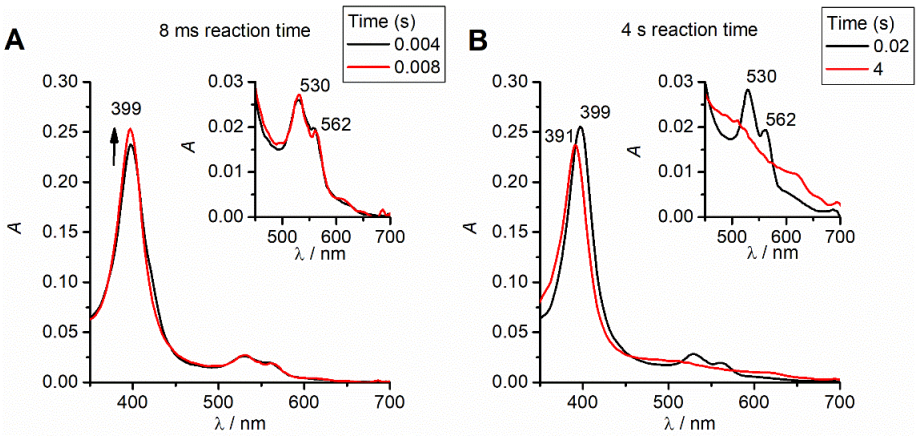

Figure 5.8: UV-Vis stopped flow monitoring of the reaction between Fe-MC6*a (5 µM) and O_2 (6 µM) in 50 mM phosphate buffer pH 6.5, T = 5°C. Spectra collected during (A) 8 ms and (B) 4 s of reaction.

Table 5.1. Apparent first order rate constants of oxy-ferrous MC6*a autoxidation at different O_2 concentrations. [Fe^{II}-MC6*a] = 5 µM; 50mM phosphate buffer pH 6.5. T = 5°C.

$[O_2]$ (µM)[a]	**k_{decay} (s^{-1})[b]**
600	6.2
60	5.9
6	6.7

[a] $[O_2]$ was estimated based on O_2 solubility and by dilution of O_2-saturated buffers with degassed buffers.
[b] k_{decay} was obtained by a single exponential fit of the experimental single-wavelength progress curves.

In all cases, the autoxidation process followed an apparent first-order kinetics and the rate constant was nearly independent from O_2 concentration (Table 5.1). The binding kinetics was too fast for an accurate determination of the rate constants in the explored experimental conditions.

UV-Vis stopped flow monitoring of the reaction between Mn^{II}-MC6*a and O_2-containing buffer solutions (50 mM phosphate, pH 6.5) evidenced the rapid and direct conversion of the catalyst to the Mn^{III} state (Figure 5.9).

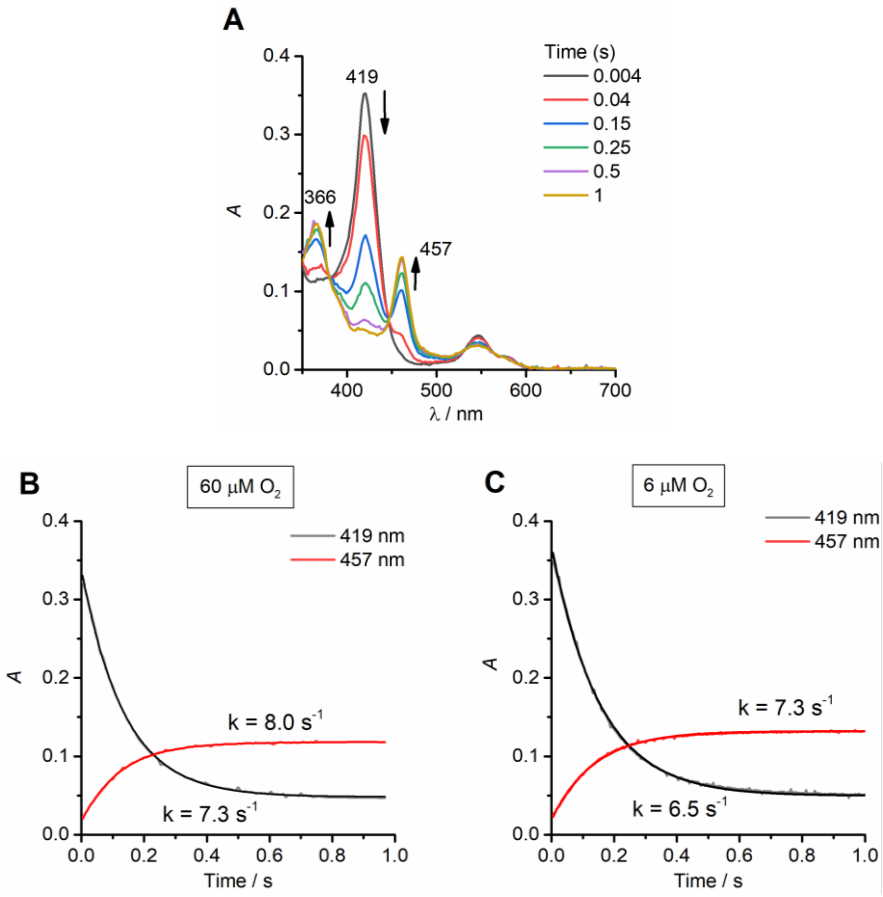

Figure 5.9: (A) Spectra acquired during reaction between Mn^{II}-MC6*a (5 μM) and O_2 (60 μM) in 50 mM phosphate buffer pH 6.5, T = 5°C. Progress curves at 419 nm and 457 nm relative to experiments with (B) 60 μM and (C) 6 μM O_2.

The lack of spectroscopically detectable intermediates in the process indicates that Mn^{II}-MC6*a, differently to Fe^{II}-MC6*a, is not able to tightly bind O_2.

5.4. Discussion

The ability of Fe^{II} and Mn^{II}-MC6*a to form metallo-carbenoid species upon reaction with diazo-compounds has been evaluated. Whereas the Mn-complex did not display any reactivity towards carbene precursors, the formation of a carbene adduct of Fe-MC6*a was ascertained by MS analysis. This species was characterized by a high-chemical stability, that prevented any carbene-transfer reactivity towards external nucleophilic substrates such as aromatic alkenes and amines.

Carbene precursors were reported to act as mechanism-based inhibitors of P450s since before the exploitation of heme-carbenoid species in catalysis. In such mechanisms, an iron-carbenoid intermediate is generated along the metabolism of an inactivator molecule and covalently reacts with an active site amino-acid residue and/or alkylates the porphyrin, resulting in the irreversible heme degradation.[85,86] Suicide inactivation of P450s in the presence of CCl_4 was also proposed to involve a carbenoid species.[87] Recently, the group of prof. Arnold investigated the mechanism of P450s inactivation upon reaction with diazo-compounds, with the aim of circumventing such pathways by protein engineering.[82]

It is worth to note that most of the enzymes reported to act as carbene-transferases have been obtained by engineering of native proteins and/or have been exposed to several rounds of directed evolution. Therefore, it is not surprising that the miniaturized mimochrome scaffold, which was designed to act as oxidative heme-enzymes, needs further optimization to provide productive carbene transfer catalysis.

UV-Vis stopped-flow experiments evidenced that ferrous MC6*a forms a spectroscopically detectable ferrous-oxy species, even upon mixing with N_2-flushed solutions. By contrast, Mn^{II}-MC6*a is not able to tightly bind dioxygen.

A preliminary kinetic study of the reaction between Fe^{II}-MC6*a and O_2 highlighted that dioxygen binding is very fast, occurring suddenly upon mixing (~ 40 ms).

The characterization of MC6*a ferrous-oxy complex, concerning the kinetics of its formation and its stability could provide the basis for the exploitation of the catalyst in the construction of dissolved oxygen sensors.

6. CONCLUDING REMARKS

The research activity carried out in the frame of this PhD project has been focused on studying the reactivity of synthetic heme-enzymes, with a focus on oxidative catalysis. In particular, the Fe- and the Mn-derivatives of Mimochrome VI*a (MC6*a) have been screened for oxygen-transfer reactions.

Mimochromes, which represent a class of miniaturized heme-proteins, were designed and optimized to promote the oxidation of peroxidases' model substrates.[1,88,89] This kind of catalysis could be useful for sensing and diagnostic applications.[90,91]

The primary aim of this PhD project was to extend the possible applications of mimochromes to synthetic chemistry. Taking into account the versatility of metallo-porphyrins in promoting diverse oxidative transformations, the Mn-derivative of MC6*a was prepared. Then, the analysis of the spectroscopic, redox and catalytic properties of Fe- and Mn-MC6*a was performed.

Compared to other peptide-porphyrin conjugates with a fully solvent-exposed distal site, both Fe- and Mn-MC6*a display an increased ability to promote the deprotonation of metal-bound water. This property was ascribed to the interaction between the metalloporphyrin and the distal peptide chain, that also leads to less negative reduction potentials for the Fe^{III}/Fe^{II} and Mn^{III}/Mn^{II} couples. The hydrophobic environment on the distal site results in a high stabilization of the species characterized by a lower charge density, such as the water-bound reduced form and the hydroxy-bound oxidized form. This property enables MC6*a complexes to reach their highest activity towards H_2O_2 at lower pH values, approaching more closely the natural counterparts.

The high-valent Fe^{IV}- or Mn^{IV}-oxo species formed upon reaction with hydrogen peroxide were efficiently exploited in the oxygenation of reducing substrates.

Both Fe- and Mn-MC6*a demonstrated to be highly active and robust catalysts in the H_2O_2-mediated sulfoxidation of thioethers, being among the most efficient artificial heme-enzymes studied for this reaction. The analysis of indole oxidation instead highlighted a divergent behaviour of the two catalysts, which was ascribed to the different electronic properties of the metal ions. Notably, Mn-MC6*a displays higher chemo-selectivity compared to Fe-MC6*a and also surpasses most heme-enzymes studied for the same reaction. Mn-MC6*a represents one of the most proficient catalysts for indole oxidation, mainly due to the possibility of controlling reaction regio-selectivity depending on substrate substitution. In this context, the high yielding and selective conversion of starting indole into 3-oxindolenine is a very important result, because of the unavailability of this product from other sources. Its high reactivity could be exploited for the construction of more complex molecules of synthetic interest.

Overall, the results reported in this PhD thesis pave the way for the application of mimochromes in synthetic chemistry. The simple structure of this artificial system holds some typical features of small-molecule metallo-porphyrin catalysts, such as an accessible distal site that enables substrate promiscuity. It also displays enzyme-like properties, owing to a rationally designed peptide scaffold, that allows for the modulation of redox properties of the metal ion. Future work will be devoted to increase the complexity of the environment around the metal centre, with the aim of further improving the catalytic performances of this system and to expand the scope of transformations accessible by mimochrome complexes.

7. REFERENCES

1. Caserta, G., Chino, M., Firpo, V., Zambrano, G., Leone, L., D'Alonzo, D., Nastri, F., Maglio, O., Pavone, V. & Lombardi, A. Enhancement of Peroxidase Activity in Artificial Mimochrome VI Catalysts through Rational Design. *ChemBioChem* **19,** 1823–1826 (2018).
2. Buchler, J. W. 10 - Synthesis and Properties of Metalloporphyrins. in *The Porphyrins* (ed. Dolphin, D.) 389–483 (Academic Press, 1978).
3. Giovannetti, R., Alibabaei, L. & Pucciarelli, F. Spectral and kinetic investigation on oxidation and reduction of water soluble porphyrin–manganese(III) complex. *Inorg. Chim. Acta* **363,** 1561–1567 (2010).
4. Firpo, V. Functional Characterization of Synthetic Metalloporphyrin-Containing Enzymes. Ph.D. Thesis in Chemical Sciences - XXX Cycle (Università degli Studi di Napoli Federico II, 2018).
5. Vitale, R., Lista, L., Cerrone, C., Caserta, G., Chino, M., Maglio, O., Nastri, F., Pavone, V. & Lombardi, A. An artificial heme-enzyme with enhanced catalytic activity: evolution, functional screening and structural characterization. *Org. Biomol. Chem.* **13,** 4859–4868 (2015).
6. Hong, D.-P., Hoshino, M., Kuboi, R. & Goto, Y. Clustering of Fluorine-Substituted Alcohols as a Factor Responsible for Their Marked Effects on Proteins and Peptides. *J. Am. Chem. Soc.* **121,** 8427–8433 (1999).
7. Whitmore, L. & Wallace, B. A. Protein secondary structure analyses from circular dichroism spectroscopy: Methods and reference databases. *Biopolymers* **89,** 392–400 (2008).
8. Low, D. W., Abedin, S., Yang, G., Winkler, J. R. & Gray, H. B. Manganese Microperoxidase-8. *Inorg. Chem.* **37,** 1841–1843 (1998).
9. Vitale, R., Lista, L., Lau-Truong, S., Tucker, R. T., Brett, M. J., Limoges, B., Pavone, V., Lombardi, A. & Balland, V. Spectroelectrochemistry of FeIII- and CoIII-mimochrome VI artificial enzymes immobilized on mesoporous ITO electrodes. *Chem. Commun.* **50,** 1894–1896 (2014).
10. Marritt, S. J., Kemp, G. L., Xiaoe, L., Durrant, J. R., Cheesman, M. R. & Butt, J. N. Spectroelectrochemical Characterization of a Pentaheme Cytochrome in Solution and as Electrocatalytically Active Films on Nanocrystalline Metal-Oxide Electrodes. *J. Am. Chem. Soc.* **130,** 8588–8589 (2008).
11. Renault, C., Andrieux, C. P., Tucker, R. T., Brett, M. J., Balland, V. & Limoges, B. Unraveling the Mechanism of Catalytic Reduction of O2 by Microperoxidase-11 Adsorbed within a Transparent 3D-Nanoporous ITO Film. *J. Am. Chem. Soc.* **134,** 6834–6845 (2012).
12. Risbridger, T. A. G., Watkins, D. W., Armstrong, J. P. K., Perriman, A. W., Anderson, J. L. R. & Fermin, D. J. Effect of Bioconjugation on the Reduction Potential of Heme-proteins. *Biomacromolecules* **17,** 3485–3492 (2016).

13. Rodriguez-Lopez, J. N., Smith, A. T. & Thorneley, R. N. F. Effect of Distal Cavity Mutations on the Binding and Activation of Oxygen by Ferrous Horseradish Peroxidase. *J. Biol. Chem.* **272,** 389–395 (1997).
14. Efimov, I., Parkin, G., Millett, E. S., Glenday, J., Chan, C. K., Weedon, H., Randhawa, H., Basran, J. & Raven, E. L. A simple method for the determination of reduction potentials in heme-proteins. *FEBS Lett.* **588,** 701–704 (2014).
15. Leone, L., D'Alonzo, D., Balland, V., Zambrano, G., Chino, M., Nastri, F., Maglio, O., Pavone, V. & Lombardi, A. Mn-Mimochrome VI*a: An Artificial Metalloenzyme With Peroxygenase Activity. *Front. Chem.* **6,** 1–14 (2018).
16. Khan, K. K., Mondal, M. S. & Mitra, S. Kinetic studies of the reaction of hydrogen peroxide with manganese-reconstituted horseradish peroxidase. *J. Chem. Soc., Dalton Trans.* **0,** 1059–1062 (1996).
17. Primus, J.-L., Grunenwald, S., Hagedoorn, P.-L., Albrecht-Gary, A.-M., Mandon, D. & Veeger, C. The nature of the intermediates in the reactions of Fe(III)- and Mn(III)-microperoxidase-8 with H(2)O(2): a rapid kinetics study. *J. Am. Chem. Soc.* **124,** 1214–1221 (2002).
18. Hersleth, H.-P., Ryde, U., Rydberg, P., Görbitz, C. H. & Andersson, K. K. Structures of the high-valent metal-ion haem–oxygen intermediates in peroxidases, oxygenases and catalases. *J. Inorg. Biochem.* **100,** 460–476 (2006).
19. Dolphin, D., Forman, A., Borg, D. C., Fajer, J. & Felton, R. H. Compounds I of Catalase and Horse Radish Peroxidase: π-Cation Radicals. *Proc. Natl. Acad. Sci. U.S.A.* **68,** 614–618 (1971).
20. Huang, X. & Groves, J. T. Oxygen Activation and Radical Transformations in Heme-proteins and Metalloporphyrins. *Chem. Rev.* **118,** 2491–2553 (2017).
21. Khan, K. K., Mondal, M. S. & Mitra, S. Kinetics and thermodynamics of the reaction of peroxides with manganese-reconstituted horseradish peroxidase: a stopped-flow transient kinetic investigation. *J. Chem. Soc., Dalton Trans.* **0,** 533–536 (1998).
22. Nick, R. J., Ray, G. B., Fish, K. M., Spiro, T. G. & Groves, J. T. Evidence for a weak Mn:O bond and a non-porphyrin radical in manganese-substituted horseradish peroxidase compound I. *J. Am. Chem. Soc.* **113,** 1838–1840 (2002).
23. Ryabova, E. S. & Nordlander, E. Synthesis and reactivity studies of a manganese 'microperoxidase' containing b-type heme. *Dalton Trans.* **7,** 1228–1233 (2005).
24. Nastri, F., Lista, L., Ringhieri, P., Vitale, R., Faiella, M., Andreozzi, C., Travascio, P., Maglio, O., Lombardi, A. & Pavone, V. A Heme–Peptide Metalloenzyme Mimetic with Natural Peroxidase-Like Activity. *Chem. Eur. J.* **17,** 4444–4453 (2011).

25. Chino, M., Leone, L., Zambrano, G., Pirro, F., D'Alonzo, D., Firpo, V., Aref, D., Lista, L., Maglio, O., Nastri, F. & Lombardi, A. Oxidation catalysis by iron and manganese porphyrins within enzyme-like cages. *Biopolymers* **109,** e23107 (2018).
26. Primus, J.-L., Boersma, M. G., Mandon, D., Boeren, S., Veeger, C., Weiss, R. & Rietjens, I. M. C. M. The effect of iron to manganese substitution on microperoxidase 8 catalysed peroxidase and cytochrome P450 type of catalysis. *J. Biol. Inorg. Chem.* **4,** 274–283 (1999).
27. Reedy, C. J., Elvekrog, M. M. & Gibney, B. R. Development of a heme-protein structure–electrochemical function database. *Nucleic Acids Res.* **36,** D307–D313 (2008).
28. Tezcan, F. A., Winkler, J. R. & Gray, H. B. Effects of Ligation and Folding on Reduction Potentials of Heme-proteins. *J. Am. Chem. Soc.* **120,** 13383–13388 (1998).
29. Caserta, G., Chino, M., Firpo, V., Zambrano, G., Leone, L., D'Alonzo, D., Nastri, F., Maglio, O., Pavone, V. & Lombardi, A. Enhancement of peroxidase activity in the artificial Mimochrome VI catalysts through rational design. *ChemBioChem* **19,** 1823–1826 (2018).
30. Cai, Y.-B., Li, X.-H., Jing, J. & Zhang, J.-L. Effect of distal histidines on hydrogen peroxide activation by manganese reconstituted myoglobin. *Metallomics* **5,** 828–835 (2013).
31. Yeh, H.-C., Yu, C.-H., Wang, J.-S., Chen, S.-T., Su, O. Y. & Lin, W.-Y. Stopped-flow kinetic study of the peroxidase reactions of mangano-microperoxidase-8. *J. Biol. Inorg. Chem.* **7,** 113–119 (2001).
32. Goto, Y., Matsui, T., Ozaki, S., Watanabe, Y. & Fukuzumi⊥, S. Mechanisms of Sulfoxidation Catalyzed by High-Valent Intermediates of Heme Enzymes: Electron-Transfer vs Oxygen-Transfer Mechanism. *J. Am. Chem. Soc.* **121,** 9497–9502 (1999).
33. Ohashi, M., Koshiyama, T., Ueno, T., Yanase, M., Fujii, H. & Watanabe, Y. Preparation of Artificial Metalloenzymes by Insertion of Chromium(III) Schiff Base Complexes into Apomyoglobin Mutants. *Angew. Chem. Int. Ed. Engl.* **42,** 1005–1008 (2003).
34. Mahammed, A. & Gross, Z. Albumin-Conjugated Corrole Metal Complexes: Extremely Simple Yet Very Efficient Biomimetic Oxidation Systems. *J. Am. Chem. Soc.* **127,** 2883–2887 (2005).
35. Ricoux, R., Allard, M., Dubuc, R., Dupont, C., Maréchal, J.-D. & Mahy, J.-P. Selective oxidation of aromatic sulfide catalyzed by an artificial metalloenzyme: new activity of hemozymes. *Org. Biomol. Chem.* **7,** 3208–3211 (2009).
36. Sansiaume-Dagousset, E., Urvoas, A., Chelly, K., Ghattas, W., Maréchal, J.-D., Mahy, J.-P. & Ricoux, R. Neocarzinostatin-based hybrid biocatalysts for oxidation reactions. *Dalton Trans.* **43,** 8344–8354 (2014).

37. Tang, J., Huang, F., Wei, Y., Bian, H., Zhang, W. & Liang, H. Bovine serum albumin–cobalt(II) Schiff base complex hybrid: an efficient artificial metalloenzyme for enantioselective sulfoxidation using hydrogen peroxide. *Dalton Trans.* **45,** 8061–8072 (2016).
38. Garner, D. K., Liang, L., Barrios, D. A., Zhang, J.-L. & Lu, Y. Covalent Anchor Positions Play an Important Role in Tuning Catalytic Properties of a Rationally Designed MnSalen-containing Metalloenzyme. *ACS Catal.* **1,** 1083–1089 (2011).
39. Colonna, S., Gaggero, N., Carrea, G. & Pasta, P. Horseradish peroxidase catalysed sulfoxidation is enantioselective. *J. Chem. Soc., Chem. Commun.* **1992,** 357–358 (1992).
40. Gajhede, M. Plant peroxidases: substrate complexes with mechanistic implications. *Biochem. Soc. Trans.* **29,** 91–99 (2001).
41. Ozaki, S. & Ortiz de Montellano, P. R. Molecular Engineering of Horseradish Peroxidase: Thioether Sulfoxidation and Styrene Epoxidation by Phe-41 Leucine and Threonine Mutants. *J. Am. Chem. Soc.* **117,** 7056–7064 (1995).
42. Savenkova, M. I., Newmyer, S. L. & Ortiz de Montellano, P. R. Rescue of His-42 → Ala Horseradish Peroxidase by a Phe-41 → His Mutation Engineering of a Surrogate Catalytic Histidine. *J. Biol. Chem.* **271,** 24598–24603 (1996).
43. Savenkova, M. I., Kuo, J. M. & Ortiz de Montellano, P. R. Improvement of Peroxygenase Activity by Relocation of a Catalytic Histidine within the Active Site of Horseradish Peroxidase. *Biochemistry* **37,** 10828–10836 (1998).
44. Velde, F. van de, Rantwijk, F. van & Sheldon, R. A. Improving the catalytic performance of peroxidases in organic synthesis. *Trends Biotechnol.* **19,** 73–80 (2001).
45. Linhares, M., Rebelo, S. L. H., Simões, M. M. Q., Silva, A. M. S., Neves, M. G. P. M. S., Cavaleiro, J. A. S. & Freire, C. Biomimetic oxidation of indole by Mn(III)porphyrins. *Appl. Catal. A: General* **470,** 427–433 (2014).
46. Gillam, E. M., Notley, L. M., Cai, H., De Voss, J. J. & Guengerich, F. P. Oxidation of indole by cytochrome P450 enzymes. *Biochemistry* **39,** 13817–13824 (2000).
47. Kuo, H. H. & Mauk, A. G. Indole peroxygenase activity of indoleamine 2,3-dioxygenase. *Proc. Natl. Acad. Sci. U.S.A.* **109,** 13966–13971 (2012).
48. Barrios, D. A., D'Antonio, J., McCombs, N. L., Zhao, J., Franzen, S., Schmidt, A. C., Sombers, L. A. & Ghiladi, R. A. Peroxygenase and Oxidase Activities of Dehaloperoxidase-Hemoglobin from Amphitrite ornata. *J. Am. Chem. Soc.* **136,** 7914–7925 (2014).
49. Liu, C., Xu, J., Gao, S.-Q., He, B., Wei, C.-W., Wang, X.-J., Wang, Z. & Lin, Y.-W. Green and efficient biosynthesis of indigo from indole by engineered myoglobins. *RSC Advances* **8,** 33325–33330 (2018).

50. Rebelo, S. L. H., Linhares, M., Simões, M. M. Q., Silva, A. M. S., Neves, M. G. P. M. S., Cavaleiro, J. A. S. & Freire, C. Indigo dye production by enzymatic mimicking based on an iron(III)porphyrin. *J. Catal.* **315,** 33–40 (2014).
51. Corbett, M. D. & Chipko, B. R. Peroxide oxidation of indole to oxindole by chloroperoxidase catalysis. *Biochem. J.* **183,** 269–276 (1979).
52. Xiao, M., Wu, W., Wei, L., Jin, X., Yao, X. & Xie, Z. Total synthesis of (−)-isatisine A via a biomimetic benzilic acid rearrangement. *Tetrahedron* **71,** 3705–3714 (2015).
53. Devi, L., Shukla, R. & Rastogi, N. Intramolecular trapping of ammonium ylides with N -benzoylbenzotriazoles in aqueous medium: direct access to the pseudoindoxyl scaffold. *Org. Biomol. Chem.* **17,** 135–139 (2019).
54. Atienza, B. J. P., Jensen, L. D., Noton, S. L., Ansalem, A. K. V., Hobman, T., Fearns, R., Marchant, D. J. & West, F. G. Dual Catalytic Synthesis of Antiviral Compounds Based on Metallocarbene–Azide Cascade Chemistry. *J. Org. Chem.* **83,** 6829–6842 (2018).
55. Liu, R.-R., Ye, S.-C., Lu, C.-J., Zhuang, G.-L., Gao, J.-R. & Jia, Y.-X. Dual Catalysis for the Redox Annulation of Nitroalkynes with Indoles: Enantioselective Construction of Indolin-3-ones Bearing Quaternary Stereocenters. *Angew. Chem. Int. Ed. Engl.* **127,** 11357–11360 (2015).
56. Desesso, J. M., Scialli, A. R. & Goeringer, G. C. D-mannitol, a specific hydroxyl free radical scavenger, reduces the developmental toxicity of hydroxyurea in rabbits. *Teratology* **49,** 248–259 (1994).
57. Arasasingham, R. D., He, G. X. & Bruice, T. C. Mechanism of manganese porphyrin-catalyzed oxidation of alkenes. Role of manganese(IV)-oxo species. *J. Am. Chem. Soc.* **115,** 7985–7991 (1993).
58. Gillam, E. M., Notley, L. M., Cai, H., De Voss, J. J. & Guengerich, F. P. Oxidation of indole by cytochrome P450 enzymes. *Biochemistry* **39,** 13817–13824 (2000).
59. Xu, J., Shoji, O., Fujishiro, T., Ohki, T., Ueno, T. & Watanabe, Y. Construction of biocatalysts using the myoglobin scaffold for the synthesis of indigo from indole. *Catal. Sci. Technol.* **2,** 739–744 (2012).
60. Liu, C., Xu, J., Gao, S.-Q., He, B., Wei, C.-W., Wang, X.-J., Wang, Z. & Lin, Y.-W. Green and efficient biosynthesis of indigo from indole by engineered myoglobins. *RSC Advances* **8,** 33325–33330 (2018).
61. Lewis, R. D., Garcia-Borràs, M., Chalkley, M. J., Buller, A. R., Houk, K. N., Kan, S. B. J. & Arnold, F. H. Catalytic iron-carbene intermediate revealed in a cytochrome c carbene transferase. *Proc. Natl. Acad. Sci. U.S.A.* **115,** 7308–7313 (2018).
62. Zhang, R. K., Chen, K., Huang, X., Wohlschlager, L., Renata, H. & Arnold, F. H. Enzymatic assembly of carbon–carbon bonds via iron-catalysed sp 3 C–H functionalization. *Nature* **565,** 67–72 (2019).

63. Edwards, E. H. & Bren, K. L. Carbene capture in a myoglobin mutant. *Nat. Catal.* **1,** 565–566 (2018).
64. Coelho, P. S., Brustad, E. M., Kannan, A. & Arnold, F. H. Olefin cyclopropanation via carbene transfer catalyzed by engineered cytochrome P450 enzymes. *Science* **339,** 307–310 (2013).
65. Coelho, P. S., Wang, Z. J., Ener, M. E., Baril, S. A., Kannan, A., Arnold, F. H. & Brustad, E. M. A serine-substituted P450 catalyzes highly efficient carbene transfer to olefins in vivo. *Nat. Chem. Biol.* **9,** 485–487 (2013).
66. Bordeaux, M., Tyagi, V. & Fasan, R. Highly Diastereoselective and Enantioselective Olefin Cyclopropanation Using Engineered Myoglobin-Based Catalysts. *Angew. Chem. Int. Ed. Engl.* **127,** 1764–1768 (2015).
67. Vargas, D. A., Tinoco, A., Tyagi, V. & Fasan, R. Myoglobin-Catalyzed C−H Functionalization of Unprotected Indoles. *Angew. Chem. Int. Ed. Engl.* **57,** 9911–9915 (2018).
68. Tyagi, V., Bonn, R. B. & Fasan, R. Intermolecular carbene S-H insertion catalysed by engineered myoglobin-based catalysts. *Chem. Sci.* **6,** 2488–2494 (2015).
69. Wang, Z. J., Peck, N. E., Renata, H. & Arnold, F. H. Cytochrome P450-Catalyzed Insertion of Carbenoids into N-H Bonds. *Chem. Sci.* **5,** 598–601 (2014).
70. Sreenilayam, G. & Fasan, R. Myoglobin-catalyzed intermolecular carbene N–H insertion with arylamine substrates. *Chem. Commun.* **51,** 1532–1534 (2015).
71. Kan, S. B. J., Huang, X., Gumulya, Y., Chen, K. & Arnold, F. H. Genetically programmed chiral organoborane synthesis. *Nature* **552,** 132–136 (2017).
72. Kan, S. B. J., Lewis, R. D., Chen, K. & Arnold, F. H. Directed evolution of cytochrome c for carbon–silicon bond formation: Bringing silicon to life. *Science* **354,** 1048–1051 (2016).
73. Brandenberg, O. F., Fasan, R. & Arnold, F. H. Exploiting and engineering hemoproteins for abiological carbene and nitrene transfer reactions. *Curr. Opin. Biotechnol.* **47,** 102–111 (2017).
74. Zhang, R. K., Huang, X. & Arnold, F. H. Selective CH bond functionalization with engineered heme-proteins: new tools to generate complexity. *Curr. Opin. Chem. Biol.* **49,** 67–75 (2019).
75. Chen, K. & Arnold, F. H. Engineering new catalytic activities in enzymes. *Nat. Catal.* 1–11 (2020). doi:10.1038/s41929-019-0385-5
76. Key, H. M., Dydio, P., Clark, D. S. & Hartwig, J. F. Abiological catalysis by artificial haem proteins containing noble metals in place of iron. *Nature* **534,** 534–537 (2016).
77. Sreenilayam, G., Moore, E. J., Steck, V. & Fasan, R. Metal Substitution Modulates the Reactivity and Extends the Reaction Scope of Myoglobin Carbene Transfer Catalysts. *Adv. Synth. Catal.* **359,** 2076–2089 (2017).

78. Arnold, F. H. Directed Evolution: Bringing New Chemistry to Life. *Angew. Chem. Int. Ed.* **57,** 4143–4148 (2018).
79. Zeymer, C. & Hilvert, D. Directed Evolution of Protein Catalysts. *Annu. Rev. Biochem.* **87,** 131–157 (2018).
80. Renata, H., Wang, Z. J. & Arnold, F. H. Expanding the enzyme universe: accessing non-natural reactions by mechanism-guided directed evolution. *Angew. Chem. Int. Ed. Engl.* **54,** 3351–3367 (2015).
81. Stenner, R., Steventon, J. W., Seddon, A. & Anderson, J. L. R. A de novo peroxidase is also a promiscuous yet stereoselective carbene transferase. *Proc. Natl. Acad. Sci. U.S.A.* **117,** 1419–1428 (2020).
82. Renata, H., Lewis, R. D., Sweredoski, M. J., Moradian, A., Hess, S., Wang, Z. J. & Arnold, F. H. Identification of Mechanism-Based Inactivation in P450-Catalyzed Cyclopropanation Facilitates Engineering of Improved Enzymes. *J. Am. Chem. Soc.* **138,** 12527–12533 (2016).
83. Xing, W., Yin, M., Lv, Q., Hu, Y., Liu, C. & Zhang, J. 1 - Oxygen Solubility, Diffusion Coefficient, and Solution Viscosity. in *Rotating Electrode Methods and Oxygen Reduction Electrocatalysts* (eds. Xing, W., Yin, G. & Zhang, J.) 1–31 (Elsevier, 2014).
84. Watkins, D. W., Jenkins, J. M. X., Grayson, K. J., Wood, N., Steventon, J. W., Vay, K. K. L., Goodwin, M. I., Mullen, A. S., Bailey, H. J., Crump, M. P., MacMillan, F., Mulholland, A. J., Cameron, G., Sessions, R. B., Mann, S. & Anderson, J. L. R. Construction and in vivo assembly of a catalytically proficient and hyperthermostable de novo enzyme. *Nat. Commun.* **8,** 1–9 (2017).
85. Tolando, R., Ferrara, R., Eldirdiri, N. I., Albores, A., King, L. J. & Manno, M. Reductive activation of 1,1-dichloro-1-fluoroethane (HCFC-141b) by phenobarbital- and pyridine-induced rat liver microsomal cytochrome P450. *Xenobiotica* **26,** 425–435 (1996).
86. Kamel, A. & Harriman, S. Inhibition of cytochrome P450 enzymes and biochemical aspects of mechanism-based inactivation (MBI). *Drug Discov. Today* **10,** e177–e189 (2013).
87. Li, X.-X., Zheng, Q.-C., Wang, Y. & Zhang, H.-X. Theoretical insights into the reductive metabolism of CCl4 by cytochrome P450 enzymes and the CCl4 -dependent suicidal inactivation of P450. *Dalton Trans.* **43,** 14833–14840 (2014).
88. Nastri, F., Lista, L., Ringhieri, P., Vitale, R., Faiella, M., Andreozzi, C., Travascio, P., Maglio, O., Lombardi, A. & Pavone, V. A Heme–Peptide Metalloenzyme Mimetic with Natural Peroxidase-Like Activity. *Chem. Eur. J.* **17,** 4444–4453 (2011).
89. Vitale, R., Lista, L., Cerrone, C., Caserta, G., Chino, M., Maglio, O., Nastri, F., Pavone, V. & Lombardi, A. An artificial heme-enzyme with enhanced

catalytic activity: evolution, functional screening and structural characterization. *Org. Biomol. Chem.* **13,** 4859–4868 (2015).
90. Ranieri, A., Monari, S., Sola, M., Borsari, M., Battistuzzi, G., Ringhieri, P., Nastri, F., Pavone, V. & Lombardi, A. Redox and electrocatalytic properties of mimochrome VI, a synthetic heme peptide adsorbed on gold. *Langmuir* **26,** 17831–17835 (2010).
91. Zambrano, G., Ruggiero, E., Malafronte, A., Chino, M., Maglio, O., Pavone, V., Nastri, F. & Lombardi, A. Artificial Heme Enzymes for the Construction of Gold-Based Biomaterials. *Int J. Mol. Sci.* **19,** 2896 (2018).

This page was intentionally left blank.

SECTION 3:
Materials and methods

This page was intentionally left blank.

1. SYNTHESIS AND PURIFICATION OF MN-MC6*A

Apo-MC6*a was synthesized combining methods of solution and solid-phase peptide synthesis, as previously described.[1]

Manganese ion was inserted, following a slightly modified acetate method.[2] Mn^{II} acetate (10 eq.) was added to a solution of pure *apo*-MC6a in 2/3 TFE/AcOH (*v/v*) ([MC6*a] = $2.0 \cdot 10^{-4}$ M), and the reaction mixture was kept at 50°C for 4 h. The reaction was monitored by analytical RP-HPLC, using a C18 column (2.1 mm·100 mm; 1.7 μm), eluted with a linear gradient of acetonitrile in aqueous 0.1% TFA (*v/v*), from 10 to 50% over 20 min, at 0.3 mL/min flow rate.

Once the reaction was completed, the solvent was removed under vacuum and the excess of manganese acetate was removed by Reverse Phase-Flash Chromatography, using a SNAP KP-C18-HS 30 g column, eluted a gradient of acetonitrile in 0.1% aqueous TFA, 5% to 95% over 2 column volumes, at 25 mL/min flow rate. The product was then purified by preparative RP-HPLC using a C18 column (250 mm · 22 mm, 10 μm) eluted with a linear gradient of acetonitrile in aqueous 0.1% TFA (*v/v*), from 10 to 50% over 30 min, at 23 $mL \cdot min^{-1}$ flow rate.

Product purity was assessed by analytical HPLC (Figure 1.1A). The fractions containing the pure product were re-united, lyophilized and then stored at T = -20°C. Electrospray Ionization (ESI) Mass spectrometry (MS) analysis provided confirmation of the product identity, since the experimental mass was in agreement with the theoretical value (Figure 1.1B).

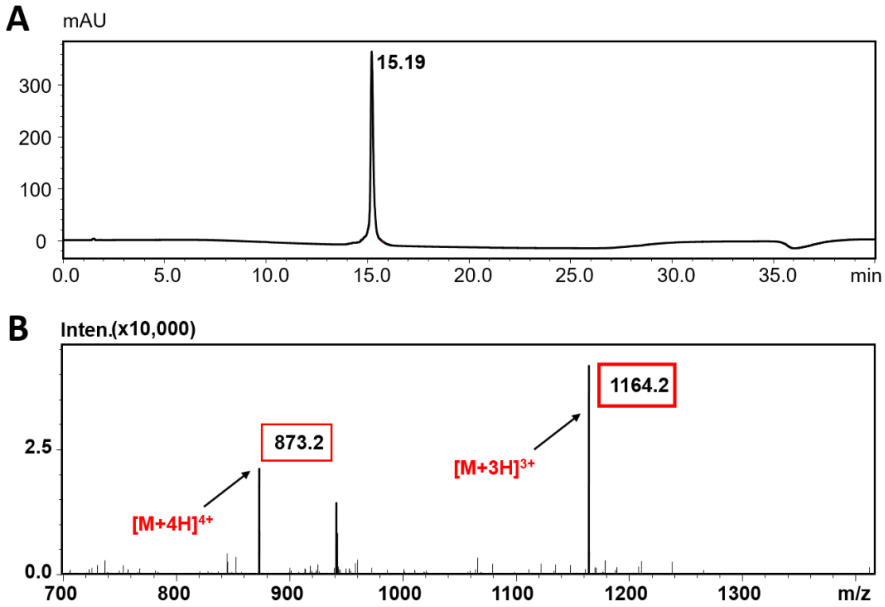

Figure 1.1: HPLC chromatogram of pure Mn^{III}-MC6a, and its positive ESI-MS spectrum (B). The peaks corresponding to the intact compound, carrying the indicated number of charges (protons), are evidenced. Experimental mass: (3489.2 ± 0.4) Da; Theoretical mass: 3488.8 Da.

2. SPECTROSCOPIC CHARACTERIZATION

2.1. Determination of molar extinction coefficient of Mn-MC6*a

Molar absorptivity (ε) at 365 nm was determined for Mn-MC6*a using Atomic Absorption spectroscopy (AAS) and UV-vis spectroscopy. In detail, a stock solution of the catalyst (≈ $2.0 \cdot 10^{-4}$ M) was prepared in H_2O 0.1% TFA (*v/v*) and its concentration was determined after mineralization using AAS. Mineralization was carried out by treating aliquots (50 µL) of stock solution with HNO_3 (200 µL) at 95°C for 2 h. Then, the samples were diluted with H_2O 2% HNO_3 (*v/v*) to a final concentration of Mn^{III} ions of ≈ 2 ppb. Manganese concentration in the stock solution was determined by comparison with a calibration curve obtained using standards. Since metal:catalyst ratio is 1:1, the catalyst concentration was determined. Another aliquot of the same Mn-MC6*a stock solution examined by AAS was used to prepare different diluted samples, which were then used to obtain the ε value at 365 nm by UV-Vis spectroscopy. The absorbance at 365 nm was plotted as a function of catalyst concentration (Figure 2.1). The experimental data were fitted to a Lambert-Beer's law, giving a ε_{365} = (7.84 ± 0.02) · 10^4 M^{-1} cm^{-1}.

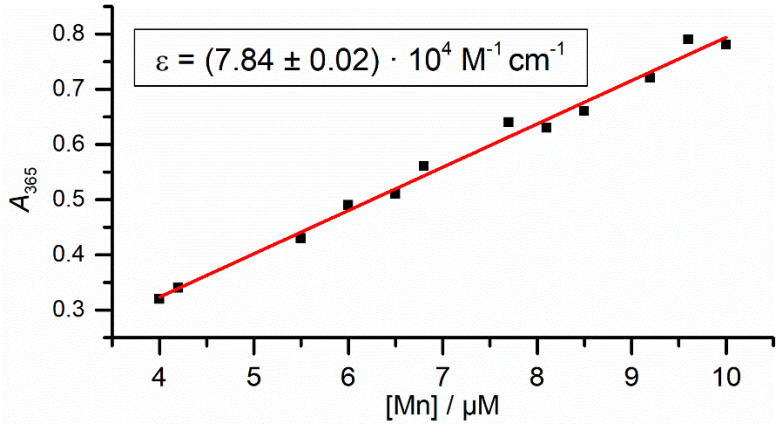

Figure 2.1. Plot of the absorbance at 365 nm as a function of Mn^{III}-MC6*a concentration, indicated as Mn content assayed by AAS. Data were fitted to the Lambert-Beer's law.

2.2. CD experiments

Solutions of Mn-MC6*a (20 µM) were prepared in 5 mM phosphate buffer at pH 6.5, using various TFE percentages from 0 to 50% (*v/v*). Far-UV CD spectra were collected from 260 to 190 nm using cells of 0.1 cm path length; spectra in the Soret region were collected from 500 to 300 nm using cells of 1 cm path length. All spectra were recorded at 0.2 nm intervals with a 20 nm min^{-1} scan speed, at 2 nm bandwidth and at 16 s response. All measurements were performed at 25 °C.

2.3. UV-Vis pH titration experiments

Solutions of Mn-MC6*a (15 µM) were prepared in a mixture of H_2O and TFE (6/4 *v/v*). Solutions of NaOH (1, 0.1 and 0.01 M) and TFA (0.1 and 1% *v/v* in water) were used to adjust the pH of the samples (dilution was less than 1% and considered in the final data). Experimental data were fitted to a model describing four species involved in acid-base equilibria.

The pH-dependent equilibria are described by the following equation:

$$AH_3^{3+} \overset{Ka1}{\longrightarrow} BH_2^{2+} + H^+ \overset{Ka2}{\longrightarrow} CH^+ + H^+ \overset{Ka3}{\longrightarrow} D + H^+ \quad (2.1)$$

The equilibrium constants, Ka_1, Ka_2 and Ka_3, can be expressed as:

$$K_{a1} = \frac{[BH_2^{2+}] \cdot [H^+]}{[AH_3^{3+}]} \; ; \; K_{a2} = \frac{[CH^+] \cdot [H^+]}{[BH_2^{2+}]} \; ; \; K_{a3} = \frac{[D] \cdot [H^+]}{[CH^+]} \quad (2.2)$$

The total concentration (C_{tot}) of Mn^{III}-MC6a can be expressed as sum of the four species:

$$C_{tot} = [AH_3^{3+}] + [BH_2^{2+}] + [CH^+] + [D] \quad (2.3)$$

The total absorbance (A_{tot}) can be expressed as the sum of the contribution of all the four species:

$$A_{tot} = \varepsilon_A[AH_3^{3+}] + \varepsilon_B[BH_2^{2+}] + \varepsilon_C[CH^+] + \varepsilon_D[D] \quad (2.4)$$

The total concentration and the total absorbance can be indicated in dependence of [D]:

$$C_{tot} = [D] + \frac{[D]\cdot[H^+]}{K_{a3}} + \frac{[D]\cdot[H^+]^2}{K_{a3}\cdot K_{a2}} + \frac{[D]\cdot[H^+]^3}{K_{a3}\cdot K_{a2}\cdot K_{a1}} \quad (2.5)$$

$$A_{tot} = \varepsilon_D\cdot[D] + \varepsilon_C\cdot\frac{[D]\cdot[H^+]}{K_{a3}} + \varepsilon_B\cdot\frac{[D]\cdot[H^+]^2}{K_{a3}\cdot K_{a2}} + \varepsilon_A\cdot\frac{[D]\cdot[H^+]^3}{K_{a3}\cdot K_{a2}\cdot K_{a1}} \quad (2.6)$$

Equations 5 and 6 can be rearranged, giving:

$$A_{tot} = \frac{C_{tot}\cdot\left(\varepsilon_D + \varepsilon_C\cdot\frac{[H^+]}{K_{a3}} + \varepsilon_B\cdot\frac{[H^+]^2}{K_{a3}\cdot K_{a2}} + \varepsilon_A\cdot\frac{[H^+]^3}{K_{a3}\cdot K_{a2}\cdot K_{a1}}\right)}{\left(1 + \frac{[H^+]}{K_{a3}} + \frac{[H^+]^2}{K_{a3}\cdot K_{a2}} + \frac{[H^+]^3}{K_{a3}\cdot K_{a2}\cdot K_{a1}}\right)} \quad (2.7)$$

Equation 2.7 can be written as:

$$A_{tot} = \frac{\left(A_D + A_C\cdot\frac{[H^+]}{K_{a3}} + A_B\cdot\frac{[H^+]^2}{K_{a3}\cdot K_{a2}} + A_A\cdot\frac{[H^+]^3}{K_{a3}\cdot K_{a2}\cdot K_{a1}}\right)}{\left(1 + \frac{[H^+]}{K_{a3}} + \frac{[H^+]^2}{K_{a3}\cdot K_{a2}} + \frac{[H^+]^3}{K_{a3}\cdot K_{a2}\cdot K_{a1}}\right)} \quad (2.8)$$

A_A, A_B, A_C, A_D, parameters represent the absorbance of the four differently protonated species. Species A - D are referred as **1** - **4** in Chapter 2 of Section 2, Results and discussion. Equation 2.8 was used to fit the experimental A_{365} (Soret absorbance) data points (Figure 2.3A of Section 2, Results and discussion), which were then reported as molar extinction coefficient at 365 nm (ε_{365}).

2.4. Spectro-electrochemistry experiments

Catalysts ([Fe-MC6*a] = 100 µM or [Mn-MC6*a] = 30 µM) were prepared in buffered solutions containing 10% glycerol. Different buffers were used to obtain the different pH conditions: 100 mM sodium citrate buffer for pH 5.0; 100 mM sodium phosphate buffer for pH 6.5 and 12.0; 100 mM sodium carbonate buffer for pH 10.0; 100 mM CHES buffer with 100 mM NaCl for pH 8.5. 20 µM

anthroquinone-2-sulfonate (-225 mV), 20 μM phenazine (-180 mV), 25 μM 2-hydroxy-1,4-napthoquinone (-152 mV), 6 μM indigotrisulfonate (-90 mV) and 50 μM duroquinone (5 mV) were used as redox mediators in all the experiments. Benzyl viologen (-374 mV) was added as redox mediator only in the experiments with Mn-MC6*a, since more negative potential values were explored.

Catalyst solutions (120 μL) were added to a thin layer cell (0.3 mm) set up for UV−Vis and electrochemical measurements. A Pt gauze working electrode (WE) was inserted into the thin layer cell. Following, a larger volume (4 mL) of the buffer solution, containing no glycerol or catalyst, was carefully added to the upper part of the cell. Mixing was prevented by the difference in viscosity of the two layers. Ionic conduction occurs across the liquid interface, allowing reference (KCl saturated Ag/AgCl) and counter (Pt) electrodes to be placed in the upper solution.

The applied potential was varied with discrete steps of 20 to 50 mV using a potentiostat connected to the three (working, reference and counter) electrodes. UV-Vis spectra were collected at each potential value at the end of 30 minutes equilibration time. In each experiment, the potential was stepped from positive to negative values (reduction scan) and back to the initial potential value (oxidation scan). All potentials in the text are reported *vs* normal hydrogen electrode (NHE), based on a value of E(Ag/AgCl) = 0.225 versus NHE at room temperature.

2.5. Reaction of Mn^{III}-MC6*a with H_2O_2

Solutions of Mn-MC6*a (20 μM) were prepared in 60 mM carbonate buffer containing 40% TFE (*v/v*) at pH 10. Reactions were initialized by addition of different amount of hydrogen peroxide (1, 10, 100 eq.) from properly diluted stock solutions of H_2O_2 in water. Reaction progress was followed by continuously collecting UV-Vis spectra in the 250-750 nm region using a 9600 nm/min scan speed. Catalyst recovery was estimated based on the Soret absorbance when no more changes were observed. Similar experiments were performed with a

prepared sample of Mn-HRP. In these cases, 8.0 μM protein in 100 mM phosphate buffered solutions at pH 7 were employed.

In the pH-dependent experiments, reactions were initiated by addition of 1.0 eq. H_2O_2 to a buffered solution of the catalyst (20 μM) containing 40% TFE (*v/v*). Different buffers were used depending on the pH: pH 6.5-8.5, phosphate buffer; pH 9.5-10 carbonate buffer. The pH of the solutions was adjusted with NaOH in the experiments at higher pH values. Reactions were monitored over 60 s by collecting the single-wavelength absorbance traces at 393 nm. The initial rate (v_0) was determined, for each pH value, as the slope of the reaction progress curve at t = 0.

All experiments were performed at T = 25 °C, under magnetic stirring, using quartz cells of 1 cm path length.

2.6. Preparation of Mn-HRP

Mn-protoporphyrin IX, *apo*-HRP and Mn-HRP were prepared according to literature procedures. [4] The insertion of Mn porphyrin into *apo*-peroxidase was assessed by UV-Vis spectroscopy in comparison with literature data.[4,5] The homogeneity of the sample was ascertained by analytical Gel Filtration Chromatography (Figure 2.2), using a Yarra SEC-2000 column (7.8 mm·300 mm; 3 μm), with an isocratic flow of 0.05 M sodium phosphate 0.3 M NaCl pH 6.8 as mobile phase, at a flow rate of 0.35 mL/min.

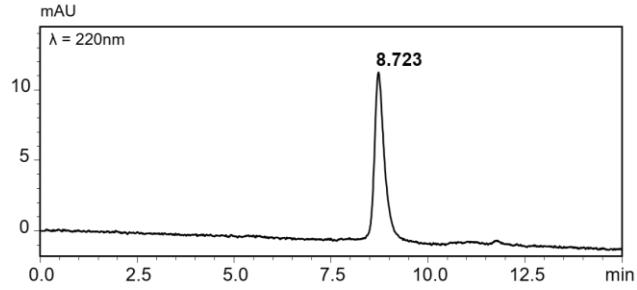

Figure 2.2. GFC chromatogram of: Mn^{III}-HRP (C = 0.1 mg/ml, 0.05 M sodium phosphate, 0.3 M NaCl, pH 6.8).

Fe-HRP was analysed under the same experimental conditions for comparison (data not shown).

Molecular weight of the samples was determined based on a calibration curve obtained with standards (Figure 2.3). The GE Healthcare LMW Calibration kit, containing Conalbumin, Ovalbumin, Carbonic anhydrase and Ribonuclease A, all at a concentration of 1 mg/ml, was used for calibration. To prepare the calibration curve, K_{av} of the proteins were calculated as follows (Equation 2.9):

$$K_{av} = \frac{V_e - V_0}{V_c - V_0} \qquad (2.9)$$

where V_0 is column void volume, V_c is the geometric volume of column, V_e is the elution volume of the protein.

A value of 48 kDa was found for the molecular weight of both Fe-HRP and Mn-HRP.

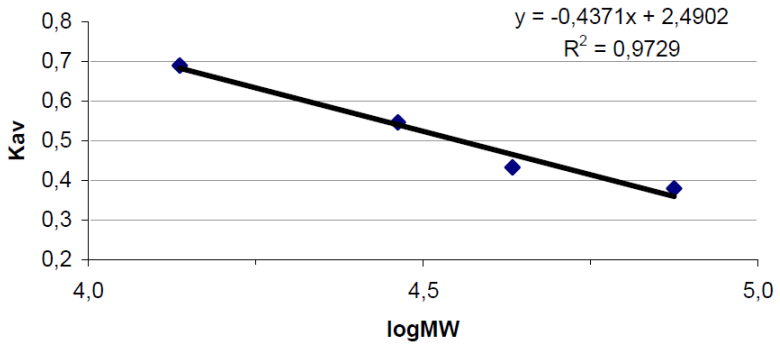

Figure 2.3: GFC calibration curve prepared using Conalbumin (MW: 75 kDa), Ovalbumin (MW: 43 kDa), Carbonic Anhydrase (MW: 29 kDa), Ribonuclease A (MW: 13.7 kDa).

3. SULFOXIDATION OF PHENYL-THIOETHERS

Stock solutions of substrates (thioanisole, TA; *p*-chlorothioanisole, *p*CTA; *p*-nitrothioanisole, *p*NTA; *p*-methoxythioanisole, *p*MTA; cyclopropyl-phenyl sulfide, CPPS) were prepared dissolving a known amount of neat sulfide in TFE to a final concentration of 0.1 M.

All reactions were carried out at 20 μM catalyst concentration in 60 mM buffered solution with 40% TFE (*v/v*). Reactions with Mn-HRP and Fe-MC6*a as catalysts were performed in absence and in presence of 50% (*v/v*) TFE, respectively. Depending on the pH value, different buffers were used: pH 6.5-8.5, phosphate buffer; pH 9.5-10.0, 11.0. All reactions were carried out at room temperature and under magnetic stirring. All assays were performed at 1:100:100 catalyst:substrate:oxidant ratio. TON was determined using a 1:1000:1000 ratio and a 1:2000:2000 ratio for Mn- and Fe-MC6*a, respectively.

The catalyst was preloaded with substrate prior to addition of hydrogen peroxide. Reaction was then initialized by addition of hydrogen peroxide from a solution of 0.1 M H_2O_2 in water. For TA, reaction was carried out also using ^{18}O labeled hydrogen peroxide to test the peroxygenase activity of Fe- and Mn-MC6*a. A solution of 90% ^{18}O enriched H_2O_2, at 0.1 M concentration was used. Reaction progress was monitored by GC-MS, using anisole as internal standard. At different times, an aliquot of the reaction mixture (50 μl) was diluted with an equal volume of H_2O 0.1% TFA (*v/v*) and extracted with ethyl acetate (100 μL). Residual water was removed from the organic phase with anhydrous sodium sulfate. GC-MS analysis of the organic phase was performed using a Rxi-5Sil-MS Column with helium as carrier gas. A linear gradient from 80°C to 230°C with a rate of 18°C min^{-1} was used for thioanisole and *p*CTA; a linear gradient from 70° to 200°C with a rate of 15°C min^{-1} was used for CPPS; a linear gradient from 70° to 200°C with a rate of 18°C min^{-1}, and then from 200°C to 300°C with a rate of

40°C min^{-1} was used for *p*NTA and *p*MTA. MS analysis was performed in TIC (Total Ion Current) mode, exploring a range of m/z from 50 to 250 Th. The degree of conversion at different reaction times was determined based on substrate consumption, using the following equation (Equation 2.10):

$$Conversion\ (\%) = \frac{\left(\frac{A_{sub}}{A_{I.Std}}\right)_0 - \left(\frac{A_{sub}}{A_{I.Std.}}\right)_x}{\left(\frac{A_{sub}}{A_{I.Std.}}\right)_0} \cdot 100 \qquad (2.10)$$

where A_{sub} and $A_{I.Std.}$ are the peak areas of substrate and internal standard, respectively, in the GC-MS TIC chromatogram. The subscript *0* indicates the trace acquired prior to addition of peroxide, while the subscript *x* is a specific time during the reaction course. Control reactions in the absence of catalyst were also performed and gave no reaction progress.

4. INDOLE OXIDATION

4.1. Oxidation of indoles: general procedure

Stock solutions of indoles were freshly prepared by dissolving a weighted amount of the pure compound in TFE. All solutions were stored at -20°C until their use.

H_2O_2 (1 mM) was added to a stirring mixture of the catalyst (10 μM Mn- or Fe-MC6*a) and the substrate (1 mM) in the appropriate buffer (60 mM) containing 40% TFE (*v/v*). Phosphate buffer was used in the reactions at pH 6.5, 7.5 and 8.5, while carbonate buffer was used at pH 9.5 and pH 10.0. Aliquots of the reaction mixture (30 μL) were taken at given times (from 5 to 120 min), diluted with H_2O containing 1% formic acid (30 μL) and analysed by HPLC.
HPLC analyses were performed with a Kinetex Phenyl Hexyl column (150 x 4.6 mm, 5μm) using water 0.1% formic acid (A) and acetonitrile 0.1% formic acid (B) as the eluents. A linear gradient from 5 to 50% B over 30 min at a flow rate of 1.85 mL/min was used as the elution method in all analyses.

4.2. Identification of oxidation products

Identification of oxidation products was performed by high-resolution mass spectrometry (HRMS) analysis and comparison of the experimental UV-Vis absorption spectra with literature data and standard compounds. Pure products were collected by HPLC analysis of reaction mixture and then subjected to MS analysis using an ESI-TOF instrument. Some of the standard compounds were synthesized according to standard organic synthesis procedures reported in the literature.

4.3. Synthesis of standard compounds

4.3.1. Synthesis of isatin

Following a literature procedure,[6] indole was oxidized to isatin by the reaction

with I_2 and *t*-butyl hydroperoxide (TBHP) in dimethylsulfoxide (DMSO) at high temperatures (80-85 °C) for 24h (**Scheme 4.1**).

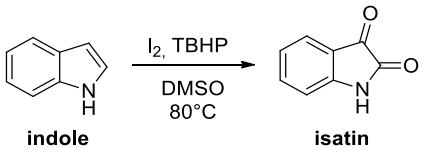

Scheme 4.1. Synthesis of isatin.

Under an air atmosphere, indole (5 mmol, 585 mg) and DMSO (10 mL) were added into a flask and vigorously stirred at 80 °C. Then I_2 (6 mmol, 1.5 g) and TBHP (25 mmol, 4 mL, 5 eq.) in DMSO (6 mL) were sequentially added to the flask dropwise. The reaction was stirred until indole consumption as monitored by GC/MS analysis. Afterwards, 5% $Na_2S_2O_3$ solution (100 mL) was added to the mixture. The latter was extracted with ethyl acetate (3×15 mL) and the organic layer was dried (Na_2SO_4) and evaporated. Then a sample of the crude residue was purified by column chromatography on silica gel. NMR data of isatin were in agreement with those reported in literature.[6] The product was then analysed in by analytical HPLC and MS in the same experimental conditions used to monitor the catalytic indole oxidation, providing identification to the isolated product (see Figures 4.2 and 4.3 of Section 2, Results and discussion).

4.3.2. Synthesis of N-methyl-indole

Synthesis of *N*-methyl indole was achieved in one step from indole, following a standard methylation procedure involving iodomethane (**Scheme 4.2**).

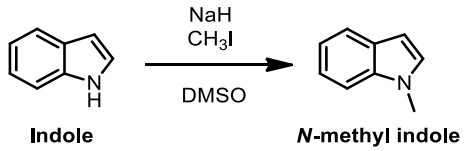

Scheme 4.2. Synthesis of *N*-methyl-indole

To a solution of indole (2 mmol, 234 mg) in anhydrous DMSO (2 mL), NaH (2.4 mmol, 96 mg, 1.2 eq., 60%, dispersed in mineral oil) was added under inert gas at room temperature. After the reaction mixture was stirred for 2 h, a solution of iodomethane (1.5 mL, 1.5 eq.) in DMSO (1 mL) was added and stirred for 2 h. Afterwards, the reaction was quenched with water and the aqueous layer was extracted with ethyl acetate. The combined organic layer was dried over Na_2SO_4 and evaporated to leave a residue, which was purified by column chromatography using hexane and dichloromethane as eluents to yield 185 mg of the pure compound (70% yield). NMR data of *N*-methyl indole were in agreement with those reported in literature.[7]

The product was then analysed in by analytical HPLC and MS in the same experimental conditions used to monitor the catalytic *N*-methyl-indole oxidation, providing identification to the isolated product (see Figures 4.11 and 4.12 of Section 2, Results and discussion).

4.3.3. Synthesis of N-methyl-2-oxindole

N-methyl-2-oxindole was obtained from standard 2-oxindole using dimethyl-sulfate instead of methyl-iodide as the methylating agent (**Scheme 4.3**).

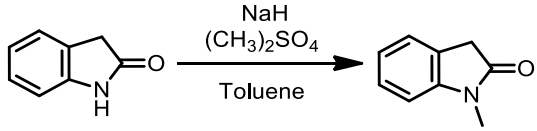

Scheme 4.3. Synthesis of N-methyl-2-oxindole

2-Oxindole (2 mmol, 265 mg) was dissolved in freshly distilled toluene (5 mL) under vigorously stirring. Sodium hydride (2.1 mmol, 0.084 g, 60% suspension in mineral oil, 1.05 eq) was added to the previous solution and the resulting mixture was stirred at 60 °C for 20 min. Dimethyl sulfate (2.4 mmol, 0.165 mL, 1.2 eq) was then added dropwise to mixture. The solution was stirred at 60 °C for 1h and

then at rt for 16h. Then the reaction was cooled to rt and the mixture was washed with brine and then extracted using AcOEt (3x20 mL). The organic layers were combined, dried over Na_2SO_4 and evaporated under vacuum. An aliquot of the crude residue was purified over silica gel, to afford the pure *N*-methyl oxindole. ^1H NMR spectrum of the synthesized product was in agreement with that reported in literature.[8]

5. METALLO-CARBENOID FORMATION STUDIES

5.1. UV-Vis stopped-flow studies

All the assays were carried out under nitrogen inside an anaerobic glovebox ([O_2] < 10 ppm). In a typical experiment, the catalyst was dissolved in 100 mM sodium phosphate buffer pH 6.5, 50% TFE *v/v* and pre-mixed with a large excess of sodium dithionite to achieve its complete reduction. The reduced catalyst was then mixed with a solution of EDA (in ethanol or in TFE/buffer 50% *v/v*) in a stopped-flow spectrophotometer and the changes in the UV-Vis spectrum were monitored over different time periods (1-1000 s). Identical conditions were employed in the screening of different carbene precursors (*t*-BuDa and BnDA). Final concentrations were 5 μM catalyst and 500 μM diazo-compound.

5.2. MS analysis

Solutions of Fe^{II}-MC6*a (100 μM, 0.4 mL) and EDA (400 mM stock in ethanol) were prepared into sealed top vials containing silicon septa inside an anaerobic glovebox. Addition of the diazo-compound (10 μL) was carried out via gas-tight syringe suddenly before loading the sample into the mass spectrometer, where an isocratic 100 mM ammonium acetate solution was employed as the mobile phase (0.25 mL min^{-1}). 20 μL injections were employed and the progression of the sample into the chamber was also monitored spectroscopically at 280 nm. Identical conditions were employed for Mn-MC6*a.

5.3. Carbene-transfer assays

In the screening for carbene-transfer activity, the catalyst (10 μM) was reduced with an excess of sodium dithionite and preloaded with the substrate (30 mM). Reaction was then initialized by anaerobic addition of the carbene precursor (10 mM) and kept anaerobically under stirring at room temperature for 2 hours. Reaction mixtures were quenched by addition of 20 μL 3M HCl and then extracted

with ethyl acetate. The organic phase was dried with $MgSO_4$ prior to be analysed by HPLC. A chiral-HPLC column (Astec CHIROBIOTIC® V, 250 x 21 mm, 5 µm) was used, employing an isocratic polar organic mobile phase (100% acetonitrile: 0.1% *v/v* TFA: 0.1% *v/v*: Et_3N; 0.1 $mL.min^{-1}$ flow rate and 5 µL injection volume.

5.4. Oxygen-binding studies

O_2-saturated buffers were obtained by continuously bubbling oxygen through the solutions for 20 minutes. Solutions at lower O_2 concentrations were obtained by mixing an O_2-saturated buffer with an N_2-purged buffer *via* gas-tight syringes. Fe^{II} and Mn^{II} catalyst was generated by anaerobic addition of a slight excess of sodium dithionite. Catalyst reduction was assessed by UV-Vis spectroscopy by means of a fiber-optics device placed inside the glovebox. The process was monitored by UV-Vis stopped flow spectroscopy. All experiments were performed at 5°C.

6. EXPERIMENTAL EQUIPMENT

6.1. Materials

HPLC grade solvents were employed for chromatographic analyses and purifications (Romil). Solvents with higher degree of purity were used in the preparation of solutions for mass spectrometry and spectroscopic investigations (Ups grade, Romil). Phosphate and carbonate salts (mono- and dibasic), for buffers preparation, Mn^{II} acetate, glacial acetic, thioanisole (analytical standard), indole, 3-methyl-indole (analytical standard), ethyl-diazoacetate (15% in toluene), *tert*-butyl diazoacetate (15% in toluene), benzyl diazoacetate (10% in toluene) hydrogen peroxide (H_2O_2) solution (30% *w/w* in water) and isotope labelled hydrogen peroxide ($H_2{}^{18}O_2$) solution (3% *w/w* in water) were supplied by Sigma Aldrich. Sodium dithionite (85% *w/w*), 4-nitrothioanisole, 4-chlorothioanisole, 4-methoxythioanisole and cyclopropyl-phenyl-sulfide employed in catalytic assays were all provided (98% purity) by Alfa Aesar. All products purchased commercially were used without further purification, unless otherwise stated.

6.2. Instruments

Analytical RP-HPLC analyses were performed with a Shimadzu LC-10ADvp equipped with an SPDM10Avp diode-array detector.

Flash Chromatography was performed using a Biotage Isolera flash purification system, equipped with a diode-array detector.

Catalyst purifications were carried out with a preparative Shimadzu LC-8A equipped with SPD-10A UV-Vis detector.

ESI-MS spectra of the catalysts were recorded on a Shimadzu LC-MS-2010EV system with ESI interface, Q-array-octapole-quadrupole mass analyser, and Shimadzu LC-MS solution workstation software for data processing. Only the metallo-carbenoid formation was examined using a Waters Xevo G2-XS with an ESI MS source and a Q-TOF array of mass analysers. HRMS spectra of indole

oxidation products were recorded on a Shimadzu LCMS-IT-TOF system with an ESI MS source and an IT-TOF array of mass analysers.

Atomic absorption measurements were performed using a Shimadzu AA-7000 Series equipped with a graphite furnace atomizer.

UV-Vis analyses were performed with a Cary Varian 60 Probe UV Spectrophotometer equipped with a thermostatic cell holder and a magnetic stirrer.

CD measurements were carried out on Jasco J-815 dichrograph, equipped with a thermostatic cell holder (JASCO, Easton, MD, USA).

GC/MS analyses were performed by a Shimadzu GCMS-QP2010 SE system equipped with an EI MS source and a quadrupole array as MS analyser.

NMR spectra were acquired at 25 °C, on a Bruker Avance 600 spectrometer equipped with a triple resonance cryo-probe.

Kinetic measurements were performed with a SX20 Stopped Flow Spectrophotometer (Applied Photophysics) housed in an anaerobic glove box under N_2 ($[O_2] < 5$ p.p.m.; Belle Technology).

7. REFERENCES

1. Caserta, G., Chino, M., Firpo, V., Zambrano, G., Leone, L., D'Alonzo, D., Nastri, F., Maglio, O., Pavone, V. & Lombardi, A. Enhancement of peroxidase activity in the artificial Mimochrome VI catalysts through rational design. *ChemBioChem* **19,** 1823–1826 (2018).
2. Buchler, J. W. 10 - Synthesis and Properties of Metalloporphyrins. in *The Porphyrins* (ed. Dolphin, D.) 389–483 (Academic Press, 1978).
3. Risbridger, T. A. G., Watkins, D. W., Armstrong, J. P. K., Perriman, A. W., Anderson, J. L. R. & Fermin, D. J. Effect of Bioconjugation on the Reduction Potential of Heme-proteins. *Biomacromolecules* **17,** 3485–3492 (2016).
4. Yonetani, T. & Asakura, T. Studies on Cytochrome c Peroxidase XV. Comparison Of Manganese Porphyrin-containing Cytochrome c Perxidase, Horseradish Peroxidase, and Myoglobin. *J. Biol. Chem.* **244,** 4580–4588 (1969).
5. Khan, K. K., Mondal, M. S. & Mitra, S. Kinetic studies of the reaction of hydrogen peroxide with manganese-reconstituted horseradish peroxidase. *J. Chem. Soc., Dalton Trans.* **0,** 1059–1062 (1996).
6. Zi, Y., Cai, Z.-J., Wang, S.-Y. & Ji, S.-J. Synthesis of Isatins by I2/TBHP Mediated Oxidation of Indoles. *Org. Lett.* **16,** 3094–3097 (2014).
7. Schiffner, J. A., Wöste, T. H. & Oestreich, M. Enantioselective Fujiwara–Moritani Indole and Pyrrole Annulations Catalyzed by Chiral Palladium(II)–NicOx Complexes. *Eur. J. Org. Chem.* **2010,** 174–182 (2010).
8. Goff, R. L., Sanselme, M., Lawson, A. M., Daïch, A. & Comesse, S. Highly Stereoselective Domino Oxa-Michael/Aza-Michael/Cyclization: Synthesis of Bicyclic Lactams and Spiroox-indole Skeleton. *Eur. J. Org. Chem.* **2015,** 7244–7248 (2015).

This page was intentionally left blank.

LIST OF ACRONYMS AND ABBREVIATIONS

A: absorbance
AAS: atomic absorption spectroscopy
ABTS: 2,2'–azino–bis(3–ethylbenzthiazoline–6–sulphonic acid)
Ac: acetyl
ACN: acetonitrile
Aib: α–amino–isobutyrric acid
Ar: aryl
Arg: arginine
Asn: asparagine
Asp: aspartic acid
AU: arbitrary units
Bn: benzyl
C*c*P: cytochrome c peroxidase
CD: circular dichroism
CE: counter electrode
CTM: *c*–type Cytochrome Maquette
CV: cyclic voltammetry
Cys: cysteine
CPO: chloroperoxidase
CPPS: cyclopropyl-phenyl sulfide
D: decapeptide
DHP: dehaloperoxidase
DIEA: diisopropylethylamine
DMF: *N,N*–dimethylformamide
DMSO: dimethylsulfoxide
DPIX: deuteroporphyrin IX
EDA: ethyl diazoacetate
e.e.: enantiomeric excess
EI: electronic Impact
E_m: redox midpoint-potential
EPR: electron paramagnetic resonance
ESI–MS: electrospray ionization mass spectrometry
Et_3N: triethylamine
Fmoc: 9–fluorenylmethoxycarbonyl
GC/MS: gas chromatography–mass spectrometry

GFC: gel filtration chromatography
Gln: glutamine
Glu: glutamic acid
GOx: glucose oxidase
HATU: *N*–[(dimethylamino)–1H–1,2,3–triazolo–[4,5–b] pyridin– 1–ylmethylene]–*N*–methylmethanaminium hexafluorophosphate *N*–oxide
HCO: heme-copper oxidase
His: histidine
HPLC: high performance liquid chromatography
HRP: horseradish peroxidase
IDO: indoleamine 2,3-dioxygenase
Ile: isoleucine
IT-TOF: ion trap – time of flight
k_{cat}/K_m: catalytic efficiency
K_d: dissociation constant
k_{decay}: kinetic constant of decomposition
K_m: Michaelis–Menten constant
k_{on}: kinetic constant of formation
Leu: leucine
Lys: lysine
Mb: myoglobin
MC: mimochrome
Mes: 1,3,5-trimethylbenzyl
Mtt: 4-methyl-trityl
MP: microperoxidase
MS: mass spectrometry
MW: molecular weight
NAD(P)H: nicotinamide adenine dinucleotide (phosphate), reduced form
NCS: neocarzinostatin
NHE: normal Hydrogen Electrode
NMR: nuclear magnetic resonance
NOR: nitric oxide reductase
PDA: photodiode array
PDB: protein data bank
Ph: phenyl
*p*CTA: *p*-chlorothioanisole
*p*MTA: *p*-methoxythioanisole

*p*NTA: *p*-nitrothioanisole
Pro: proline
pK_a: negative logarithm of the acid dissociation constant
Q-TOF: quadrupole-time of flight
RE: reference electrode
ROS: reactive oxygen species
RP–HPLC: reverse phase – high performance liquid chromatography
R_T: retention time
SEC: Spectro-electrochemistry
Ser: serine
TA: thioanisole
TDO: trypthophan 2,3-dioxygenase
TON: turnover number
t-Bu: *tert*–butyl
TBHP: *tert*-butyl-hydroperoxide
TD: tetradecapeptide
TFA: trifluoroacetic acid
TFE: 2,2,2–trifluoroethanol
TMPyP: *meso*-tetrakis(*N*-methyl-4-pyridyl)porphyrin
T*p*CPP: *meso*-tetrakis(4-carboxyphenyl)porphyrin
T*p*SPP: *meso*-tetrakis(4-sulfophenyl)porphyrin
Thr: threonine
Trp: tryptophan
TLC: thin layer chromatography
Tyr: tyrosine
UV-Vis: ultra violet – visible
WE: working electrode
WT: wild-type
XlnA: xylanase A